IOWA STATE UNIVERSITY
Digital Repository

Graduate Theses and Dissertations

Iowa State University Capstones, Theses and Dissertations

2017

Enhanced Light Out-Coupling of Organic Light Emitting Devices (OLEDs) using Novel Plastic Substrates and Improved Performance of OLED-based Photoluminescence Sensing Platform

Eeshita Manna
Iowa State University

Follow this and additional works at: https://lib.dr.iastate.edu/etd

 Part of the Electrical and Electronics Commons

Recommended Citation
Manna, Eeshita, "Enhanced Light Out-Coupling of Organic Light Emitting Devices (OLEDs) using Novel Plastic Substrates and Improved Performance of OLED-based Photoluminescence Sensing Platform" (2017). *Graduate Theses and Dissertations*. 15360.
https://lib.dr.iastate.edu/etd/15360

This Dissertation is brought to you for free and open access by the Iowa State University Capstones, Theses and Dissertations at Iowa State University Digital Repository. It has been accepted for inclusion in Graduate Theses and Dissertations by an authorized administrator of Iowa State University Digital Repository. For more information, please contact digirep@iastate.edu.

www.manaraa.com

Enhanced light out-coupling of organic light emitting devices (OLEDs) using novel plastic substrates and improved performance of OLED-based photoluminescence sensing platform

by

Eeshita Manna

A dissertation submitted to the graduate faculty

in partial fulfillment of the requirements for the degree of

DOCTOR OF PHILOSOPHY

Major: Electrical Engineering

Program of Study Committee:
Joseph Shinar, Co-Major Professor
Ruth Shinar, Co-Major Professor
Rana Biswas
Mani Mina
Kai-Ming Ho

The student author and the program of study committee are solely responsible for the content of this dissertation. The Graduate College will ensure this dissertation is globally accessible and will not permit alterations after a degree is conferred.

Iowa State University

Ames, Iowa

2017

Copyright © Eeshita Manna, 2017. All rights reserved.

www.manaraa.com

TABLE OF CONTENTS

ACKNOWLEDGEMENT iv

ABSTRACT vi

CHAPTER 1. INTRODUCTION TO OLEDS 1

1.1. Brief history of OLED technology 1

1.2. OLED structure 2

1.3. Operating principles 5

1.4. Light extraction and efficiency 16

1.5. Fabrication techniques 18

1.6. Dissertation organization 20

1.7.References 22

CHAPTER 2. ENHANCED LIGHT EXTRACTION EFFICIENCY OF OLEDS WITH CONFORMALLY COATED PEDOT:PSS ON NANO-PATTERNED POLYCARBONATE SUBSTRATES 25

2.1. Introduction 26

2.2. Results and discussion 29

2.3. Challenges with corrugated OLEDs 35

2.4. Summary 42

2.5. Experimental procedure 43

2.6. References 44

CHAPTER 3. HIGH EFFICIENCY FLUORESCENT WHITE OLED ON PATTERNED PLASTIC SUBSTRATES 47

3.1. Introduction 47

3.2. Results and discussion 49

3.3. Summary 60

3.4. Experimental procedure 60

3.5. References 61

www.manaraa.com

CHAPTER 4. ORGANIC PHOTODETECTORS IN ANALYTICAL APPLICATIONS 63

4.1. Introduction 63

4.2. Organic photodetectors: working principle 66

4.3. OPDs in analytical sensing 70

4.4. Examples of potential challenges in sensing with OPDs 91

4.5. Concluding remarks and outlook 97

4.6. Acknowledgement 98

4.7. References 98

CHAPTER 5. TUNABLE NEAR UV MICROCAVITY OLEDS AND MULTICOLOR OLED ARRAYS: CHARACTERIZATION AND ANALYTICAL APPLICATIONS 105

5.1. Introduction 106

5.2. Results and discussion 109

5.3. Summary 118

5.4. Experimental procedure 119

5.5. Acknowledgement 121

5.6. References 122

CHAPTER 6. SUMMARY AND CONCLUSIONS 125

APPENDIX A: WOLEDS IN SSL AND COLOR POINT MANAGEMENT 127

APPENDIX B: OPDS IN SENSING: SUMMARY TABLES 129

www.manaraa.com

ACKNOWLEDGEMENT

I would like to express my deepest gratitude to my major professors Dr. Joseph Shinar and Dr. Ruth Shinar for their guidance and support during the entire course of this dissertation. They have been great mentors to me – advising me at every step of the way. This dissertation would not have been possible without the constant support and opportunities provided by them. I feel very fortunate to have them as my advisers and I will always hold them in the highest of regards.

I would also like to express my thanks to Dr. Rana Biswas for his collaboration with us and for helping me understand the simulation work. I am grateful to Dr. Mani Mina, Dr. Kai-Ming Ho and Dr. Malika Jeffries-EL for being on my program of study committee. I would also like to extend my great appreciation to Dr. Dennis Slafer, Diane Martin and Tom Trovato for their collaboration with us and continuous encouragement and support in pursuing my research.

I express my deepest gratitude to my parents, Amar Kumar Manna and Basabi Manna, for their unconditional love and endless support throughout my life. I dedicate my thesis and my degree to them. My heartfelt thanks go to my brother and to my entire family for believing in me and for making me feel special at every single phase of my life. My friend, Arjun Poddar has been a source of overwhelming support throughout this journey. Thank you for believing in my abilities and relentlessly encouraging me to pursue my dreams.

I am thankful to my past and present group members, Emily Hellerich, Rui Liu, Min Cai, Teng Xiao, Ying Chen, Weipan Cui, Fadzai Fungura, Chamika Hippola, Dusan Danolovic, Rajiv Kaudal for their friendship and support. I am grateful to Emily, Rui, Teng and Min for being great mentors to me, it allowed a smooth transition to this group and the field of

www.manaraa.com

OLED at the beginning my research. I would like to extend my special thanks to Wai Lung and Joong-Mok Park for their collaborative work and immense help with the lab equipment troubleshooting. I have learnt a lot from them. I would also like to thank Moneim for teaching me to use the AFM set up with great patience.

I am thankful to the administrative staff Lori Hockett, Gloria Oberender, Larry Stolenberg and Vicky Thorand-Oster for their help and support. I am grateful to Ames Laboratory, US Department of Energy, Department of Physics and Astronomy and Department of Electrical and Computer Engineering for supporting my research at Iowa State University. This work was partially supported by the U.S. Department of Energy (DOE), Basic Energy Sciences, Division of Materials Science and Engineering, at the Ames Laboratory under contract number DE-AC02-07CH11358. The Ames Laboratory is operated for the DOE by Iowa State University.

www.manaraa.com

ABSTRACT

Organic light emitting diodes (OLEDs) have been widely used in commercial display technologies and are surpassing the competitors such as LCD or plasma displays in popularity. While OLEDs are excellent candidates for lighting as well for potential lower costs, compatibility with flexible substrates**,** and their characteristic warm and diffused light, challenges remain to be resolved before employing them in high brightness application. In this dissertation, several techniques are employed to address the major issues in the OLED technology for solid state lighting (SSL) applications and analytical on-chip sensing. To improve the light extraction from OLEDs, novel plastic substrates with nano-patterns were utilized along with a polymer anode. PEDOT:PSS (Poly(3,4-ethylenedioxythiophene)-poly(styrenesulfonate)) anode was spin-coated and rest of the materials were thermally evaporated to achieve a corrugated OLED conformally coated on the patterned substrates. With the corrugated OLEDs fabricated on patterned substrates, enhanced light extraction (50%-100%) was achieved over flat OLEDs. The challenges of achieving conformal coating of such substrates and their effects on the device reliability were evaluated, a potential solution was discussed to address this issue as well. Furthermore, the device architecture of white OLEDs was also modified to achieve desired color coordinates and its stability with increasing voltage. A near ultra-violet microcavity (μc) OLED was utilized as the excitation source to achieve higher dynamic range in oxygen sensing experiment with organic photodetector. A CBP(4,4′-Bis(*N*-carbazolyl)-1,1′-biphenyl)-based combinatorial array of μc OLEDs was fabricated by varying the thickness of the organic layers to obtain nine sharp, discrete emission peaks from 370 to 430 nm, which were employed in an all-organic on-chip spectrophotometer and absorption measurement of a common dye was demonstrated with set up.

www.manaraa.com

CHAPTER 1.

INTRODUCTION TO OLEDS

1.1. Brief History of OLED Technology

In the early 1950's, A. Bernanose and coworkers at the Nancy-Université in France first discovered electroluminance (EL) in organic materials by applying a high alternating voltage to acridine derivatives deposited on a cellophane thin films. [1] In 1963, W. Helfrich & W.G. Sneider demonstrated EL from anthracene single crystal [2] for the first time utilizing the invention of ohmic, dark-injecting electrodes by Pope's group in 1960. [3] EL from a thick polymer PVK (Poly (9-vinylcarbazole)) layer was also reported with hole-electron injecting electrodes in 1983. [4] However, these devices were not of practical interest due to the high driving voltage needed for their operation, to compensate for the low conductivity of the materials.

In 1987, Ching W. Tang and Steven Van Slyke developed the world's first working OLED at Eastman Kodak with a NPB (N,N′-Di(1-naphthyl)-N,N′-diphenyl-(1,1′-biphenyl)-4,4′-diamine)/Alq_3 (Tris-(8-hydroxyquinolinato)aluminum) bilayer heterojunction structure[5]. The OLED demonstrated peak external quantum efficiency (EQE) of 1% with maximum brightness exceeding 1000 Cd/m^2 at ~10V. After that, Friend and coworkers reported the first polymer LED (PLED) based on PPV [6].These researches drew attention toward potential commercial applications of OLEDs and thus considerably enhanced the research interest in OLED technology. The first flexible OLED was demonstrated in 1992 by Gustafsson *et al.* on a polyethylene terephthalate (PET) substrate with a polyaniline (PANI) anode for hole injection[7]. The first white OLED was demonstrated by Kido et al.; [8] which shows a high brightness (~3400 Cd/m^2) a broad

www.manaraa.com

visible-range spectrum, which eventually pushed the research to OLED applications in solid state lighting, displays, and sensing.

A significant milestone was achieved by the groundbreaking work on PtOEP (Platinum octaethylporphyrin)-based phosphorescent OLEDs by Forrest and coworker in 1998 [9].The efficiency of a fluorescent OLED is typically restricted to 25% because the light is produced only by singlet excitons (SE) and not by the 75% triplet excitons (TE) due to the forbidden triplet to ground state singlet radiative transition. Using PtOEP as the emissive material enabled utilization of both singlet and triplet excitons' emission due to large spin-orbit coupling in the presence of the heavy metal that enabled achieving ~100% internal quantum efficiency (IQE).

Following the introduction of the first commercial OLED display by Pioneer in 1997[10], the technology continues to mature. Despite several challenges, such as the OLEDs' short lifetime and the intrinsic light loss within the device, tremendous research effort in this field led the OLED technology to be one of the leading display technologies in the high end consumer electronics market.

1.2. OLED Structure

OLEDs are generally fabricated on glass or plastic substrates. They consist of multiple organic layers sandwiched between two electrodes with matching work-functions for electron and hole injection. The state of the art OLEDs typically include a hole injection layer (HIL) on the anode, followed by a hole transport layer (HTL), an emissive layer (EML), an electron transport layer (ETL), an electron injection layer (EIL), and a cathode. Additional layers include hole and electron blocking layers (HBL/EBL), but generally HTLs and ETLs are chosen so that they can simultaneously work as EBL or HBL,

www.manaraa.com

respectively. **Figure 1.1** shows the schematic of a standard device structure and the energy band diagram of an OLED.

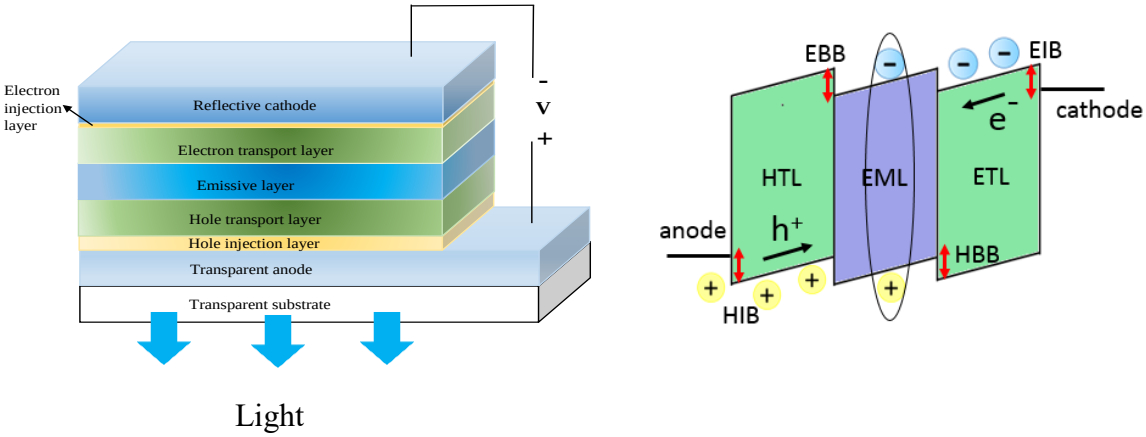

Figure 1.1: Schematic of a standard bottom emitting OLED (left) and the energy band diagram of a simple OLED structure (right)

One of the electrodes in OLED stack has to be transparent or semi-transparent to extract light from the device. Indium Tin Oxide (ITO) is very popular as the transparent anode in OLED field due to its uniform transparency over the visible wavelength range. Another important aspect of choosing anode is its work function (φ_f). To efficiently inject holes into HIL/HTL, metals or metal oxide with high φ_f is desirable. For example, φ_f of ITO is -4.7 eV while that of a polymer anode is as high as -5.2 eV. ITO's φ_f can be increased by e.g., by treating its surface with UV ozone for 5 minutes; alternatively, chlorinated ITO that has higher φ_f can be utilized. [11-12].

In contrast, metals for the cathode should have a lower work function to inject electron efficiently to the ETL. Lithium fluoride (LiF), Liq, CsF, or Cs_2CO_3 are typically used as the EIL. It is believed that Li+ ions dope an ETL layer like Alq_3 and enhance electron mobility. EIL can also reduce the electron injection barrier (Figure 1.1) due to band bending at the cathode-dielectric interface [13-14].

www.manaraa.com

There are different OLED geometries, such as microcavity, top emitting, and transparent OLEDs, in addition to the standard bottom emitting structure, where light generated in the EML is emitted through the bottom glass or plastic substrate.

In microcavity OLEDs, a semi-transparent thin metal anode replaces the transparent ITO or polymer anode. The two metal electrodes produces an optical cavity that enables tuning the peak wavelength of the OLED. The semi-transparent metal anode is useful in getting sharp and strong emission in the normal direction as compared to the conventional Lambertian emission from transparent anodes [15]. Microcavity devices are discussed in greater detail later in the chapter.

In top emitting OLEDs, which are microcavity OLEDs, the light is emitted from a top semi-transparent cathode. These devices are well suited for display applications, where the opaque anode can be well integrated with TFT backplane [16-17].Transparent OLEDs use transparent materials for both the cathode and anode [18].This geometry significantly enhances the contrast in the display matrix as there is no reflection of light from a reflective anode under daylight conditions.

Inverted OLEDs, with a thick cathode as the bottom electrode, are particularly advantageous for some specific applications in the active matrix setting. Stacked and Tandem OLEDs consist of multiple OLED structures fabricated on top of each other and connected in series [19].The advantage of tandem OLEDs lies in the fact that multiple photons can be generated by injecting a single electron-hole pair into the device. Thus significantly enhancing the current efficiency. Though for these devices longer lifetimes were reported, the power efficiency is too low reducing their practical applications. Several mixed host phosphorescent OLEDs are reported demonstrating better charge transfer and

www.manaraa.com

exciton confinement in the emissive layer that leads to higher efficiency devices [20].It was reported also that graded doping of the emissive layer enhances the lifetime of blue phosphorescent OLEDs by 10x [21].Moreover, it was shown that the degradation of blue phosphorescent material reduced when the dopant concentration was higher close to the HTL and gradually decreased towards the ETL. Graded junctions are also reported to have higher stability and lifetime.

1.3. Operating Principles

1.3.1. Organic semiconductors: π-conjugated materials

Organic semiconductors are typically π-conjugated organic compounds. The conjugation comes from alternating single and double bonds through the molecule or the polymer backbone. Double bonds in C-atoms are formed by sp^2 hybridization. In sp^2 hybridization, 2*s* and two 2*p* (p_x and p_y orbitals) orbitals are hybridized to form strongly localized sigma (σ) bonds aligning three equal energy *sp* orbitals in a triangular planar structure with an angle of 120° between them. The remaining p_z orbital forms a π bond with another adjacent p_z orbital, which is perpendicular to the σ-bond plane as shown in **Figure 1.2**. As these π bonds are much weaker than σ-bonds, the electrons associated with these bonds are delocalized and comparatively free to hop from one molecule to another. These delocalized electrons in π bonds contribute to the relatively high conductivity and semiconducting properties of the π-conjugated materials.

www.manaraa.com

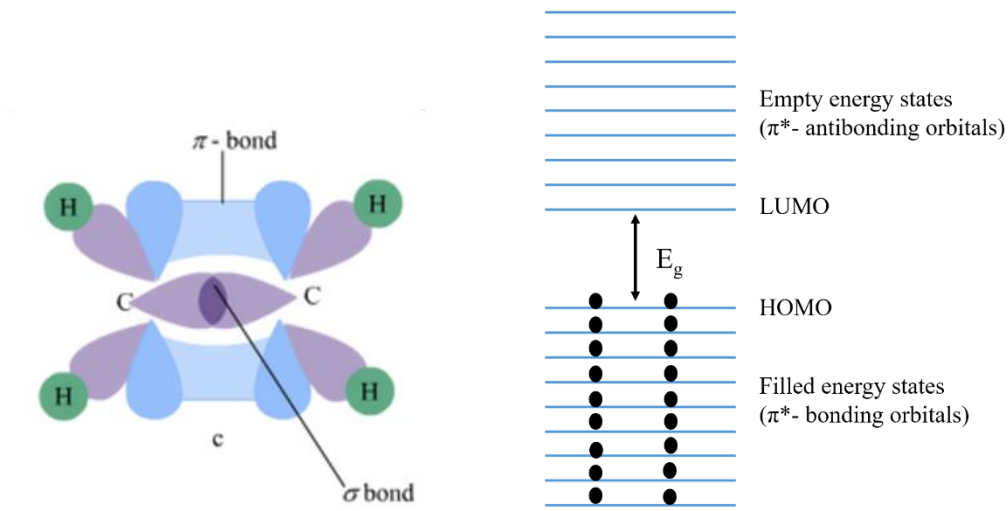

Figure 1.2: Schematic of a simple molecule with sp^2 hybridization (left) and HOMO-LUMO energy levels (right) [22]

The semiconductor like band structures in π -conjugated materials can be explained with the help of Molecular Orbital (MO) theory. According to one of the MO theories, the molecular orbital wave function of a π-bond can be expressed as a linear combination of atomic orbital wave functions and the linear coefficients will be determined by minimizing the total energy of the system. For example, two p_z orbitals result in splitting into two energy levels bonding and anti-bonding molecular orbitals. According to the Pauli Exclusion Principle, every energy state can be occupied by two electrons. Thus the electrons will occupy only the ground state (bonding) of the π-orbital. Similarly, in a molecular system with more carbon atoms, the two bonding and anti-bonding energy levels form quasi-continuous energy bands. All the energy levels associated with bonding orbitals will be occupied by electrons whereas the energy levels associated with the antibonding orbitals will remain empty. The highest energy occupied molecular orbital (HOMO) and lowest energy unoccupied molecular orbital (LUMO) are analogous to the top of the valence and the bottom of the conduction band. **Figure 1.2** (right) shows the schematic

www.manaraa.com

representation of the molecular orbital splitting and HOMO-LUMO formation in π - conjugated materials.

1.3.2. Carrier injection from metal to organic semiconductors

Carrier injection in OLEDs is a crucial factor in producing high efficiency devices with longer lifetime. In an ideal case, ohmic contacts are desired to reduce the operating voltage of the device. For ohmic contacts, where the interface barrier energy is small, the number of injected carriers/second is always larger than the organic semiconductors can transport and thus the charge transport is typically bulk limited transport, i.e., restricted by the carrier mobility of the material. But due to limited choice of electrode materials, mostly quasi-ohmic barriers are observed because of the larger energy barrier at the metal-organic interface. Also organic semiconductors are highly disordered and contain trap states. For these type of barriers, the electron or hole injection from metal electrodes to organic materials can be typically described by two models: thermionic emission and Fowler-Nordheim tunneling. When the contact between a metal and an organic semiconductor is established, the electrons or holes can hop into some trap states in the organics and an image potential is created. The image potential hen lowers the carrier injection barrier and the effective potential barrier seen by the a charge carrier under an electric field E is given by,

$$q\varphi_B(x) = q\varphi_m - qEx - \frac{q^2}{16\pi\epsilon x} \qquad 1.1$$

Where *x* is the distance between the charge carrier and metal/organic interface and φ_m is the work function of the electrode. As seen, the second and third terms correspond to potential barrier reduction due to the applied electric field and the image charge potential formed at the interface.

www.manaraa.com

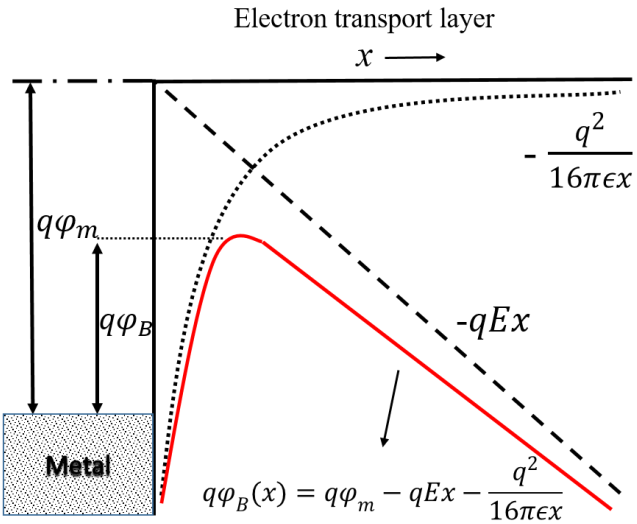

Figure 1.3: Effective energy barrier seen by an electron at the organic/metal interface as the energy barrier is lowered by the image charge at interface

Thermionic injection occurs at the metal/organic interface when the thermal energy of the charge carrier exceeds the energy needed to overcome the potential barrier. The thermionic injection current at temperature T is given by:

$$J_{Thermionic} = AT^2 e^{-\frac{q\varphi_B}{KT}} \quad 1.2$$

where A is the Richardson constant, which depends on the carrier effective mass. As the applied electric field increases, the triangular barrier becomes shallower and the field assisted tunneling or the FN tunneling become gradually important. The injection current due to the tunneling of carriers through a narrow triangular barrier can be expressed in the following form:

$$J_{FN\ Tunneling} \propto \frac{q^3}{4h\varphi_B} E^2 e^{-\frac{8\pi\sqrt{2m^*}\varphi_B^{1.5}}{3heE}} \quad 1.3$$

where the first term contains a tunneling pre-factor and the rate of current backflow. FN tunneling dominates the current injection when there is either very high field or very high potential barrier. Though there are several reports supporting thermionic injection and/or

www.manaraa.com

FN tunneling of carrier injection from metal to organics, there are several parameters that call for individual treatment for different interfaces. Direct chemical interaction between metal and organics, current backflow, injection into polaron levels etc. are to be considered in analyzing the current injection into an OLED in proper way. There can also be thermally activated hopping of charge carriers from the metal to the organics.

Transition metal oxides, like molybdenum oxide (MoO_3), are popularly used as hole injecting material to make the hole injection ohmic. Research shows that for a very thin such oxides in contact with a metal, chemical reaction between the metal and transition metal oxide occurs altering the electronic properties and energy level alignment of the oxide at the metal interface. For example, for MoO_3 at the metal interface MoO_x (x<3) and Mo^{+5} cations are formed instead of Mo^{+6}. This modification of the oxide layer lowers the fermi level of MoO_3 toward the conduction band and changes its electronic properties [23]. For a similar reason, a thin layer of some transition metal compounds, e.g., TiO_2 or Cs_2C0_3, can be is used as electron injecting material. For LiF, most commonly used as EIL, it is believed that chemical interaction occurs between Al and fluoride ion and Li^+ diffuses through the ETL yielding greater electron injection [24].

1.3.3. Charge transport

In contrast to the band-like charge transport observed in inorganic semiconductors, the charges in the organic materials are mainly localized and charge transport in these material takes place via hopping of charge carriers from one molecule to another. The localized energy states can be thought of as a series of potential wells that can trap a carrier. The carriers are typically trapped in localized states and hop from one potential well to another.

www.manaraa.com

The excess energy to overcome the energy barrier of the potential well, generally come from the lattice vibration (phonon-assisted) or the applied electric field.

As a result of the hopping transport, the drift mobility of charge carriers in the organic materials is very low in comparison to their inorganic counterparts, the drift mobility is typically of the order of 10^{-7} to 10^{-3} $cm^2V^{-1}s^{-1}$ for holes and even lower for electrons.[25-26] The charge transport in the organics is found to be thermally activated while the mobility of charge carriers are found to be dependent on the applied electric field. There are many proposed models such as the Poole-Frenkel model,[27] the small-polaron model[28] and the Gaussian disorder formalism[29-30] to explain the electric field and temperature dependence of carrier mobility in such disordered system. Except under strong electric field and high carrier injection, the best fitting mobility dependence on the electric field was derived with Poole-Frenkel formalism and as given by equation 1.4.

$$\mu(E,T) = \mu(0,T)\exp[\gamma\sqrt{E}] \qquad 1.4$$

Where μ(0,T) is the low field mobility and γ is empirically determined coefficient. μ(0,T) and γ are temperature dependent quantities that also rely on the energetic and positional disorder of the system suggested by the disordered formalism [30]. To explain the phenomena in a very simplistic way, they can be thought of as controlled by shallow traps present in the organic materials and at the interfaces. As the thermally assisted hopping of charge carriers increases with increasing temperature, the mobility also increases with increasing T.

As discussed in the previous section, the carrier injection at the metal/organic interface is strongly dependent on the energy barrier between the two materials. Similarly, charge hopping between two energy sites strongly depends on the energy difference and the

www.manaraa.com

distance between the two sites. The interface barrier can significantly vary from the expected value if there is chemical interaction between two materials and any morphological differences. The low current regime is mainly dominated by injection limited current and as the name suggests the current in this regime is strictly dependent on the interfacial energy barrier between metal-injection layers or between consecutive organic layers. The current in this injection limited current regime is given by the following equation [25]:

$$J \propto V^2 e^{-b/V} \quad 1.5$$

where b is the parameter dependent on the interface materials. Under higher electric field when the charge injection is higher, the current is mainly limited by the low mobilities in the organic materials. Due to the low mobility of charge carriers, charges will be accumulated at the interface which in turn partly screens the electric field. This regime is known as the space-charge limited current (SCLC), in this case the current-voltage relationship is given by the following equation.

$$J \propto V^{\alpha} \quad 1.6$$

The operating regime of the device determines the value of α in the above equation. For SCLC regime, it is generally linear to quadratic. As the organic materials are highly disordered and filled with deep level trap states, with increasing electric field, the deep trap states start to fill leading to rapidly increasing current. The device thus enters into the trapped charge limited current (TCLC) regime with the current-voltage following the above relationship with high α ($7 \leq \alpha \leq 9$)[31].

www.manaraa.com

1.3.4. Exciton formation and recombination

The injected holes and electrons form more energetically favorable polaron or bipolaron states within the molecule. Coulombically-correlated positive and negatively charged polarons can combine to form an exciton. Due to low dielectric constants (ε ~3-5) for organic semiconductors as compared to inorganic semiconductors (ε > 10), mostly Frenkel excitons exist in OLEDs. For such excitons, both electrons and hole are generally localized on the same molecule with a high binding energy (~1 eV) and low binding radius (~ 10 Å). [32,33] The capture radius (R_c), defined as the distance where the coulombic attraction between the electron-hole pair will be equal to the thermal energy (kT, k is Boltzman constant and T is the absolute temperature), is given by equation (1.7).

$$R_c = \frac{e^2}{4\pi\epsilon\epsilon_0 kT} \qquad 1.7$$

To recombine, the electron-hole pair must be within the capture radius (typically ~ 15 nm for organic materials at room temperature) to gain enough coulombic energy to surpass the thermal energy. At high carrier injection in multilayer OLEDs, accumulated charges at the interfaces may lead to a strong localized electric field. If the field is close to the recombination zone, field-assisted exciton dissociation will result in exciton quenching and hence efficiency 'roll-off' of OLEDs at high brightness levels. Thus, charge balance is crucial for such devices for reducing charge accumulation at the interfaces and keeping accumulated charges far away from the recombination zone.

After an exciton is formed, it can decay either radiatively or non-radiatively to the ground state. As the spin states of the injected electrons and holes are statistically independent, in combining the electron-hole pair can form either the single singlet exciton (SE) state (total spin, $S = 0$) or one of three triplet exciton (TE) states ($S = 1$), consequently

www.manaraa.com

with 0.25 and 0.75 probabilities respectively. According to the spin selection rule of optical transitions, recombination is allowed only within similar spin configurations ($\Delta S = 0$) when the interaction between orbital and spin angular momentum is small. The ground state being a singlet state, spin conservation rule only allows SEs to decay radiatively to the ground state. This process of light emission by SEs is known as fluorescence. Since only 25% of the generated excitons are SEs, it limits the efficiency of a fluorescent OLED. The fluorescent decay is typically very fast and can vary from 0.1 ns – 100 ns.

However, if there is a heavy metal in the molecular structure, it introduces high spin orbit coupling due to large interaction between spin and orbital angular momentum. Under this condition, $\Delta S \neq 0$ transitions are no longer forbidden and that leads to radiative recombination of TEs to the ground state yielding 100% internal recombination efficiency. This process is known as phosphorescence. The large spin orbit coupling due to the presence of the heavy metal in the molecule also enhances the probability of intersystem crossing (ISC),[9] non-radiative transitions from SEs to TEs as shown in the **Figure 1.4**. Phosphorescence materials thus utilizes both SEs and TEs for radiative recombination achieving the theoretical efficiency of 100% for such devices. However, ISC often is a slower process as compared to the internal conversions (IC), the phosphorescence decay time typically ranges from 1 μs to 10s.

Although the theoretical limit for fluorescent OLED efficiency is 25%, there are proposed theories that suggests the capture cross section for SE formation is higher than TEs.[34] Efficiency exceeding 25% limit for fluorescent small molecule devices are experimentally observed as well. It is believed to be due to the conversion of TEs to SEs due to triplet-triplet annihilation (TTA) process described in the following equation.

www.manaraa.com

$$T^* + T^* = S^* + S \qquad 1.8$$

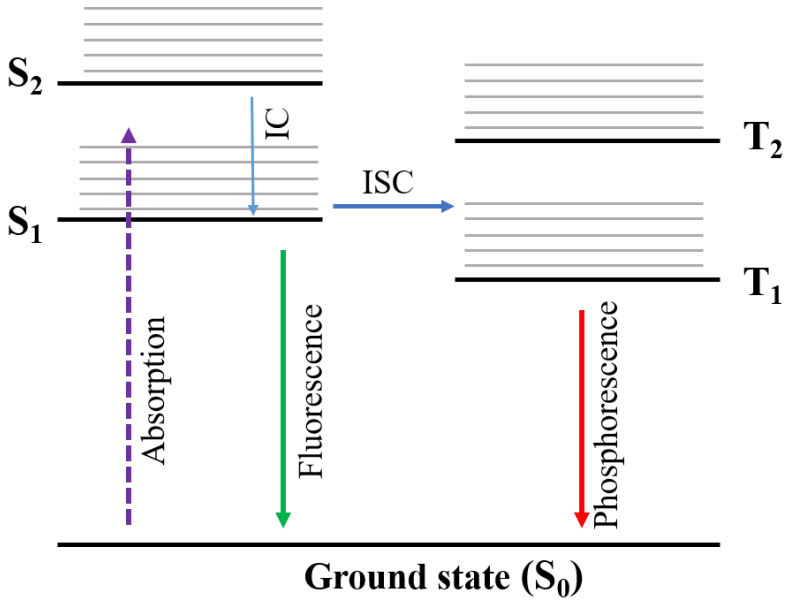

Figure 1.4: Jablonski diagram, possible transitions between different energy levels of organic molecules

There are two energy transfer processes that occur in light sensitive materials, radiative and resonance energy transfer. In radiative energy transfer the acceptor molecule absorb the photon emitted by the donor molecule when there is an overlap between the absorption spectra and emission spectra of the acceptor and donor materials respectively. In contrast, for resonance energy transfer, there is no actual photon emission and reabsorption by the donor-acceptor molecules. Typically the energy transfer is initiated due to the interaction between donor and acceptor molecules, it can be coulombic (Förster Energy Transfer or FRET) or electron exchange (Dexter Energy Transfer or DET) interaction. **Figure 1.5** shows the schematic of FRET and DET processes in a guest-host configuration in OLED.

www.manaraa.com

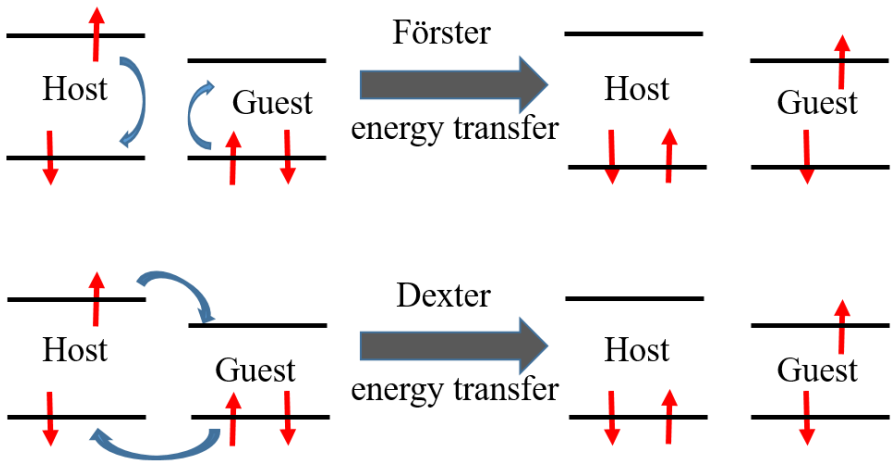

Figure 1.5: Schematic of Förster and Dexter energy transfer

In FRET, excitons are generated in the host molecule and induce dipoles in the guest molecule. The energy transfer occurs through a non-radiative dipole-dipole coupling between the inducing exciton donor field and induced acceptor field. [35] The efficiency of the FRET processes is very sensitive to the distance between acceptor and donor molecules and can be described by the following equation.

$$K_{FRET} = \frac{1}{\tau_H}({}^{R_0}/_{R})^6 \qquad 1.9$$

Where τ_H is the exciton lifetime for hole molecule, R is the distance between the host and guest molecules and R_0 is Förster radius that depends on the overlap integral of the donor's emission spectra with acceptor's absorption spectra. FRET occurs when the distance between donor-acceptor molecules is within the range of 1-10 nm.

Unlike FRET, DET occur through excited electron transfer from donor molecule to acceptor molecule. Since it's a direct electron exchange, the process requires wavefunction overlap between donor-acceptor molecules. Therefore DET is a short range mechanism, i.e., occurs only when the distance between donor-acceptor molecules is very small (typically <1 nm) and the rate of the energy transfer is given by the following equation.

www.manaraa.com

$$K_{DET} \propto Jexp(-\frac{2r}{L}) \quad 1.10$$

Where *J* is the spectral overlap integral between donor-acceptor molecules, *r* and *L* are the distance and sum of the Van der Waals radii of the donor-acceptor molecules respectively. It is observed mostly in phosphorescent OLEDs. Spin conservation is FRET is ΔS=0 whereas in DET, triplet to singlet or singlet to triplet is allowed.

1.4. Light Extraction and OLED Efficiency

High OLED Efficiency is crucial for reducing energy consumption and improving device performance. Efficiencies are generally expressed in terms of luminous efficiency and power efficiency with the units Candela/Ampere (Cd/A) and (Lumen/W), respectively. These efficiencies in general measure the light flux generated in the forward direction per unit electrical energy input. However, the measurement of light flux greatly depends on the light perception of human eyes, which is described by the luminosity function shown in **Figure 1.6**. The human eye is most sensitive to λ=555 nm and the perception goes down with the change of wavelength on either side of the peak. For example, the perception of human eye at λ =380 nm, where the ultra violet (UV) region starts, is almost zero. As a result, a blue OLED will seemingly have a lesser brightness and efficiency when compared to a green OLED, even if they are emitting the same amount of power.

www.manaraa.com

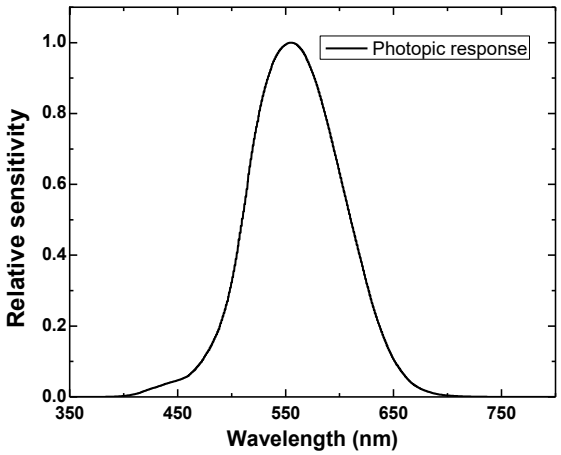

Figure 1.6: Luminosity curve or photopic response of the human eye, CIE 1978

Thus, it is very important to use a different measure of efficiency when comparing OLEDs with different EL spectra. The external quantum efficiency (EQE, η_{EXT}) of an OLED is given by the number of photons generated per electrical charge injected without taking the emission wavelength into account (equation 1.11). [25]

$$\eta_{EXT} = \eta_{OUT} * \gamma * r_{ex}\eta_{PL} \qquad 1.11$$

Where η_{PL} is the PL quantum yield, r_{ex} is the fraction of singlet or triplet excitons generated, γ is the charge balance factor, and η_{OUT} is the outcoupling efficiency. For phosphorescent OLEDs all three factors except η_{OUT} can be optimized to 1. The outcoupling factor depends on the refractive index (RI) matching of the organic layers, the anode, and the substrate as well as on surface plasmon excitation-related losses at the metal cathode. An oversimplified estimation of η_{OUT} is given by equation-1.12.

$$\eta_{out} \approx {}^{1}/_{n^2} \qquad 1.12$$

where *n* is the effective refractive index of the organic stack. With RI of organics being ~ 1.7, only ~17-20% of the light generated inside can be extracted for a standard ITO/glass

www.manaraa.com

OLED. About 30% of the photons are lost in the substrate mode due to total internal reflection (TIR) at the glass/air interface. The rest of 50-53% photons are trapped in the organics and lost via surface plasmon excitation at the organic/cathode interface. [36-37]Extensive research is ongoing in an attempt to extract these lost photons. It is easier to extract the light trapped in the substrate by using an external macrolens or microlens array (MLA) at the back of the glass or plastic substrate. It is a very effective method, as MLA attached on the back of the substrate does not affect the device performance while extracting most of the trapped light from the substrate. Extracting light trapped in the organics and lost to surface plasmon excitation remains a challenge. One approach to overcome the latter issue is to fabricate an extraction layer between substrate and anode. [38-39] Such a layer can adversely affect the device performance. However, thorough research addressing this issue enabled significant light extraction. Light extraction is discussed in greater detail in Chapter 2.

1.5. OLED Fabrication Techniques

Two major techniques are used to fabricate OLEDs, i.e., thermal vacuum deposition and solution processing. Irrespective of the fabrication methods, all OLEDs must be fabricated in an inert atmosphere with very low oxygen and humidity level.

Thermal vacuum deposition is the most common and proficient technique to fabricate efficient OLEDs. Most commercial grade small molecule OLEDs (SMOLEDs) are fabricated by this method. In this technique, organic/inorganic materials required for the device are thermally evaporated in a vacuum chamber with a base pressure of ~10^{-6} mbar. Materials are heated in crucibles/baskets for evaporation and the deposition occurs when the materials come into contact with the substrate placed at the top of the vacuum chamber.

www.manaraa.com

Layer thickness can be controlled precisely by monitoring the thickness with a piezoelectric crystals along with various shutters to enable evaporation of a specific material. Multilayered device fabrication, as well as patterning to generate pixels are much easier with this technique. Additionally, for small area applications, thermal evaporation yields uniformly coated substrates of highly reliable OLEDs. However, the size of OLED panels is restricted, as a larger system introduces non-uniformity in the organic films, which reduces the device quality.

Polymers are more likely to degrade fast when subjected to high temperature. For that reason, polymer OLEDs (PLEDs) are generally fabricated using solution processing techniques, such as spin coating. In this method, materials are dissolved in appropriate solvents in specific concentrations and the solution is dispensed onto the substrate. The substrate is then spun at a high speed (500-6000 rpm). During the spinning, excess solution is thrown off, and then the substrate is baked to get rid of excess solvent trapped in the film. The concentration of the material in the solution and the spin speed determine the thickness of the film. However, it is difficult to control the precise thickness of the film deposited by the process, and fabricating multilayered devices is challenging due to the limited number of orthogonal solvents.

Although thermal evaporation and spin-coating are the two main fabrication methods practiced in research labs and industry, there are several other methods developed in order to overcome the shortcomings of these two methods. For example, organic vapor deposition, where material is transported by a carrier gas, was developed in order to overcome the limitation of thermal vacuum deposition for large area applications. In this case, the materials to be deposited are transported by the carrier gas to a cold targeted

www.manaraa.com

substrate, which allows for better control and increases material utilization significantly. Inject printing is a cost-effective alternative to spin-coating for large scale production. In this method low cost inject printers are used, droplets from the desired solution are formed at the nozzle and then driven by electric field toward the substrate. In order to reduce the manufacturing cost of OLED panels, roll-to-roll processing is a potential solution. However, this process is still under development.

1.6. Dissertation Organization

This dissertation is comprised of six chapters. Chapter 1 provides a general introduction to Organic Light Emitting diodes (OLEDs), their basic operating principles, and characteristics relevant to the work presented. The rest can be broken down into two parts. The first part focuses on enhancing the efficiency of OLEDs, particularly the light extraction, whereas the second part demonstrates the application of OLEDs in optical analytical applications and its integration with Organic Photo-detectors (OPDs) to achieve lab-on-chip sensing. Chapter 2 to chapter 5 are mostly modified from the papers that have already been published or from manuscripts under preparation.

Chapter 2 addresses the light out-coupling issues of OLEDs and focuses on enhancing the light extraction from OLEDs by introducing novel plastic substrates and a polymer anode. The challenges of using nano-patterned substrates and fabricating conformal OLEDs on them are also discussed. The work on light extraction of OLEDs continues to chapter 3. In this chapter emphasis was given to fluorescent white OLEDs for solid state light (SSL) applications utilizing the nano patterned plastic substrates mentioned in chapter 2. OLED fabrication and characterization was performed by the author, except for the experiment of pattern height optimization, which was performed by Dr. Teng Xiao.

www.manaraa.com

Chapter 4 provides an overview of recent progress on integration of OPDs with different optoelectronic components in various optical analytical applications. A general introduction to the operating principles and experimental set up are also provided. The review mainly focuses on chemical and biological optical sensing platforms highlighting the use of OPDs. This review paper was co-written by the author and Dr. Ruth Shinar, with the first draft written largely by the author. Dr. Teng Xiao wrote part of the section regarding 'the general characteristics of the organic photodetectors'. This review was published on *Electronics* in September 2015.

A new approach is demonstrated in chapter 5 to fabricate a narrow band emission near-UV microcavity (μC) OLED with peak emission wavelength near 385 nm. The work makes an effort to realize the integration of OLEDs and OPDs in optical analytical applications with enhanced signal to noise ratio and improved limit of detection. Furthermore, a combinatorial array of μC OLEDs with variable peak emission wavelengths is demonstrated and subsequently employed as an on-chip spectrophotometer integrated with an OPD. The fabrication and characterization of all the OLEDs as well as those of the sensing films were performed by the author, including all the experiments with the compact sensor setups. The fabrication and characterization of the organic photovoltaic devices were done by Dr. Fadzai Fungura. The simulation work on the combinatorial array supporting the experimental results was performed by Dr. R. Biswas. This work was published on *Advanced Functional Material* in January 2015. Part of this work (presented as an invited talk) was also published in the Proceedings of the SPIE, 2015. Finally Chapter 6 summarizes the results of different projects presented.

www.manaraa.com

1.7. References

[1] A. Bernanose, M. Comte, P. Vouaux, *J. Chim. Phys.* **50**, 64 (1953); A. Bernanose, P. Vouaux, *J. Chim. Phys.* **50**, 261 (1953); A. Bernanose, *J. Chim. Phys.* **52**, 396 (1955); A. Bernanose, P. Vouaux, *J. Chim. Phys.* **52**, 509 (1955).

[2] H. Kallmann, M. Pope, *J. Chem. Phys.* **32**, 300 (1960); H. Kallmann, M. Pope, *Nature* **186**, 4718 (1960); M. Pope, H. P. Kallmann, P. Magnante, *J. Chem. Phys.* **38**, 2042 (1963).

[3] P. Mark, W. Helfrich, *J. Appl. Phys.* **33**, 205 (1962); W. Helfrich, W. Schneider, *Phys. Rev. Lett.* **14**, 229 (1965).

[4] R. Partridge, *Polymer* **24**, 733 (1983); R. Partridge, *Polymer* **24**, 739 (1983); R. Partridge, *Polymer* **24**, 748 (1983); R. Partridge, *Polymer* **24**, 755 (1983).

[5] C. W. Tang, S. A. Vanslyke, *Appl. Phys. Lett*. **51**, 913 (1987)

[6] J. H. Burroughes, D. D. C. Bradley, A. R. Brown, R. N. Marks, K. MacKay, R. H. Friend, P. L. Burns, A. B. Holmes, *Nature* **347**, 539 (1990).

[7] G. Gustafsson, Y. Cao, G. M. Treacy, F. Klavetter, N. Colaneri, A. J. Heeger, *Nature* **357**, 477 (1992).

[8] J. Kido, K. Hongawa, K. Okuyama, K. Nagai, *Appl. Phys. Lett.* **64**, 815 (1994).

[9] M. A. Baldo, D. F. O'Brien, Y. You, A. Shoustikov, S. Sibley, M. E. Thompson, S. R. Forrest, *Nature* **395**, 151 (1998).

[10] Tohoku Pioneer Corporation, http://pioneer.jp/en/info/globalnetwork/japan/tohokupioneer/mainbusinesses/oled/

[11] D. J. Milliron, I. G. Hill, C. Shen, A. Kahn, J. Schwartz, *J. Appl. Phys.* **87**, 572 (2000).

[12] F. Nüesch, E. W. Forsythe, Q. T. Le, Y. Gao, L. J. Rothberg, *J. Appl. Phys.* **87**, 7973 (2000).

[13] L. S. Hung, C. W. Tang, M. G. Mason, *Appl. Phys. Lett.* **70**, 152 (1997).

[14] G. E. Jabbour, B. Kippelen, N. R. Armstrong, N. Peyghambarian, *Appl. Phys. Lett.* **73**, 1185 (1998).

[15] J. Shinar, R. Shinar, *J. Phys. D: Appl. Phys.* **41**, 133001 (2008).

[16] G. Gu, V. Bulović, P. E. Burrows, S. R. Forrest, M. E. Thompson, *Appl. Phys. Lett.* **68**, 2606 (1996)

[17] H. Riel, S. Karg, T. Beierlein, B. Ruhstaller, W. Rieß, *Appl. Phys. Lett.* **82**, 466 (2003)

www.manaraa.com

[18] P. Görrn, M. Sander, J. Meyer, M. Kröger, E. Becker, H.-H. Johannes, W. Kowalsky, T. Riedl, *Adv. Mater.* **18**, 738, (2006)

[19] L. S. Liao, K. P. Klubek, C. W. Tang, *Appl. Phys. Lett.* **84**, 167 (2004)

[20] J. Lee, J.-I. Lee, J. Y. Lee, H. Y. Chu, *Appl. Phys. Lett.* **94**, 193305 (2009)

[21] Y. Zhang, J. Lee, S. R. Forrest, *Nat. Commun.* **5**, 5008 (2014).

[22] Chapter 4 Chemical bonding and molecular structure (2013), https://vakir.Wordpress .com/2013/09/30/6-sp2-hybridization/

[23] M. T. Greiner, L. Chai, M. G. Helander, W.-M. Tang, Z.-H. Lu, *Adv. Funct. Mater.* **23**, 215, (2013)

[24] H. Heil, J. Steiger, S. Karg, M. Gastel, H. Ortner, H. von Seggern, M. Stößel, *J. Appl. Phys.* **89**, 420 (2001)

[25] J. Shinar, V. Savvateev, in Organic Light-Emitting Devices: A Survey, ed. J. Shinar, Springer, New York, (2004) ch. 1.

[26] F. So, ed., Organic Electronics: Materials, Processing, Devices and Applications (CRC, 2010).

[27] J. Frenkel, *Phys. Rev.* **54**, 647 (1937).

[28] T. Holstein, *Appl. Phys.* (N.Y.) **8**, 325 (1959); **8**, 343 (1959);

[29] H. Bâssler, *Phys. Stat. Sol (b)* **175**, 15 (1993)

[30] Y. Gartstein, E.M. Conwell, *Chem. Phys. Lett.* **245**, 351 (1995)

[31] M. Pope, C. E. Swenberg, Electronic processes in organic crystals and polymers, 2nd Ed., Oxford University Press, 1999.

[32] M. Knupfer, *Appl. Phys. A* **77**, 623 (2003)

[33] W. Li, Y. Pan, R. Xiao, Q. Peng, S. Zhang, D. Ma , F. Li, F. Shen, Y. Wang, B. Yang, Y. Ma, *Adv. Funct. Mater.* **24,** 1609 (2014)

[34] M. Wohlgenannt, Kunj Tandon, S. Mazumdar, S. Ramasesha, Z. V. Vardeny, *Nature* **409**, 494 (2001)

[35] M. Pope, C. E. Swenberg, Electronic processes in organic crystals and polymers, 2nd Ed., Oxford University Press, (1999).

[36] M. Cai, Z. Ye, T. Xiao, R. Liu, Y. Chen, R. W. Mayer, R. Biswas, K.-M. Ho, R. Shinar, J. Shinar, *Adv. Mater.* **24**, 4337 (2012).

www.manaraa.com

[37] D. S. Mehta, K. Saxena, *Proc. of ASID '06* **198** (2006).

[38] J.B. Preinfalk, F. R. Schackmar, T. Lampe, A. Egel, T. D. Schmidt, W. Brütting, G. Gomard, U. Lemmer, *ACS Appl. Mater. Interfaces* 8, 2666 (2016).

[39] Q.-D. Ou, L.-H. Xu, W.-Y. Zhang, Y.-Q. Li, Y.-B. Zhang, X.-D. Zhao, J.-D. Chen, J.-X. Tang, *Opt. Express*, **24**, 6 (2016).

www.manaraa.com

CHAPTER 2

ENHANCED LIGHT EXTRACTION EFFICIENCY OF OLEDS WITH CONFORMALLY COATED PEDOT:PSS ON NANO-PATTERNED POLYCARBONATE SUBSTRATES

Abstract

In this paper, we report an enhancement in light outcoupling from bottom emitting organic light emitting diodes (OLEDs) using corrugated polycarbonate (PC) substrates. A simple way to develop a needed conformal, solution-processed, multilayer PEDOT:PSS (poly(3,4-ethylenedioxythiophene) polystyrene sulfonate) anode on the nano-patterned PC substrates is demonstrated. We discuss how to achieve the optimal conformal polymer coating by controlling the parameters of the solution processing. Higher speed spin-coating for a longer duration was found to be beneficial for fabricating optimal thin PEDOT:PSS layers conformally on the plastic nano-patterns. We found that this thin conformal coating is key for attaining a uniform current distribution and hence better devices. Surface morphology and current distribution images of the PEDOT:PSS anode support this finding. Additionally, the outcoupling enhancement of devices fabricated on thin PEDOT:PSS/corrugated PCs was tested for OLEDs emitting at different colors and reproducibility and stability were evaluated, with reproducibility being the main issue. A potential solution to the reproducibility issue by use of a secondary semi-transparent anode along with PEDOT:PSS is proposed.

Keywords: solution-processed anode, conductive polymer, conformal coating, nano-patterned substrates, flexible substrates, OLEDs, light extraction, enhancement, AFM, FIB

www.manaraa.com

2.1. Introduction:

OLED technology is widely used in flat panel displays of small and large electronic devices as it provides thinner, brighter displays with vibrant colors and infinite contrast. Active matrix OLED (AMOLED) displays are consistently considered superior against their competitors. OLEDs are also developed for solid state lighting (SSL) applications. Unlike the bright point source emission of inorganic LEDs, OLEDs provide a warm and diffuse source of light that is by design suitable for large area illumination. The primary criteria for OLEDs for use in SSL are cost reduction and increased efficiency (the DOE goal is an efficiency of 70% by 2020), matching or exceeding the efficiency of the current alternatives, and stability.

The external quantum efficiency (EQE) of an OLED is given by equation 2.1. [1,2]

$$\boldsymbol{EQE = \eta_{out} * \gamma * r_{ex} * \Phi_{PL}} \qquad 2.1$$

Where γ and Φ_{PL} are the charge balance factor and intrinsic photoluminescence (PL) quantum yield, respectively, and can be adjusted to equal ~1 by carefully choosing the materials and device architecture. r_{ex} is the radiative exciton recombination factor, which is 0.25 for fluorescent materials and 1 for phosphorescent materials. As a result, when using phosphorescent materials as the emitting layer, almost 100% internal quantum efficiency (IQE) is achievable.[3] Although the power efficiency (or luminous efficacy) of OLEDs is now comparable to that of LEDs and fluorescent tubes due to the almost perfect IQE, the EQE of OLEDs suffers from trapped or waveguided light loss inside the device and in the substrate due to refractive index mismatch, as well as plasmon excitation-related loss, which restrict the forward light outcoupling and hence the efficiency. According to ray optics, the fraction of outcoupled light can be approximately calculated by the well-known

www.manaraa.com

formula, $\eta_{out} \approx 1/(2n_{org}^2)$ [2], where n_{org} is the effective refractive index of the organic stack. About 53% of the generated photons are lost by total internal reflection (TIR) and subsequent waveguiding and loss in the organic/ITO layers and in surface plasmon modes, and ~30% of the photons are trapped inside the glass substrate due to TIR at the air/glass interface and subsequently waveguided to the glass edges. Thus, only ~17 – 20% of the generated light is forward-extracted from an OLED with this conventional structure [4,5]. Extensive research has been performed in an attempt to improve light extraction via different approaches. To extract the light lost in substrate modes, various sizes of microlens arrays (MLAs) were attached at the back of the glass substrate [6,7], TiO_2 nanoparticles [8] were embedded in the substrates, or high index substrates [9] replacing glass were used. A maximal 2 fold enhancement was achieved with structured MLA, where the MLA area exceeded that of the OLED pixel [7]. In this work, enhanced extraction of light waveguided in the ITO/organics was achieved via fabrication of OLEDs on patterned polycarbonate with the OLED stack grown conformally on the patterned structure.

ITO is extensively used as the transparent anode in OLEDs because of its high transparent nature in the visible range and preferred work function for hole injection into the organics.[10] As we approach commercializing, the cost reduction of the manufacturing process of flexible electronics, e.g., decorative SSL panels and wearable devices, becomes more important. A potential major cost reduction technique is roll-to-roll (R2R) manufacturing of OLEDs. Conductive polymers such as PEDOT:PSS can play a crucial role as anodes in the R2R process in ambient environment. In addition to being compatible with R2R manufacturing, the polymer does not present a refractive index mismatch with other organic materials as is the case of ITO[11], resulting in more light extraction and less

www.manaraa.com

waveguided loss in the organic/anode layers[12]. Although PEDOT:PSS was initially used only as a buffer layer between ITO and the organic layers due to its low conductivity but efficient hole injecting properties from ITO to the organics [13,14], it gained popularity as a potential anode in OLEDs with the commercial availability of high conductivity PEDOT:PSS and when the conductivity of the deposited film was drastically enhanced upon spin coating the film from a PEDOT:PSS mixture with e.g., ethylene glycol (EG)[15,16]. Like EG, by adding DMSO (dimethyl sulphoxide)[17,18] as an additive to the PEDOT:PSS solution or by a post treatment of the film with sulfuric acid, the film's conductivity was enhanced significantly. [19,20] Research also shows that just rinsing the PEDOT:PSS film with EG after a short bake following the spin coating enhances the conductivity of the layer considerably[15]. In one explanation, the conductivity enhancement is believed to be due to partial dissolution and removal of PSS only by EG. By varying the ratio of the PEDOT and PSS in the solution, the conductivity of the film can also be controlled[21]. Cai et al. showed that a double layer PEDOT:PSS anodes treated with EG and fabricated by spin-coating at 3000 rpm for 30 s yielded superior anodes for green OLEDs compared to ITO[16]. However, the characteristics of the PEDOT:PSS film varies significantly between flat glass to flat plastic to nano-patterned plastic substrates. In this report, we investigated the factors that affect the conformal coating and conductivity of the polymer anode coated on a PC substrate and the resulting outcoupling enhancement in conformally-fabricated OLEDs.

www.manaraa.com

2.2. Results and Discussion:

2.2.1. Anode Fabrication

While double layered PEDOT:PSS on a planar glass substrate serves as an excellent alternative anode to ITO,[12] the wettability of the polymer's solution on a plastic substrate is poor. As a result the adhesion of the PEDOT:PSS film to the substrate is inadequate and leads to potential film delamination, which results in the well-known non-emissive dark spots in the device.[22] In order to reduce the surface tension between the hydrophobic plastic substrate and PEDOT:PSS, the polymer solution has to be treated with an additive. Research shows that the wetting property improves when it is mixed with ethanol or fluorosurfactants. Adding ethanol increases the wettability of PEDOT:PSS on the polycarbonate substrates, but it reduces the conductivity significantly.[23] Upon addition of 25% or 50% ethanol to the solution, PEDOT:PSS was successfully deposited on a plastic substrate. However, the turn on voltage of a standard NPB (*N,N′*-Di(1-naphthyl)-*N,N′*-diphenyl-(1,1′-biphenyl)-4,4′-diamine)/Alq_3 (Tris(8-hydroxyquinolinato) aluminum OLED increased to 7.4 to 10.2 V in comparison to a turn on voltage of 2.9 V for a similar OLED on ITO/glass. In contrast, addition of a fluorosurfactant, e.g., Zonyl FS30 or Capstone FS35, reduces the surface tension considerably without affecting the conductivity of the PEDOT:PSS film[24]. Some studies even demonstrated an enhanced conductivity of PEDOT:PSS upon adding a fluorosurfactant at a very low concentration[25]. However, we did not notice any effect of the surfactant on the charge transport of a PEDOT:PSS film spin coated on the patterned substrate.

In this work, PEDOT:PSS solution was mixed with EG and 0.5-1% of Zonyl FS30 or Capstone FS35 fluorosurfactant. For a double layer PEDOT:PSS anode with each layer

www.manaraa.com

spin-coated at 3000 rpm for 30 s, a sheet resistance of 169 ohm/sq was achieved, which is slightly higher than the sheet resistance reported by Cai et al[12]. Though the sheet resistance can be further reduced by immersing the substrate/anode in an EG bath, it was not suitable for the current OLED design as the EG reduces the wetting between successive PEDOT:PSS layers, resulting in a non-conformal stack. A double layered PEDOT:PSS film fabricated as described above served as the anode for green and blue phosphorescent OLEDs.

2.2.2. Characterization of nano-pattern substrates

Substrates used in this work were mostly PCs, while some results for OLEDs on PET (polyethylene terephthalate) substrates are also shown. All PC substrates had dome-shaped nano-patterns (**Figure 2.1**) with the height of the features varying from 100 nm to 650 nm. The nano-patterns on the substrates are expected to produce corrugation throughout the OLED stack, which can be beneficial for extracting light trapped inside the device. This increased extraction is due to random changes of the incident angle at the organic+ITO/glass interface, which reduces the TIR.

The different substrates were imaged via atomic force microscopy (AFM) for height measurement. **Figure 2.1** shows AFM images of one of the nano-patterned PC substrates showing a 3D surface morphology and a pattern height of h ~320 nm.

2.2.3. Pattern optimization for green emitting OLEDs

To determine the optimal pattern height for maximum light extraction, green tris (2-phenylpyridine) iridium(III) ($Ir(ppy)_3$)-based phosphorescent OLEDs (PHOLEDs) with the structure PEDOT:PSS anode/MoO_3 (1 nm)/10% MoO_3:NPB (22.5 nm)/NPB (22.5 nm)/6% $Ir(ppy)_3$:CBP (11 nm)/BPhen (40 nm)/LiF (1nm)/Al (100 nm) were fabricated on different

www.manaraa.com

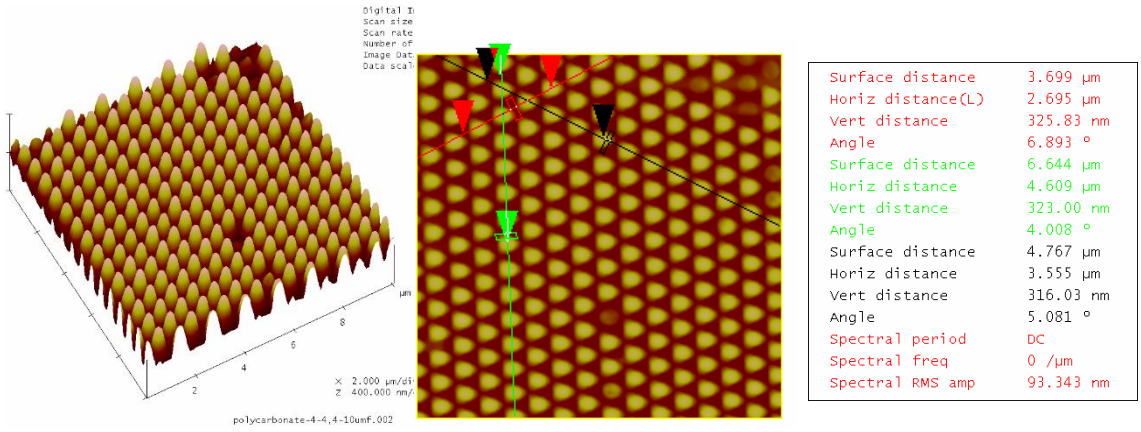

Figure 2.1: AFM images of a nanopatterned PC substrate with h ~320 nm: 3D surface morphology (left) and height measurement of the same substrate (right).

patterned PCs. The OLED layers were thermally evaporated on a spin-coated PEDOT:PSS anode. Enhanced light extraction was observed with patterned PCs with corrugation heights ranging from 250 nm to 320 nm as compared to a flat PC. A maximum luminous efficiency of 127 Cd/A was achieved for the device fabricated on the PC with the 320 nm pattern height and this efficiency was 1.5 fold higher than the luminous efficiency of the device fabricated on flat PC. **Figure 2.2** compares the electrical and optical characteristics for these devices.

The angular dependence of the electroluminescence (EL) spectra was also investigated for the green PhOLEDs. Though the intensity profile deviates slightly from a Lambertian profile as shown in Figure 2.2c, no significant change in the normal emission spectrum was observed (Figure 2.2d).

2.2.4. Blue emitting OLEDs on patterned PC

To further validate the enhanced light extraction from these corrugated structures, blue PhOLEDs were fabricated on substrate #14-0801-4 (which was identified as the substrate with the optimal feature height for the green PhOLEDs) with the device structure: 2 layered PEDOT:PSS/MoO_3 (5 nm)/di-[4-(N, N-di-p-tolyl-amino)-phenyl] cyclohexane (TAPC)

www.manaraa.com

(30 nm)/2% FIrpic:1,3-bis(carbazol-9-yl)benzene (mCP) (20 nm)/tris(2,4,6-trimethyl-3-(pyridin-3-yl)phenyl)borane (3TPYMB) (10 nm)/BPhen (40 nm)/LiF (1 nm)/Al (100 nm).[26] In addition to the optimized patterned PC (*h*~ 320 nm), another PC substrate with ~135 nm high features was also used to explore the correlation between the pattern parameters and the light extraction factor. The results are shown in **Figure 2.3**.

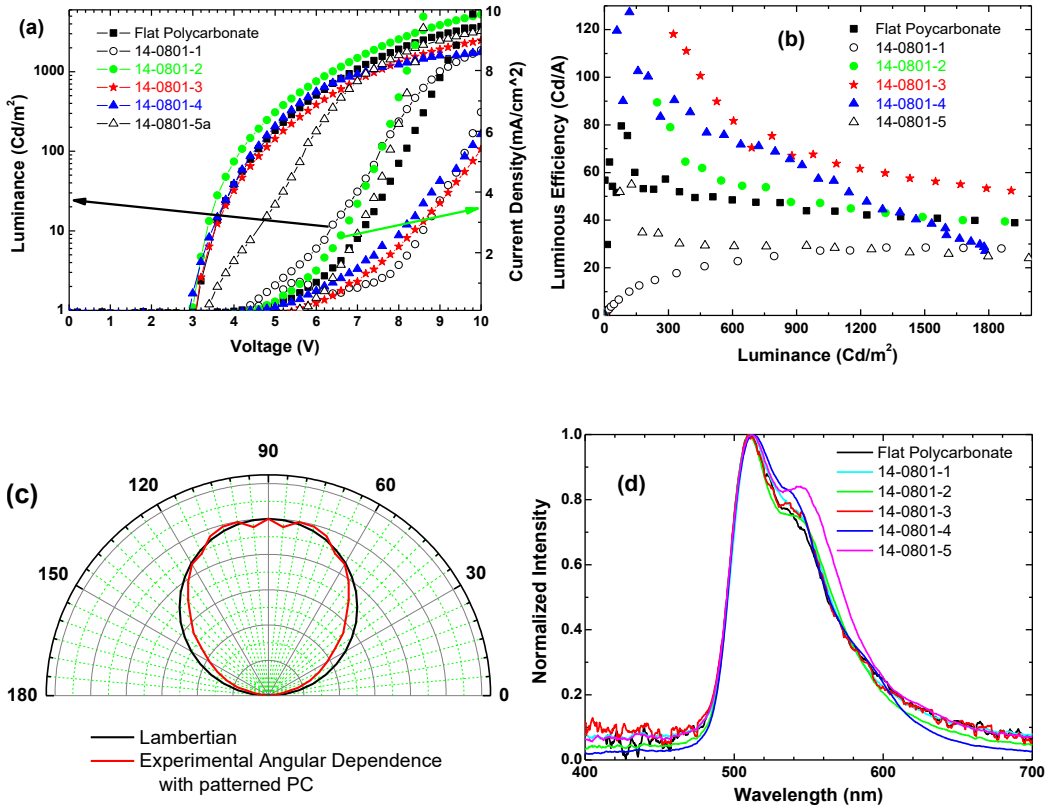

Figure 2.2: (a) J-L-V curves (b) luminous efficiency vs brightness (c) Comparison of angular distribution of EL spectra of OLEDs fabricated on patterned PC with ideal Lambertian profile and (d) normalized electroluminescence spectra for flat and patterned PC substrates; corrugation heights range from 215 nm to 500 nm.

As seen, a very similar current density profile is observed for both, the OLED on the substrate with the 135 nm high patterned and the flat PC. A 1.45 fold enhancement in light extraction was achieved and the maximum luminous efficiency was ~45 Cd/A. Interestingly, pattern #14-0801-4 resulted in a ~3 fold efficiency enhancement with a peak

www.manaraa.com

efficiency of 87 Cd/A; this efficiency is among the highest reported [27]. We note that the OLED on the ~320 nm patterned PC exhibited a steep roll-off in comparison to the flat PC and the PC with the ~135 nm high features. Most likely the reason for the faster roll-off is the larger surface area exposed to air (in the non-encapsulated devices) of patterned OLEDs in comparison to flat devices. Water vapor and oxygen can diffuse through the porous PC degrading more strongly the patterned device and quenching the electroluminescence. Figure 2.3d compares the spectra of these two corrugated devices with the flat PC; the spectral emission became narrower with increasing corrugation height in contrast to the spectral broadening observed for green PhOLEDs. This is likely due to the larger scattering angle of the green emission by the nanopatterned structure. As seen in Fig. 3e, the green shoulder in the EL spectrum of FIrpic increases with increasing angle, which is consistent with the reduced intensity of the green shoulder in the normal direction.

Table 2.1 lists the peak brightness and efficiencies for green and blue emitting devices fabricated on various substrates.

Table 2.1: Comparison of attributes of green and blue PhOLEDs fabricated on different substrates

	Sample	Pattern Height (nm)	Turn on voltage (V)	Max. luminous efficiency (Cd/A)	Corresponding EL (Cd/m^2)	Luminous Efficiency @ 1000 Cd/m^2
Green emitting OLEDs	Flat PC	0	3.0	80	79	44
	14-0801-1	~215	4.0	28	1321	27
	14-0801-2	~250	3.0	89	247	47
	14-0801-3	~280	3.0	118	323	64
	14-0801-4	~320	3.0	127	118	57

www.manaraa.com

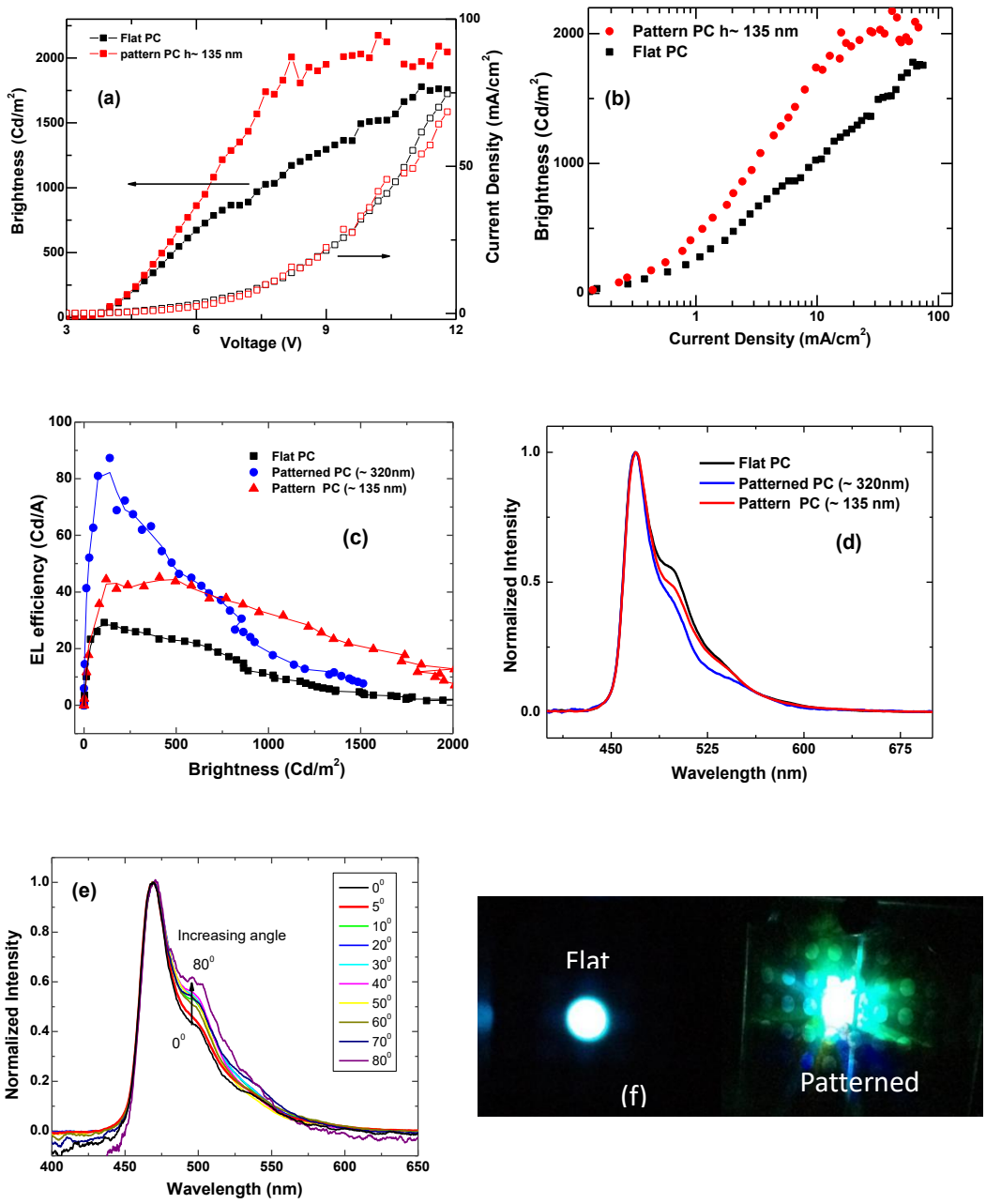

Figure 2.3: (a) J-L-V curves (b) brightness vs. current density curves for flat and inverse patterned PC (c) luminous efficiency vs brightness curves (d) normalized electroluminescence spectra of flat and patterned PCs with h~135 nm and h~ 320 nm. (e) Angular variation of EL spectra for patterned PC (h~ 320 nm) and (f) images of lit FIrpic OLEDs on flat and patterned substrates.

www.manaraa.com

2.3. Challenges with Corrugated OLEDs:

2.3.1. Evaluation of the conformal structure

As seen in Table 2.1, the highest luminous efficiencies achieved so far with the corrugated OLED structures were 87 Cd/A and 127 Cd/A for blue and green PHOLEDs, respectively, while the efficiencies of the reference OLEDs were ~30 Cd/A (blue PHOLED) and ~80 Cd/A (green PHOLED), however, these enhancements were to some extent irreproducible and efforts to mitigate this situation are ongoing.

To investigate the conformality of the OLED structure and further assess the enhancement of light extraction, the green PhOLED, fabricated on the optimized patterned PC, was imaged by the Focused Ion Beam (FIB) technique. The image indicated a mostly conformal 'corrugated' OLED structure as shown in Figure 2.4; the corrugation height, however, reduced to ~170 nm.

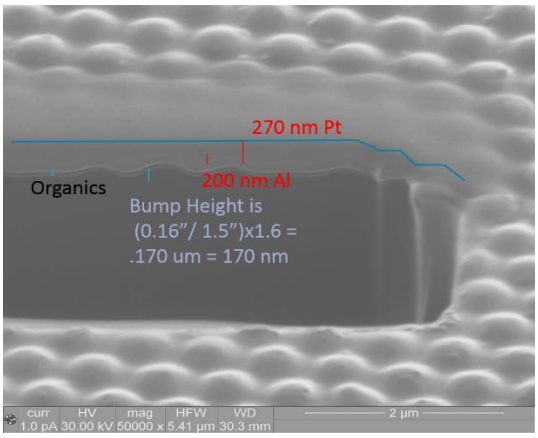

Figure 2.4: FIB image of a green PhOLEDs fabricated on patterned PC (h ~320 nm) The image clearly shows that the OLED structure is corrugated as evident from the top of the structure even after deposition of 270 nm of Pt.

To analyze what determines the efficiency enhancement, AFM images were taken before and after the device fabrication. These enhancements, due to outcoupling of light trapped in the high refraction index organics and possibly reduced plasmon-related losses,

www.manaraa.com

were found to strictly depend on the height of the corrugated OLED structure and its uniformity. Figure 2.5 shows AFM images of complete devices on various patterned substrates and compares the output of these corrugated OLEDs with that of flat OLEDs. Three different substrates were used for this analysis. Table 2.2 summarizes the dependence of the OLEDs' light extraction enhancement on the corrugation height. Light extraction increased with the corrugation height of the OLED up to a certain limit. That is, the optimal substrate feature height of $h \sim 320$ nm was likely limited by the optimal pattern height to pitch ratio needed for conformal organic layers deposition. If the organic layers are not conformal, tall features will introduce high electric fields at certain points and cause leakage current and even shorts, which obviously degrade the devices.

Table 2.2: Corrugation height of the pattern before and after device fabrication and the associated enhancement factor

Sample	Corrugation height before device fabrication		Enhancement factor
	Before device fabrication	After device fabrication	
14-0801-4 standard	320	145	~1.58x
14-0801-5a inverse	135	118	~1.45x
14-0801-4 standard	320	190	~2.98x

2.3.2. Evaluation and proposed solution

Although the FIB images show a corrugated and most likely conformal OLED on patterned PC, the difference in the height of the nano-pattern before and after device fabrication indicates that the OLED layers are not entirely conformal. AFM measurements show that the non-conformal stack is due mainly to the solution processed polymer anode. Though adding a fluorosurfactant to the PEDOT:PSS solution provides better wetting of

www.manaraa.com

the polymer on plastic substrates, it is not sufficient for conformal coating and hence requires a systematic study for improving the conformal fabrication by controlling the solution processing parameters. We therefore studied the effect of solution processing parameters and anode film thickness on the conformal coating of this conductive polymer on patterned PC-substrates.

Earlier measurements with a PEDOT:PSS anode fabricated by spin coating at 3000 rpm for 30s on the patterned substrates exhibited a higher current density than similar devices on flat PC. The higher current density is not necessarily related to a higher device efficiency as might be expected, and, as mentioned, the device performance was not always reproducible. To address this issue, we mapped the current distribution on the patterned PEDOT:PSS anode via conductive AFM (c-AFM). The results indicated a non-uniform current distribution with, as expected, a higher current through the troughs and a significantly lower current at the peaks of the nano-patterns. Interestingly, the current difference increases with increasing voltage. Figure 2.5a and 2.5b show the c-AFM images of a PEDOT:PSS coated patterned PC (h ~320 nm) under 0.5 V and 1.0 V bias, respectively. ΔI = 0.13 μA between the troughs and the peaks of the pattern with the maximum current through the troughs (I_{MAX}) 0.25 μA. Under 1 V bias, ΔI increased to 0.27 μA with I_{MAX} = 0.3 μA. This is consistent with the faster roll off for devices fabricated on patterns as compared to the devices on flat PC (Figure 2.3c). In contrast, a larger area of a PC with shallower features (135 nm) provides a more uniform current. This result is in agreement with the similar current density profile observed for both flat and 135 nm corrugated PCs as seen in Figure 2.3a. Studies claim [25] that the PEDOT:PSS film generally consists of small conductive PEDOT regions surrounded by less conductive PSS-

www.manaraa.com

rich regions where PEDOT is p-doped and thus oxidized. In the case of multiple layers of the polymer, alignment of these conductive and insulating regions might play a crucial role in achieving uniform conductivity over the pattern. However, excess oxidation can cause degradation of the polymer which can lead to less conductive regions at high driving current. [28-29]

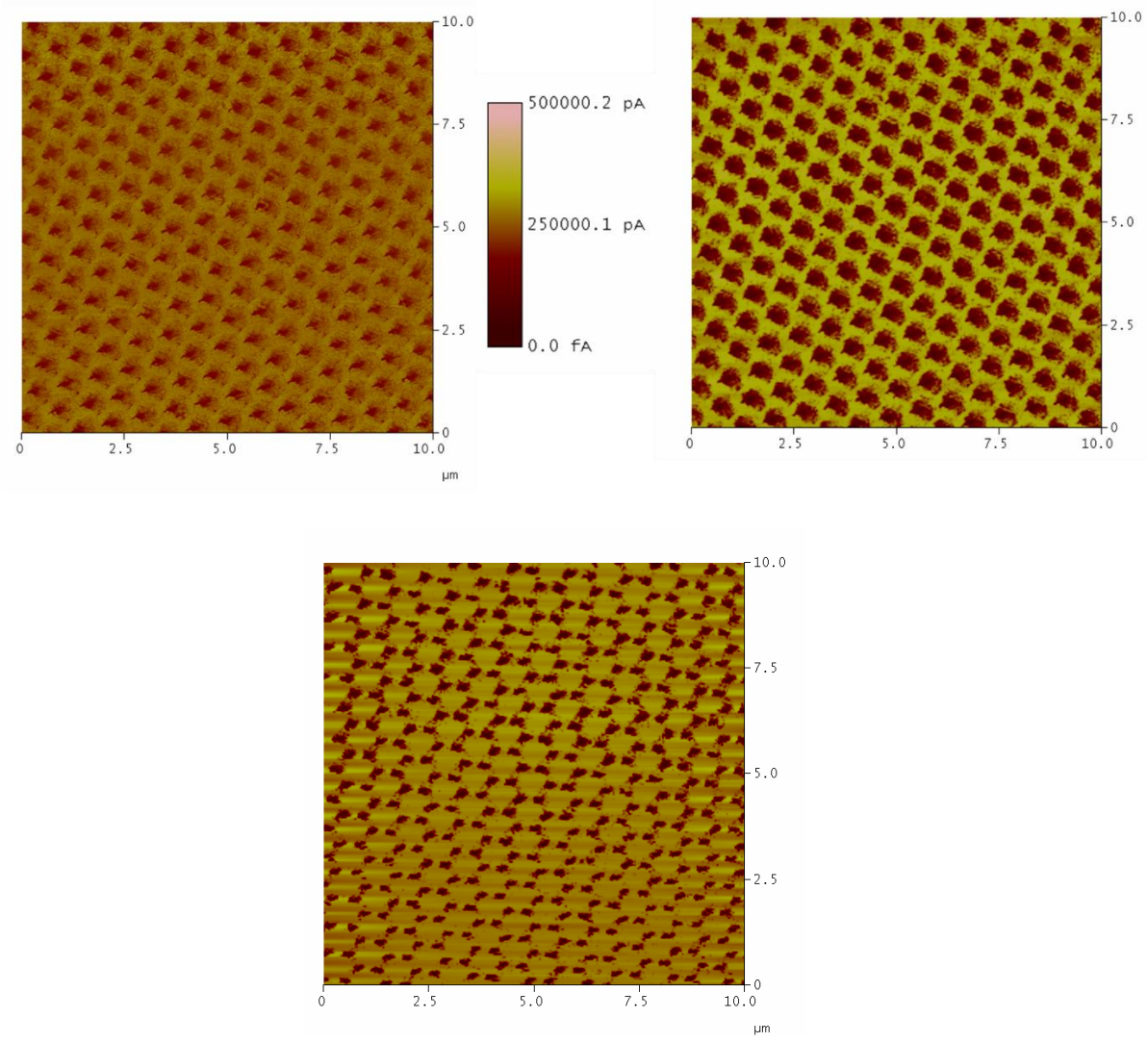

Figure 2.5: c-AFM images of PEDOT:PSS spin-coated at 3000 rpm for 30 s on (a) patterned PC with h ~320 nm under 0.5 V bias (b) patterned PC with h ~320 nm under 1.0 V bias and (c) patterned PC with h~ 135 nm under 0.5 V bias.

www.manaraa.com

To optimize the polymeric anode on patterned PC substrates for achieving a uniform current throughout the device, PEDOT:PSS was spin-coated at varying spin speeds and durations. The pattern heights were measured by tapping mode AFM before and after the PEDOT:PSS spin-coating; the results are summarized in Table 2.3. As seen, a more conformal film was achieved with higher speed processing that results in a thinner polymer layer. The c-AFM image (**Figure 2.6**) also shows that a larger area of the patterned substrate/anode displays uniform current.

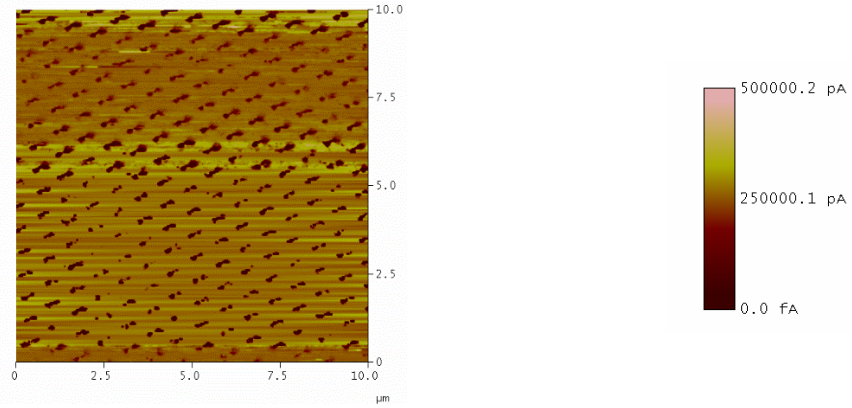

***Figure 2.6**: c- AFM images of PEDOT:PSS spin-coated @ 6000 rpm for 30s on standard pattern (h ~320 nm) under 1.0 V bias*

2.3.3. Metal mesh/PEDOT:PSS anode

Though a faster spin coating rate of PEDOT:PSS generates a conformal thinner film with a more uniform conductivity, the overall sheet resistance increases from 170 Ω/□ to 290 Ω/□. **Figure 2.7** compare the sheet resistance of several multilayer PEDOT:PSS anodes on patterned substrates spin coated at different speed. This higher sheet resistance, in turn, can reduce the peak brightness and increase the resistive loss.

www.manaraa.com

Table 2.3: Pattern heights before and after PEDOT:PSS spin coating

Substrate (initial height)	PEDOT:PSS* solution +additive	Spin coating speed and duration	UV ozone treatment before 2nd layer	Height (nm)
15-1-13-7A All substrates are UV ozone treated (10mins) before PEDOT:PSS spin coat (330 nm)	6% EG+ 1% Capstone FS35 fluorosurfactant	1000 rpm for 30s	No	60
		3000 rpm for 30s	No	141 - 149
		3000 rpm for 30s	Yes	87 - 94
		6000 rpm for 30s	No	194-203
		6000 rpm for 60s	No	208-218
		6000 rpm for 120s	No	219-237
15-1-13-8A (270 nm)		6000 rpm for 120s	No	166-173
		6000 rpm for 120s 3 layers	No	102-112

*2 PEDOT:PSS layers unless mentioned otherwise

www.manaraa.com

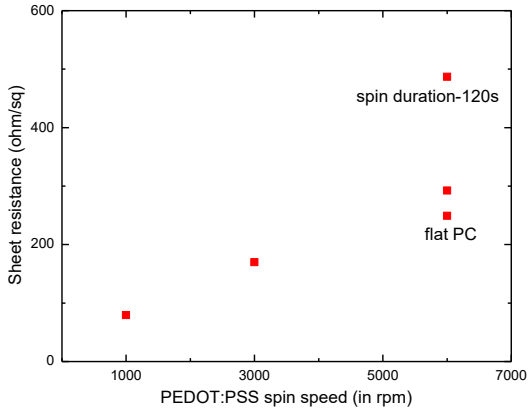

Figure 2.7: Sheet resistance of PEDOT:PSS coated on patterned substrates (h ~ 320nm) at different spin coating rates and duration. (The spin duration is 30s if not mentioned otherwise)

To compensate for the conductivity loss in thinner PEDOT:PSS layers, we tested an anode of a very thin single layer PEDOT:PSS combined with a semi-transparent metallic mesh. The latter was a grid of 30 nm thick semi-transparent Al features deposited on PET substrates provided by MicroContinuum, Inc. The metal grids consisted of hexagonal patches as shown in **Figure 2.8.** The metal mesh design was evaluated for 3 hexagon sizes (125 µm, 250 µm, and 500 µm) with a constant wire width of 20 µm. To employ the mesh structure as anode, these were spin-coated with PEDOT:PSS and OLEDs were built on the hybrid anode structure.

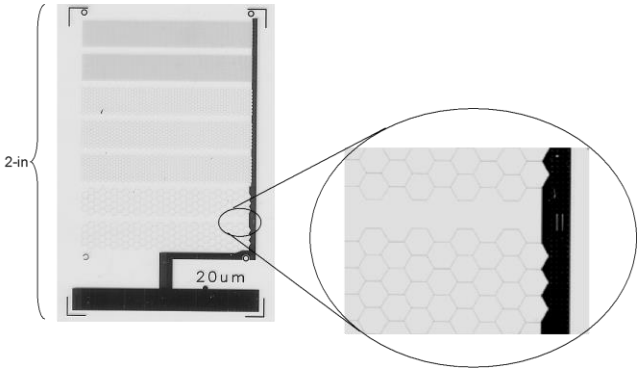

Figure 2.8: Al mesh deposited on PET substrate with three different hexagon sizes and the enlarged segments shows the hexagon pattern with 500 µm side

www.manaraa.com

Our preliminary results showed that the metal grids provide excellent hole injection, increasing the power efficiency of the OLEDs with no significant transparency loss due to the grid-like structure. In **Figure 2.9**, we compare the performance of devices on flat PET substrates with different grid structures. Blue PhOLEDs were fabricated on the flat PET substrates with just one layer of PEDOT:PSS and the OLEDs' performance on the different grids was analyzed by referencing to that of an OLED on a flat PET with no metal-grid. The results show that the metal-grid serves well in the combined anode, and it can be used with patterned PC substrate to further enhance light extraction from OLEDs.

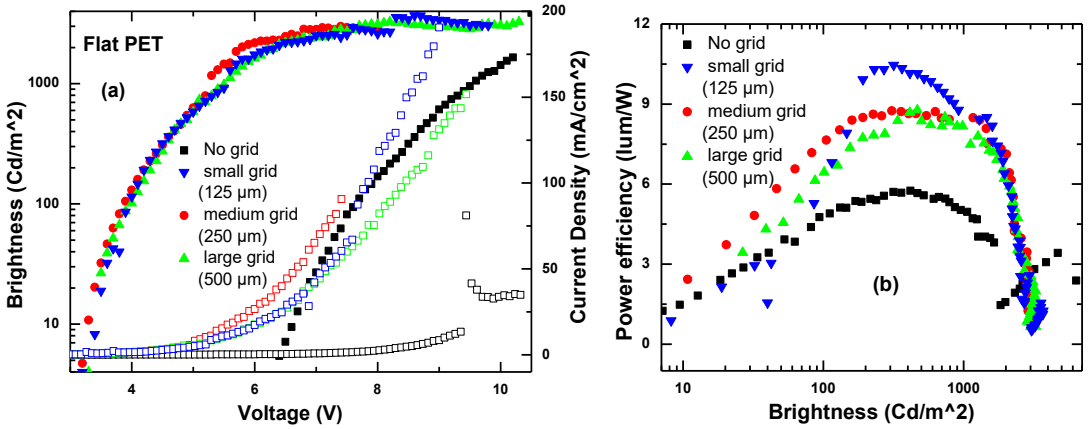

Figure 2.9: Effect of using a hybrid metal grid with a very thin PEDOT:PSS anode. (a) J-L-V (solid and open symbols represent brightness and current density respectively (b) Power efficiency comparison for different metal grids

2.4. Summary:

Outcoupling enhancements using various nano-corrugated PC substrates for green-, blue-, and white-emitting OLEDs were analyzed. The OLEDs' anode was a thin PEDOT:PSS layer whose thickness was optimized to achieve a conformal OLED stack and a uniform current distribution. Significant enhancements of 1.5 to ~3 folds were achieved with the enhancement strictly depending on the height of the corrugation and the related

www.manaraa.com

anode thickness. The PEDOT:PSS spin coating process was optimized to form a conformal anode on the patterned PC. Reproducibility of the enhancement remains an issue and approaches, such as the use of a very thin PEDOT:PSS on top of a transparent thin metal mesh, to address this issue are presented.

2.5. Experimental Procedure:

2.5.1. Materials

The flat and patterned PC substrates with various pattern heights were provided by MicroContinuum, Inc. The conductive polymer PEDOT:PSS was purchased from H. C. Starck and used as the anode. MoO_3, was purchased from Sterm Chemicals, TAPC, CBP, 3TPYMB, TmPyPB, $Ir(ppy)_3$ were purchased from Luminescence Technology Corporation. BPhen and FIrpic were purchased from Sigma-Aldrich.

2.5.2. PEDOT:PSS film fabrication and characterization

The PEDOT:PSS anode was spin coated on 10 min UV-ozone treated PC substrates. The PEDOT:PSS solution was mixed with 6 v% EG and 1 v% Capstone FS35 fluorosurfactant. The mixed solution was filtered using a 0.45 μm syringe filter. The solution was spun at various spin rates and spin durations. For example, a single layer of PEDOT:PSS was deposited by spin coating the mixed solution at 6000 rpm for 30 s followed by annealing the film on a hot plate at 120^{o}C for 5 min. The second PEDOT:PSS layer was formed following the same procedure. The resulting film was annealed at 120^{o}C for 1 h in air and for 1 h in the glovebox. Sheet resistances were measured using a four point probe setup with a source measurement unit (Keithley 200 and Fluke 8842A). Transmittance was measured using an Ocean Optics spectrometer (PC2000-ISA) and the

www.manaraa.com

morphology of the films was obtained by AFM (TESPA) employing tapping mode; current distribution maps were imaged by conductive AFM employing contact mode.

2.5.3. OLED fabrication and characterization

OLEDs were fabricated on the PEDOT:PSS-coated PC substrates as well as on ITO/glass substrates for reference. The Al cathode and all organic materials were deposited by thermal evaporation inside a thermal evaporation chamber with a base pressure of $\sim 10^{-6}$ mbar within a glovebox. The Al cathode was deposited through a shadow mask containing either 1.5 mm diameter circular holes or 3 mm wide stripes. Characterization of the OLEDs was done using a Keithley 2400 source meter to apply a voltage and measure the current. The brightness was measured by a Minolta LS110 luminance meter and the EL spectra were obtained using an Ocean Optics PC2000-ISA spectrometer. The raw spectra were obtained in the "SCOPE" mode, but were corrected to the radiometrically calibrated mode; the spectra shown are the corrected spectra.

2.6. References

[1] J. Shinar, V. Savvateev, in Organic Light-Emitting Devices: A Survey, ed. J. Shinar, Springer, New York, 2004, ch.1.

[2] J-S. Kim, P.K.H. Ho, N. C. Greenham, R. H. Friend, *J. Appl. Phys.* **88,** 1073 (2000)

[3] M. A. Baldo, D. F. O'Brien, Y. You, A. Shoustikov, S. Sibley, M. E. Thompson, S. R. Forrest, *Nature* **395**, 151 (1998).

[4] G. Gu, P.E. Burrows, S. Venkatesh, S.R. Forrest, M.E. Thompson, *Opt. Lett.* **22**, 396 (1997).

[5] A. Chutinan, K. Ishihara, T. Asano, M. Fujita, S. Noda, *Org. Electron.* **6**, 3 (2005).

[6] S. Möller, S. R. Forrest, *J. Appl. Phys.* **91**, 3324 (2002).

[7] J.-M. Park, Z. Gan, W. Y. Leung, R. Liu, Z. Ye, K. Constant, J. Shinar, R. Shinar, K.-M. Ho, *Opt. Express*, **19**, A786 (2011).

www.manaraa.com

[8] C.-H. Chang, K.-Y. Chang, Y.-J. Lo, S.-J. Chang, H.-H. Chang, *Org. Electron.* **13,** 1073 (2012).

[9] G. Gaertner, H. Greiner, *Proc. SPIE* 6999, Organic Optoelectronics and Photonics III, 69992T (2008).

[10] F. Nuesch, E. W. Forsythe, Q. T. Le, Y. Gao, L. J. Rothberg, *J. Appl. Phys.* **87**, 7973 (2000).

[11] J. Gasiorowski, R. Menon, K. Hingerl, M. Dachev, N. S. Sariciftci, *Thin Solid Films* **536**, 211 (2013).

[12]M. Cai, Z. Ye, T. Xiao, R. Liu, Y. Chen, R. W. Mayer, R. Biswas, K-M Ho, R. Shinar, J. Shinar, *Adv. Mater.* **24**, 4337 (2012).

[13] M. Cai, T. Xiao, E. Hellerich, Y. Chen, R. Shinar, J. Shinar, *Adv. Mater.* **23**, 3590 (2011).

[14] T. Xiao, W. Cui, J. Anderegg, J. Shinar, R. Shinar, *Org. Electron.* **12**, 257 (2011).

[15] Y. H. Kim, C. Sachse, M. L. Machala, C. May, L. Muller-Meskamp, K. Leo, *Adv. Funct. Mater.* **21**, 1076 (2011).

[16] M. Cai, T. Xiao, R. Liu, Y. Chen, R. Shinar, J. Shinar, *Appl. Phys. Lett.* **99**, 153303 (2011).

[17] K. Fehse, K. Walzer, K. Leo, W. Lovenich, A. Elschner, *Adv. Mater.* **19**, 441 (2007).

[18] S. I. Na, S. S. Kim, J. Jo, D. Y. Kim, *Adv. Mater.* **20**, 4061 (2008).

[19] D. S. Hecht, L. B. Hu, G. Irvin, *Adv. Mater.* **23**, 1482 (2011).

[20] J. Ouyang, Q. F. Xu, C. W. Chu, Y. Yang, G. Li, J. Shinar, *Polymer* **45**, 8443 (2004).

[21] T. Stocker, A. Kohler, R. Moos, *J. Polym. Sci., Part B: Polym. Phys.* **50**, 976 (2012).

[22] J. Shinar, R. Shinar, *J. Phys. D: Appl. Phys.* **41,** 133001 (2008).

[23] E. Hrehorova, M. Rebros, A. Pekarovicova, P.D. Fleming, V.N. Bliznyuk, *TAGA Journal* **4**, 219 (2008).

[24] M. Vosgueritchian, D. J. Lipomi, Z. Bao, *Adv. Funct. Mater.* **22**, 421 (2012).

[25] C. M. Palumbiny, J. Schlipf, A. Hexemer, C. Wang, P. Müller-Buschbaum, *Adv. Electron. Mater.* **2**, 1500377 (2016).

[26] N. Chopra, J. Lee, J. Xue, F. So, *IEEE Trans. Electron. Devices,* **57,** 101 (2010).

[27] H. Sasabe, J. Kido, *J. Mater. Chem. C* **1**, 1699 (2013).

www.manaraa.com

[28] M. Lapkowski, A. Prón, *Synth. Met.* **110,** 79 (2000).

[29] S.K.M. Jönsson, J. Birgerson, X. Crispin, G. Greczynski, W. Osikowicz, A.W. Denier van der Gon, W.R. Salaneck, M. Fahlman, *Synth. Met.* **139**, 1 (2003).

www.manaraa.com

CHAPTER 3

HIGH EFFICIENCY FLUORESCENT WHITE OLED ON PATTERNED PLASTIC SUBSTRATES

Abstract

In the previous chapter we reported that patterned polycarbonate (PC) substrates significantly enhance light outcoupling from green and blue OLEDs fabricated by thermal vacuum evaporation. In this chapter we continued to work on simple and potentially cost effective approaches to enhance light extraction from fluorescent white OLEDs (WOLEDs) using simple structures and inexpensive materials to achieve efficient WOLEDs. To minimize the waveguided loss at the anode+organic/glass and air/glass substrate interfaces, we used the flexible dome-shaped nanopatterned PC substrates with refractive index (n = 1.58) higher than glass (n ~1.5). Substrates with pattern height of 320 nm were used for this project based on the optimized results described in the previous chapter. The OLEDs were fabricated on the patterns after optimizing the WOLEDs on standard glass/ITO substrates. We report 1.5 – 2 fold enhancement over flat PC due to the pattern. The color stability of the WOLED and the stability of the structure (with ITO anode) in general are addressed in the chapter as well.

Keywords: OLEDs, white OLEDs, SSL, angular EL profile, plastic substrates, outcoupling

3.1. Introduction

There is continued interest toward developing red-green-blue (RGB) OLEDs in the display industry for consumer electronics. OLEDs are perfectly suitable for large area lighting as well as they are potentially low cost, compatible with flexible substrates, and

www.manaraa.com

provide warm and diffused light. Several companies, as well as the U.S. Department of Energy are putting great effort to improve OLEDs for solid state lighting (SSL) applications. However, for such applications, there are many challenges that need to be resolved for integrating these devices in commercial products. One such major challenge is light outcoupling that was addressed in Chapter 2. For general lighting purposes, some restrictions regarding color temperature of the light source have to be followed in order to achieve comparable emission spectra as sunlight or standard tungsten light. That is why color balance of white OLEDs for SSL application is important. The first WOLED was reported by Kido et al. in 1994 by doping a blue fluorescent host with an orange emitting dopant. [1] Since then different types of WOLED structures have been extensively studied for improving device efficiency, stability, and color balance,[2-5] while achieving color stability with increasing voltage[6-7] and viewing angle[8] still remain tricky. White emission can be achieved by either mixing the three primary colors red, green, and blue in appropriate proportions, or by mixing complementary colors like blue and orange (BO). WOLED structures typically include a guest-host emissive layer where a guest with a smaller HOMO-LUMO gap is doped into a host molecule with a higher gap. In these systems, the guest and host materials are chosen so that the absorption spectrum of the guest partially or fully overlaps the emission spectrum of the host. The excitons accumulated at the host are transferred non-radiatively to the guest molecules and the dopant emission is observed.[9] For example, RGB WOLEDs use red and green phosphorescent emitters doped in a blue fluorescent host to achieve white emission. While RGB architecture has been the most popular design for WOLEDs, this multilayer emissive architecture tends to be more complicated than the BO architecture. These device structures

www.manaraa.com

also include expensive phosphorescent materials whereas BO devices can be of much simpler structure with entirely fluorescent materials.[9] However, irrespective of the type of the WOLEDs, since multiple emitters are required in an OLED to achieve white emission, device architecture becomes very crucial to attain the desired color coordinates and proper charge balance. In this chapter, we demonstrate a highly efficient WOLED with inexpensive fluorescent materials. We utilized blue emission from either 4,4'-bis(2,2'-diphenylvinyl)-1,1'-biphenyl (DPBVi) or 9,10-di(naphth-2-yl)anthracene (ADN) and orange emission from 5,6,11,12-tetraphenylnaphthacene (rubrene). We optimized the structure to address the issue of device stability and achieve the desired color coordinates. Furthermore, OLEDs suffer from blue shift in the electroluminescent (EL) profile with increasing viewing angle. Having a broader EL emission, the blue shift with viewing angle becomes a significant problem. We showed that with the use of a microlens array on the back of the glass substrate, the variation in the angular emission profile can be suppressed. Eventually, optimized WOLEDs were fabricated on the patterned polycarbonate substrates, enhancing the light extraction from the device as described next.

3.2. Results and Discussion

3.2.1. White emission

We used a typical fluorescent guest-host system where rubrene with a relatively low 2.2 eV energy gap is doped into the higher HOMO–LUMO gap DPBVi (*Eg* = 3.1 eV) or ADN (*Eg* = 3.1 eV). Fluorescent blue DPBVi was previously shown to yield, together with rubrene, very intense WOLEDs.[10] We focused on the structures ITO/MoO_3 (5 nm)/NPB (50 nm)/1wt % rubrene doped DPVBi (*x* nm, *x* = 10, 20, 30 nm)/Alq_3 (50 nm)/LiF (1 nm)/Al (100 nm). **Figure 3.1** shows the spectra of these devices for different *x* (left) as

www.manaraa.com

well as the spectra of the device with x = 10 nm at different voltages (right). As a higher energy excitation is required for the emission from molecules with large HOMO-LUMO gap, the relative intensity of the blue peak at 440 nm increases with increasing driving voltage. Similarly, a stronger contribution from the blue host was observed with decreasing thickness of the rubrene-doped layer. These devices produce a warm white color with CIE coordinates essentially unchanged (varying from (0.37, 0.40) to (0.41, 0.44)) when x increases from 10 to 30 nm.

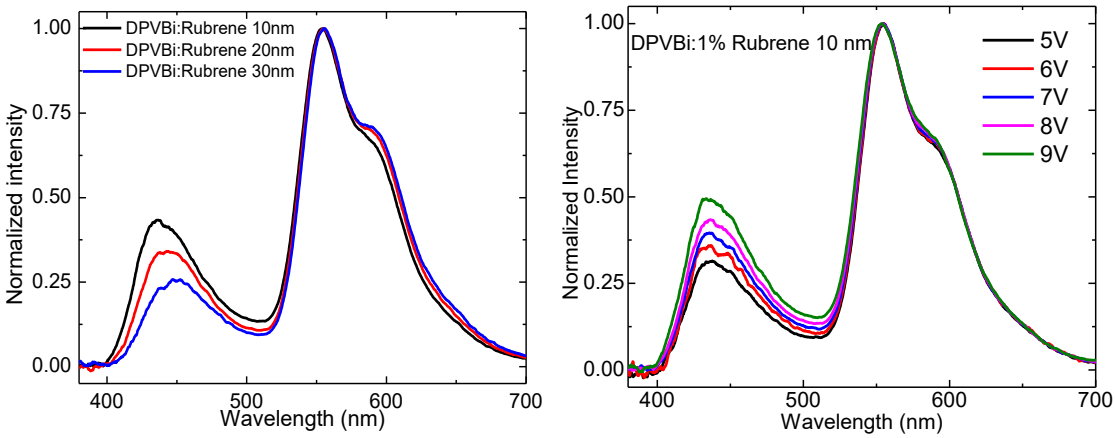

Figure 3.1: EL spectra of WOLEDs with the structure ITO/MoO_3 (5 nm)/NPB (50 nm)/1wt % rubrene: DPVBi (x nm, x = 10, 20, 30)/Alq_3 (50 nm)/LiF (1nm)/Al (100 nm) for different x (left) and at different voltages for x = 10 nm.

DPVBi was later substituted with ADN as the latter yields similarly efficient, highly stable, and robust devices. **Figure 3.2** shows the energy band diagram of the devices with ADN and rubrene as emissive layers and the molecular structures of the fluorescent materials. As shown, the physical structure is ITO/MoO_3/*N,N*′-di(1-naphthyl)-*N,N*′-diphenyl-(1,1′-biphenyl)-4,4′-diamine (NPB) / ADN:1%rubrene/ADN/tris-(8-hydroxyquinoline) Al **(**Alq_3)/LiF/Al.[11]

www.manaraa.com

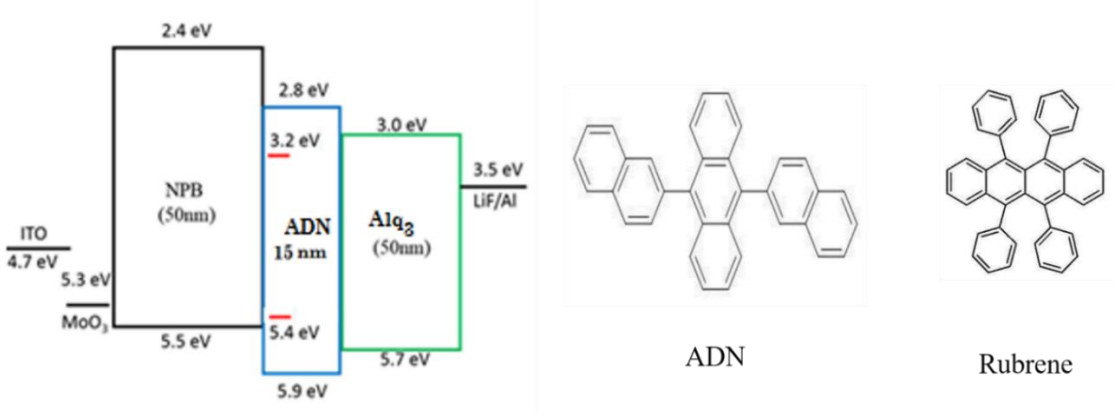

Figure 3.2: Left: The energy band diagram of the fabricated WOLEDs. Right: The molecular structure of the blue ADN and the orange rubrene fluorescent materials.

To improve the color rendering index (CRI), we explored stacked layers of blue-orange-blue emitting materials by introducing a very thin layer of ADN at the interface of NPB and the rubrene-doped layer. The modified structure is ITO/MoO_3 (5 nm)/NPB (50 nm)/ADN (4 nm)/1wt % rubrene doped ADN (2 nm)/ADN (*x* nm, *x*= 15 nm, 40 nm)/Alq_3 (50 nm)/LiF (1 nm)/Al (100 nm). This geometry certainly enhances the blue emission from the OLED by efficiently generating excitons in the ADN layer and thus producing color coordinates closer to perfect white. The color coordinates change from (0.43,0.46) to (0.32,0.34) as the emission layer structure changes from yellow-blue to blue-yellow-blue. **Figure 3.3** compares the spectra from blue-yellow-blue and yellow-blue devices.

3.2.2. Color stability and angular profile

A major challenge with WOLEDs in solid state lighting is the color stability. The color variation has to be minimal with changing angle and voltage. The blue-yellow-blue structure is efficient for confining excitons within the emissive layer, reducing the change in the blue contribution with increasing driving voltage. This structure thus yields a color that is stable with increasing voltage as shown in **Figure 3.4**a that compares the EL spectra at different voltages of such a blue-yellow-blue device on a PC substrate. We also achieved

www.manaraa.com

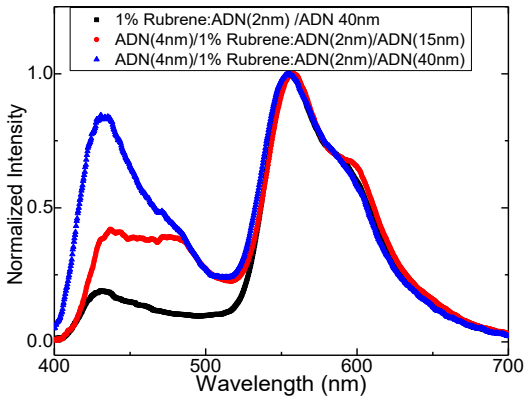

Figure 3.3: Comparison of the EL spectra of WOLEDs with blue-yellow-blue and blue-yellow geometries.

very stable devices with this geometry by mixing the interfaces of the organic layers instead of fabricating abrupt interfaces. With an abrupt junction, the device stability was poor. For example, the color coordinates shifted from (0.32,0.34) to (0.37,0.48) (white turned into greenish yellow) after running the same pixel at high driving voltage (9 V, ~14,000 Cd/m^2), as shown in the figure. The mixing of the NPB/ADN and ADN/Alq_3 at the interfaces yields a more stable device. The emission spectra of the mixed-interface devices are shown for a fresh pixel and for the same pixel after 5 consecutive runs at high driving voltage (9V, ~ 10,000 Cd/m^2). The shift in the color coordinate was from (0.31,0.37) to (0.32,0.38). The graded junction presumably reduces the accumulation of interfacial charges,[12] thus diminishing the alteration of the electric field at a high driving bias as well as the quenching effect due to the accumulated charges at the electrode, producing a more stable and efficient device.

The normalized angular profiles of the EL spectra are shown in **Figure 3.5** for WOLEDs both with (right) and without (left) a microlens array (MLA) attached on the back of the glass substrate. The structure of the OLED is as mentioned earlier (mixed

www.manaraa.com

interface). As seen in the figures, the spectral or color variation in the WOLED without the MLA is more

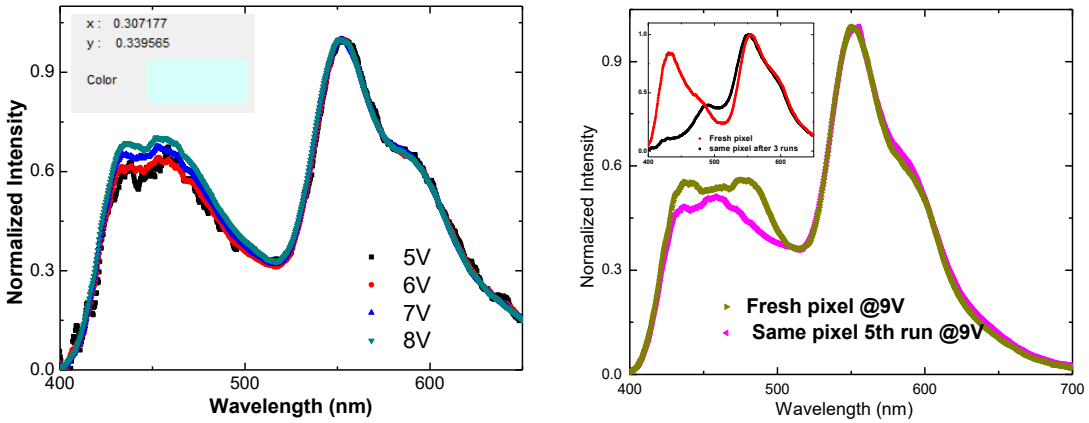

Figure 3.4: (a) Comparison of EL spectra with increasing voltage for devices with the structure PEDOT:PSS (2 layers) anode on PC/MoO_3(5nm)/NPB(45nm)/ADN(4 nm)/1% rubrene:ADN (1 nm)/ADN (15 nm)/Alq_3 (50 nm)/LiF/Al. (b) EL spectra comparison of the 1st and 5th run under high driving voltage (9V, ~ 14,000 Cd/m^2) for a device with graded NPB/ADN and ADN/Alq_3 interfaces, the inset shows the EL spectra of 1st and 3rd run under the same conditions (9V, ~ 10,000 Cd/m^2) for a device with non-graded interfaces.

prominent than for the OLED with the MLA. This is clearly due to the scattering of the outcoupled light by the MLA.[13] The CIE color coordinates for the OLED with the MLA changes from (0.28, 0.35) for normal direction emission to (0.28, 0.34) for an angle of 80°.

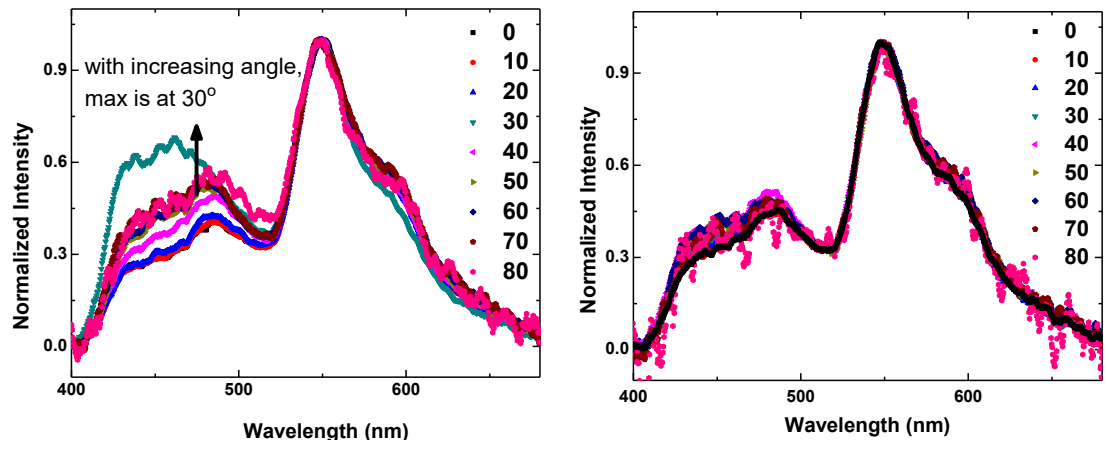

Figure 3.5: Angular EL profile of WOLEDs on ITO without (left) and with (right) MLA from 0 to 80 degrees

www.manaraa.com

3.2.3. WOLED panel

The closest to white CIE color coordinates were obtained for a 1"x1" WOLED panel with the blue-yellow-blue design of the structures ITO/MoO_3 (5 nm)/NPB (50 nm)/ADN (*x* nm, *x* = 3, 7.5, 11.5 and 16 nm)/1wt % rubrene doped ADN (1nm)/ADN (19-*x* nm)/Alq_3 (50 nm)/LiF (1 nm)/Al (100 nm) (**Figure 3.6a**). The thickness of the blue emissive layers (ADN) varied from 3 nm to 16 nm (devices A to D) at the NPB interface while the total thickness of the emissive layer was kept constant. The thickness of the 1% rubrene doped ADN layer was 1 nm. This particular structure allows for more excitons recombination in the ADN layer, enhancing the blue emission and improving the color rendering index. The CIE color coordinates shifts from (0.32, 0.43) to (0.30, 0.40) with increasing *x*. The optimum thickness of the structure was found to be as *x* = 11.5 nm. **Figure 3.6b** shows the EL spectra of these devices showing how the blue emission enhances with increasing ADN layer thickness at the NPB interface. As we have seen earlier, the blue contribution in the EL spectra increases with increasing angle. **Figure 3.6c** shows the EL spectrum of device C (*x*=11.5 nm) at an angle of 45 degrees, which produces color with (0.30, 0.38) coordinates.

3.2.4. WOLEDs fabricated on patterned PC substrates

Thin film encapsulation for PC substrates: Flexible substrates such as PC used in this project have many advantages over standard glass or silicon substrates. They are light weight, cost effective, and have higher refractive index. They can play a crucial role in advancing OLED based solid state lighting technology. But being porous in nature, PC is not an adequate barrier for oxygen and water vapor. As a result, WOLEDs with standard top encapsulation degrade comparatively fast.

www.manaraa.com

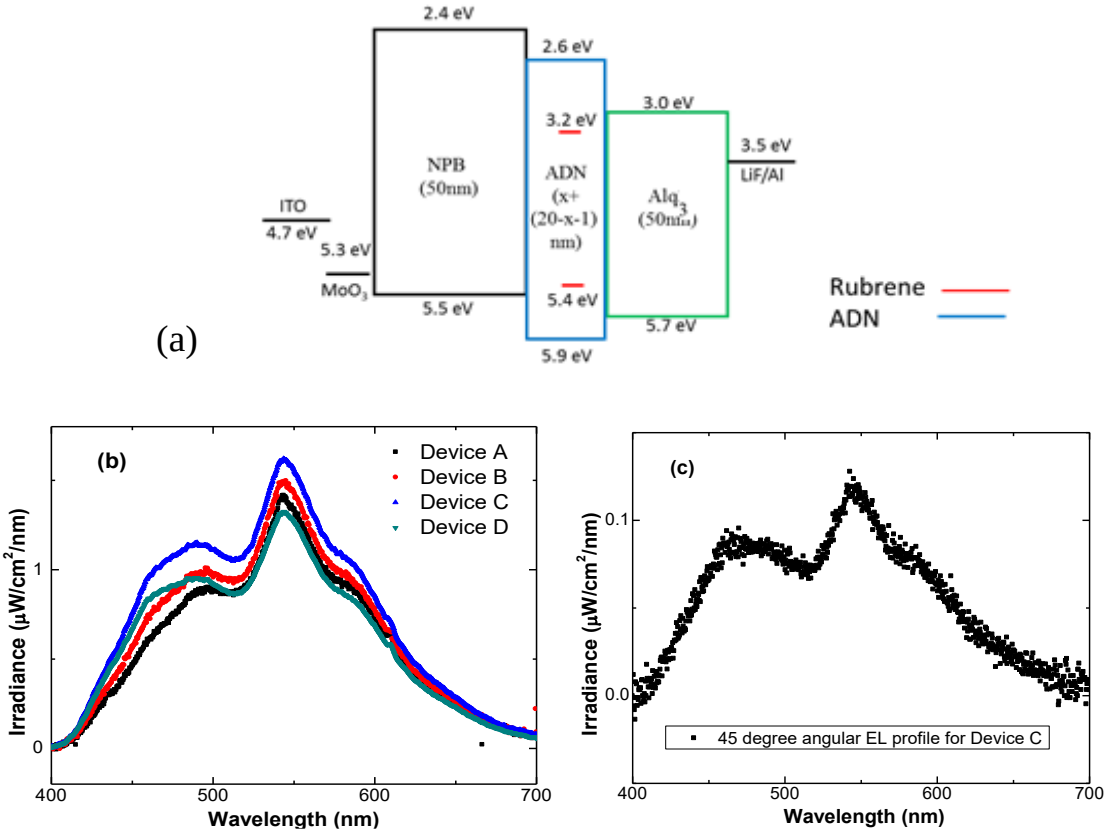

Figure 3.6: (a) *Schematic of WOLED structure. x= 3, 7.5, 11.5, 16 nm for device A to D, respectively. The thickness of the 1% rubrene-doped layer = 1 nm (b)* EL spectra for *devices A to D (c) EL spectra of device C (x = 11.5 nm) at 45 degree angle. As seen earlier, the blue contribution increases with increasing angle for these devices as well.*

To prevent this degradation and to improve it for lighting technology, we used an inorganic/organic multilayer thin film encapsulation technique that is inexpensive. Four periods of LiF (40 nm)/*N*,*N*′-bis(3-methylphenyl)-*N*,*N*′-diphenylbenzidine **(**TPD) (30 nm) layers were deposited on the back of the PC substrates. TPD was chosen because of its high stability, high energy gap, and lower optical absorption in the visible range. **Figure 3.7** compares the optical transmittance of flat PC with and without thin film encapsulation.

www.manaraa.com

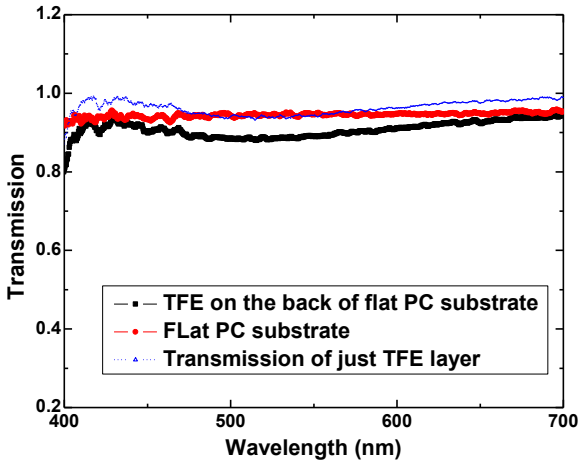

Figure 3.7: Comparison of transmission of the flat PC substrates with and without thin film encapsulation (TFE). The blue dotted line represents the calculated reference transmission of just the TFE layer obtained by deducting the transmission of the substrate.

WOLEDs with a PEDOT:PSS anode: The transparent anode plays a crucial role in the properties of OLEDs that display a broad emission spectrum. As optical transparency may vary with wavelength, a better index matching and uniform optical transmission over the entire visible range result in a better WOLEDs' CRI. The transmission spectra of double layer spin-coated PEDOT:PSS[14] and sputtered ITO anodes on patterned substrates are shown in **Figure 3.8a**. It should be noted that the transmission measurements are done in the normal direction, thus the transmission in the forward hemisphere might differ with viewing angle due to scattering from the pattern. **Figure 3.8b** shows the EL spectra of WOLEDs with a similar structure with ITO or a double layered PEDOT:PSS anode. As seen the contribution of the blue peak (~425 nm) and the red shoulder (~580 nm) are stronger with the PEDOT:PSS anode, which improves the WOLEDs' CRI.

www.manaraa.com

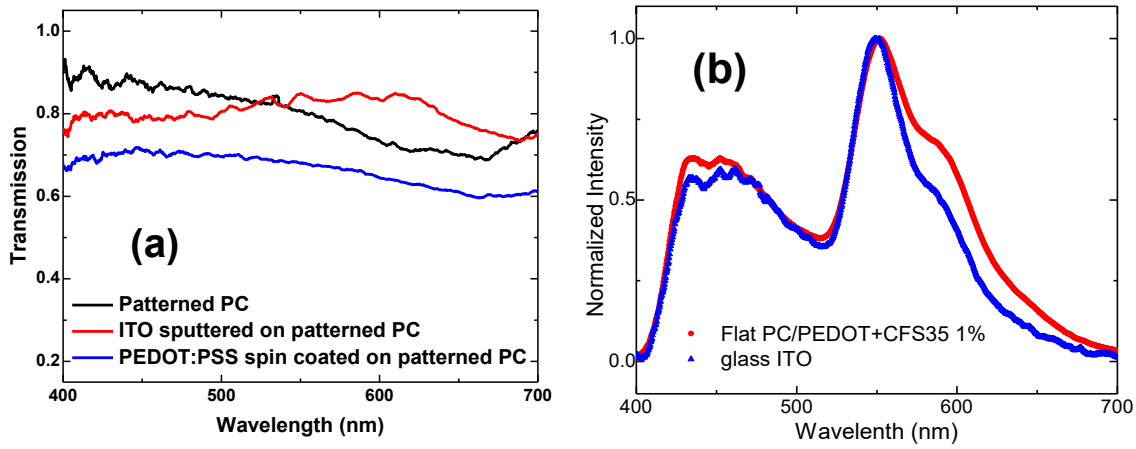

Figure 3.8: (a) Comparison of transmittance of PEDOT:PSS and ITO anodes on patterned PC substrates (b) EL spectra of WOLEDs with PEDOT:PSS or ITO anode on different substrates.

3.2.5. Light extraction from WOLEDs on patterned PC substrates

Similar WOLEDs with the device structure described earlier were fabricated on patterned PC substrates of various feature heights and on a flat PC substrate as a reference. **Figure 3.9** compares the performance of these devices. In chapter 2, we demonstrated that in comparison to devices on flat PC, the OLED brightness at the same current density increased with increasing pattern height. Here we fabricated three sets of devices on patterned and flat PCs using three different recipes for the PEDOT:PSS anode. Two double layered PEDOT:PSS anodes were deposited by spinning the solution at 3000 rpm and at 6000 rpm for 30 sec each. The third anode type was composed of 3 layers of PEDOT:PSS spun at 6000 rpm for 120 s in order to compensate for the conductivity reduction due to a higher processing speed. The sheet resistance's incremental increase with layer thickness was discussed in the previous chapter. While for the anode with the 3000 rpm processing speed there was no significant difference noticed between flat and patterned OLEDs, the other two WOLEDs (6000 rpm processing speed) fabricated on corrugated PCs exhibited higher light outcoupling over flat PCs. Although the reason for this particular result is not

www.manaraa.com

clear, the results are in accordance with the findings presented in the preceding chapter. As PEDOT:PSS anodes spin coated at 3000 rpm are not fully conformal on the corrugated substrate they yield a non-uniform current distribution within the active area. This non-uniform distribution of charge carriers introduces charge imbalance in the device that in turn reduces the efficiency. In contrast, 6000 rpm processing results in a much more conformal structure on the corrugation as shown in Chapter 2. Consequently, it enables corrugated OLEDs to benefit from light scattering by the nano-pattern and thus exhibit higher light outcoupling. The highest luminous efficiency of 5.22 Cd/A was achieved for corrugated WOLEDs with 3 layers of PEDOT:PSS spun at 6000 rpm, which is 1.28 fold higher than that of the reference WOLEDs on flat PC. On the other hand, corrugated WOLEDs with 2 layered PEDOT:PSS spun at 6000 rpm exhibited a luminous efficiency of 3.6 Cd/A, which was 2.6 fold higher than the corresponding WOLED fabricated on flat PC. The enhancement in EQE for this corrugated WOLED was 2.2 fold over that of a flat PC. Table 1 summarizes the performance of WOLEDs on different PC substrates and on different PEDOT:PSS anodes. We suspect that the lower efficiency for WOLEDs with 2 layered PEDOT:PSS anode was due to its higher sheet resistance. The change in the outcoupling factor with this type of PEDOT:PSS anode was most likely related to the effective corrugation height after the spin coating process. Tapping mode AFM images show that the pattern height reduces from 320 nm to 100-110 nm for 3 layers of PEDOT:PSS while it only reduces to 200 nm for 2 layers of PEDOT:PSS.

www.manaraa.com

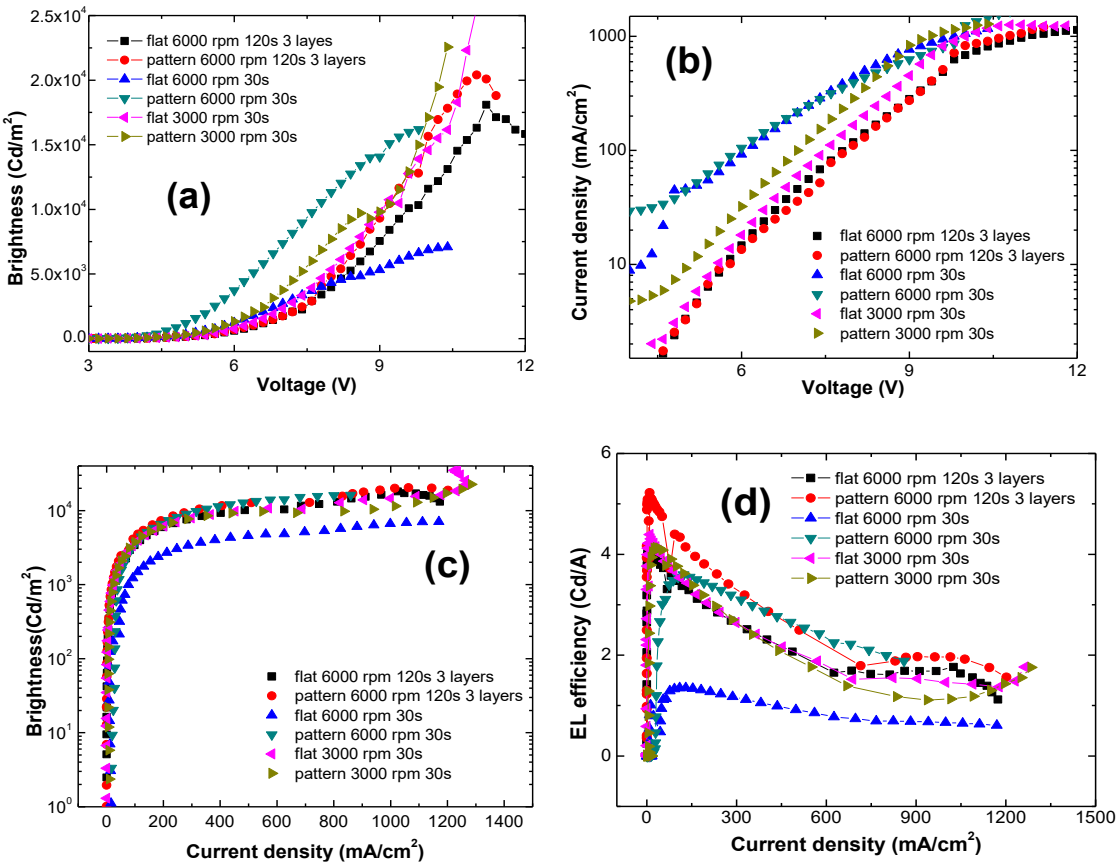

***Figure 3.9**: WOLEDs on flat and patterned PC substrates (h ~270nm) (a) Brightness (L)-V, (b) Current density (J)-V (c) L-J and (d) EL efficiency-J graphs*

Table 3.1: Device performance on different PC substrates and PEDOT:PSS anodes

Sample PC	PEDOT:PSS Processing condition	Corrugation height after spin-coat (nm)	Turn on voltage (V)	Max. luminous efficiency (Cd/A)	Corres-ponding EL (Cd/m^2)	Luminous Efficiency @ 1000 Cd/m^2
Flat	3000 rpm 30 s (2 layers)	0	3.2	4.39	453	4.2
Pattern		~140	3.1	4.13	1328	4.12
Flat	6000 rpm 30 s (2 layers)	0	3.0	1.35	1764	1.29
Pattern		~195	2.9	3.59	4431	2.7
Flat	6000 rpm 120 s (3 layers)	0	3.2	5.22	526	5.1
Pattern		~110	3.1	4.14	463	3.9

www.manaraa.com

3.3. SUMMARY:

In summary, we described efficient and color stable fluorescent WOLEDs fabricated with inexpensive materials. Optimization of the OLED structure was performed to achieve the desired white coordinates in the color space and to mitigate the color stability issue with changing voltage and viewing angle. Outcoupling enhancements using various nano-corrugated PC substrates for these WOLEDs were analyzed. Significant light extraction enhancements of 1.28 to 2.6 fold were achieved for the WOLEDs fabricated on the patterned PC with a corrugation h ~270 nm.

3.4. Experimental Procedure

3.4.1. Materials

The flat and patterned PC substrates with various pattern heights were provided by MicroContinuum, Inc. The conductive polymer PEDOT:PSS was purchased from H. C. Starck and was used as the anode. LiF and the yellow emitter rubrene were purchased from Sigma-Aldrich and TPD from Luminescence Technology Corporation. MoO_3 was purchased from Sterm Chemicals, and NPB and Alq_3 from HW Sands Corporation. The blue host material ADN was provided by Trovato Mfg, Inc.

3.4.2. PEDOT:PSS film fabrication and characterization

All PC substrates were encapsulated from the back with alternating multilayers of LiF/TPD. The substrates were UV-ozone treated for 10 minutes prior to spin coating PEDOT:PSS. The PEDOT:PSS solution was mixed with 6 v% EG and 1 v% Capstone FS35 fluorosurfactant. The mixed solution was filtered using a 0.45 μm syringe filter. The solution was spun at various spin rates and spin durations. For example, a single layer of PEDOT:PSS was deposited by spin coating the mixed solution at 6000 rpm for 30 s followed by annealing the film on a hot plate at 120°C for 5 min. The second PEDOT:PSS

www.manaraa.com

layer was formed following the same procedure. The resulting film was annealed at 120°C for 1 h in air and for 1 h in the glovebox. Sheet resistances were measured using a four point probe setup with a source measurement unit (Keithley 200 and Fluke 8842A). Transmittance was measured using an Ocean Optics spectrometer (PC2000-ISA) and the morphology of the films was obtained by AFM (TESPA) employing tapping mode.

3.4.3. OLED fabrication and characterization

OLEDs were fabricated on the PEDOT:PSS-coated PC substrates as well as on ITO/glass substrates for reference. The Al cathode and all organic materials were deposited by thermal evaporation inside a thermal evaporation chamber with a base pressure of $\sim 10^{-6}$ mbar within a glovebox. The Al cathode was deposited through a shadow mask containing either 1.5 mm diameter circular holes or 3 mm wide stripes. Characterization of the OLEDs was done using a Keithley 2400 source meter to apply a voltage and measure the current. The brightness was measured by a Minolta LS110 luminance meter and the EL spectra were obtained using an Ocean Optics PC2000-ISA spectrometer. The raw spectra were obtained in the "SCOPE" mode, but were corrected to the radiometrically calibrated mode; the spectra shown are the corrected spectra.

3.5. References

[1] J. Kido, K. Hongawa, K. Okuyama, K. Nagei, *Appl. Phys. Lett.* **64**, 815 (1994).

[2] J. Kido, M. Kimura, K. Nagai, *Science* **267**, 1332 (1995).

[3] V. Adamovich, J. Brooks, A. Tamayo, A. M. Alexander, P. I. Djurovich, B.W. D'Andrade, C. Adachi, S. R. Forrest, M. E. Thompson, *New J. Chem.* **26**, 1171 (2002).

[4] S. Reineke, F. Lindner, G. Schwartz, N. Seidler, K. Walzer, B. Lu¨ssem, K. Leo, *Nature* (London) **459**, 234 (2009).

[5] W. Song, M. Meng, Y.H. Kim, C.-B. Moon, C.G Jhun, S.Y. Lee, R. Wood, W.-Y. Kim, *J of Luminescence*, **132**, 2122 (2012).

www.manaraa.com

[6] Kim, C. H., J. Shinar, *Appl. Phys. Lett.* **80**, 2201 (2002).

[7] Y.-S. Park, J.-W. Kang, D.M. Kang, J.-W. Park, Y.-H. Kim, S.-K. Kwon, J.-J. Kim, *Adv. Mater.*, **20**: 1957 (2008).

[8] W. Gaynor, S. Hofmann, M.G. Christoforo, C. Sachse, S. Mehra, A. Salleo, M.D. McGehee, M.C. Gather, B. Lüssem, L. Müller-Meskamp, P. Peumans, K. Leo, *Adv. Mater*. **25**: 4006 (2013).

[9] K. O. Cheon and J. Shinar, *Appl. Phys. Lett.*, Vol. 83, No. 10, 8 (2003).

[10] G. Li, J. Shinar, *Appl. Phys. Lett.* **83**, 5359 (2003).

[11] Y. Guan, and L. Niu, *J. Phys.: Conf. Ser.* ***152****, 012049 (*2009).

[12] H. Riel, S. Barth, T. Beierlein, W. Brutting, S. Karg, P. Muller, W. Riel, *Proceedings of SPIE* Vol. 4105 (2001).

[13] J-M Park, Z. Gan, W. Y. Leung, Z. Ye, K. Constant, J. Shinar, R. Shinar, K-M Ho, *Opt. Exp.* **19**, A786 – A792 (2011).

[14] M. Cai, Z. Ye, T. Xiao, R. Liu, Y. Chen, R. W. Mayer, R. Biswas, K-M Ho, R. Shinar, J. Shinar, *Adv. Mater.* **24**, 4337–4342 (2012).

www.manaraa.com

CHAPTER 4

ORGANIC PHOTODETECTORS IN ANALYTICAL APPLICATIONS

Modified from E. Manna, T. Xiao, J. Shinar, R. Shinar, *Electronics* **4**, 688 (2015)

Abstract

This review focuses on the utilization of organic photodetectors (OPDs) in optical analytical applications, highlighting examples of chemical and biological sensors and lab-on-a-chip spectrometers. The integration of OPDs with other organic optical sensor components, such as organic light emitting diode (OLED) excitation sources and thin organic sensing films, presents a step toward achieving compact, eventually disposable all-organic analytical devices. We discuss recent advances in developing and integrating OPDs for various applications as well as challenges faced in this area.

Keywords: organic photodetectors; organic electronics in analytical applications; integrated sensors; lab-on-a-chip; spectrometer-on-a-chip

4.1. Introduction

There is a growing need for compact, user friendly, inexpensive, field-deployable integrated chemical and biological sensors, including multi-sensor arrays, with a demand for continued miniaturization[1] so that they can be integrated into many systems such as wearable electronics. Such sensors will replace current sensors that are often bulky or costly and require trained personnel for their operation. The sensors are needed for various applications, including water and food quality monitoring, health monitoring, medical testing, and security inspection.[1] They should be reliable, as well as sensitive and selective. Optical sensors are typically very sensitive.[1] Such sensors include an excitation

www.manaraa.com

source, a sensing element, a photodetector (PD), and the electronic circuitry. The sensing element is often an organic thin film with an embedded dye, whose photoluminescence (PL) intensity and decay time are affected by the presence and concentration of an analyte. Thin film technology, in particular organic electronics, is promising to fulfill this need of small size, reliable sensors. However, development and improvement of the various sensor components are still required. Similar to bio/chemical sensors, other on-chip optical devices such as spectrometers are of interest and thin film PDs, organic or hybrid, are promising for advancing such tools.

Organic electronics has already established its significant role in cutting edge technology due to the rapid development of organic light emitting diodes (OLEDs), organic transistors, and more recently organic photodetectors (OPDs). The use of organic thin-film devices is not limited to flat-panel displays and solid-state lighting. Organics plays an important role in analytical and bioelectronics applications. As an example, OLED-based luminescent sensors are sensitive with the ability to be integrated with sensing films, thin film PDs, and microfluidic structures.[2-4] Indeed, OLEDs have been extensively researched as excitation sources for photoluminescence (PL)-based integrated oxygen and pH sensors, integrated oxygen and humidity sensors, glucose and other bioanalyte sensors, various immunoassays, and for on-chip spectrometers.[2-6] Since optical sensors rely on the interaction between the sensing material and light from the excitation source, precise and sensitive detection of a signal originating from the sensing film is key in determining the device performance. Initially, OLEDs were integrated with a sensing film fabricated on the opposite side of a common substrate, but to achieve a sensitive and specific detection a photomultiplier tube (PMT) was commonly used.[7-8] Though optical sensors with a PMT

www.manaraa.com

have a very high signal to noise ratio (SNR) and fast response time,[9,10] the PMT is highly magnetic-field sensitive and bulky, which prevents scaling down sensors with it and the sensor's use is limited to a magnetic-free environment.

The demand for small scale analytical instrumentation in research as well as in industry has led to the development of lab-on-a-chip (LoC) technology. The LoC technology attempts to create small scale analytical devices, which can be achieved via component integration. In optical sensors this entails integration of the excitation source, the sensing element, and the PD on a single, including microfluidic, chip.[4] The rapid growth of LoC usage in laboratory environment requires smaller PDs instead of a PMT to enable on-chip integration. Inorganic PDs have served this purpose well with an additional built-in preamplifier on the chip to enhance the detected signal.[11-12] However, CMOS and other inorganic thin film deposition procedures often require high processing temperatures and as a result are not cost effective for use in disposable devices. OPDs can be a good alternative to their inorganic variant due to their low temperature processing suitability and fabrication on simple substrates such as glass or plastic, which makes them flexible in size and design and hence compatible with microfluidic architectures. Though OPDs are not yet commercially available and are mostly being used in research and development areas, they present a potential for integration with LoC sensing devices because of their adaptable design, ease of fabrication, and unique simplicity of structural integration.[13-15]

This review first discusses common OPD structures and their principle of operation. Next it describes the progress in OPD use in analytical applications via specific examples and presents issues that need to be mitigated to lead to compact and eventually disposable

www.manaraa.com

optical analytical devices. The review concludes with the recent development of hybrid PDs and an outlook.

4.2. Organic Photodetectors: Working Principle

PDs convert incident light to an electrical signal. There are various types of PDs, including PMTs, junction photodiodes, photoconductors/photoresistors, phototransistors, avalanche photodiodes, and charge-coupled devices (CCDs). OPDs are a more recent area of study. Their structure is basically that of an organic solar cell (OSC) though in contrast to OSCs they are often operated at a negative, typically small, bias. This negative bias leads to an internal field greater than the built-in field, which improves the photosensitivity and response speed. The signal increases with increased negative bias, however, the dark current (leakage current) increases as well. Low dark current is necessary for optimal PD performance and lower noise. The dark current can be reduced also by optimizing the morphology of the active layer and using a proper electron- or hole blocking layer. OPDs are comprised of metal electrodes and π-conjugated polymers or organic small-molecules as donors with typically fullerene derivatives as acceptors. The standard structure of an OPD is indium tin oxide (ITO) (anode)/hole transport (extraction) layer (HTL)/π-conjugated polymer-based bulk heterojunction or small molecule-based multiple donor-acceptor layers/electron transport (extraction) layer (ETL)/Ca/Al (cathode). The typical energy gap (1.5 - 3 eV) between the highest occupied molecular orbital (HOMO) and lowest unoccupied molecular orbital (LUMO) of such π-conjugated organic materials can be a good match for absorbing visible to near IR light. **Figure 4.1** shows a typical schematic of a bulk heterojunction (BHJ) OPD and the energy diagram of a poly(3-hexylthiophene-2,5-diyl):(6,6)-phenyl C_{61} butyric acid methyl ester P3HT:PCBM-based device.

www.manaraa.com

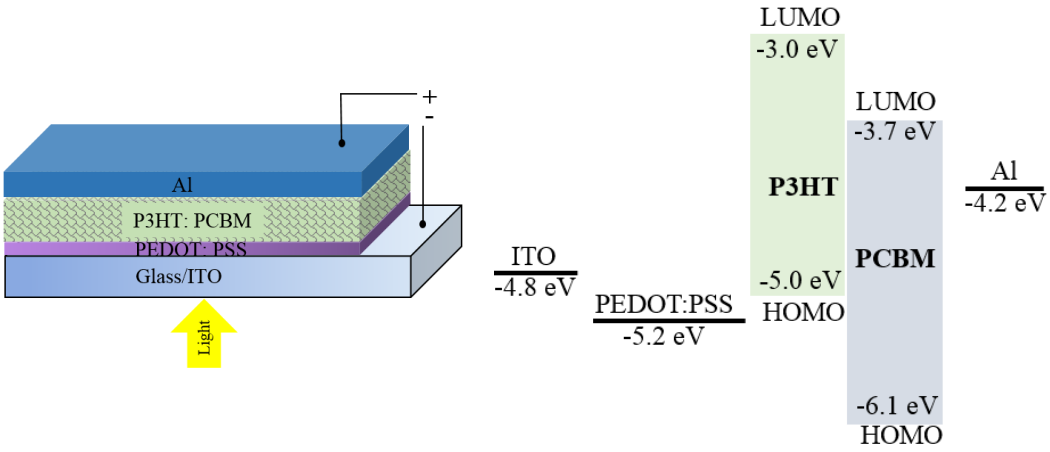

Figure 4.1: Schematic of a BHJ OPD structure and the energy diagram for a P3HT:PCBM-based OPD.

As mentioned, unlike inorganic semiconductors, organic thin films are processed at low temperatures and are therefore compatible with simple flexible substrates irrespective of the substrates' shape; these include wearable and plastic substrates.[15] Deposition techniques of the various thin layers include thermal evaporation (for π-conjugated organic small molecules), spin-coating (typically for polymers), spray-coating, screen printing, micro-printing, and roll-to-roll processing.[16-19] Importantly, the optical and electronic properties of an organic material can be tuned to make it compatible with a specific application.[20]

There are generally four stages of converting light into electric current in photovoltaic devices. An excited electron-hole pair (exciton) state is formed by photons absorbed by the active layer. The generated excitons diffuse to an interface where charge separation occurs. The separated charges travel to the corresponding electrodes, where they are collected. The efficiency of an OPD corresponds directly to the number of created charges that are collected at the electrodes and this number depends on the fraction of photons that are absorbed, the fraction of excitons that dissociate to electrons and holes, and the charge

www.manaraa.com

collection efficiency at the electrodes. The OPD performance is enhanced by optimizing any of these factors. The spectral response of detectors can be tuned mostly by material choice and by adjusting the thickness of the resonant cavity sandwiched between two metal electrodes, using an optical spacer at the anode.[21] For instance, PTB7 (polythieno [3,4-b]-thiophene-co-benzodithiophene)-based OPDs absorb more in a longer wavelength range (550-750 nm) than the well-known P3HT-based OPDs. In addition to the material choice, there are also several novel methods utilizing light trapping or plasmonic effects to maximize absorption in the active layer to enhance exciton formation.[22-25] The exciton diffusion efficiency depends on where the excitons are formed and whether they can diffuse to the donor/acceptor (D/A) interface, where charge dissociation occurs. Since the exciton diffusion length is much smaller in organic materials than in their inorganic counterparts, bulk heterojunction (BHJ) structures are mostly used to ensure exciton formation very close to the D/A interface.[26]

The charge collection highly depends on the carriers' mobility within the transporting layers. Reducing the density of deep traps, which act as recombination centers, whether originating from impurities or structural disorder, can improve carrier mobility. Indeed, carrier mobility was shown to increase with crystalline structure of the organic semiconductor formed during annealing.[27]

Specifically, attributes that are important in characterizing OPDs include responsivity, external quantum efficiency (EQE)/gain, spectral response, dynamic range, response speed, response linearity, the noise equivalent power (NEP), detectivity, and stability. The ratio of the current or voltage output signal to the input power is defined as the responsivity, which improves with increasing EQE. A constant responsivity within a certain wavelength

www.manaraa.com

range or a linear responsivity is highly desired, so that the output signal can be predicted based on a given power input. In OPDs the EQE is typically less than 100%, hence they typically have no internal gain.

High gain in OPDs was recently reported. In an OPD of the structure a ITO/poly(3,4-ethylenedioxythiophene):polystyrene sulfonate (PEDOT:PSS)/fullerene (C_{60})/2,9-dimethyl-4,7-diphenyl-1,10-phenanthroline (BCP)/Al OPD.[28] The high gain was explained by a trapped hole-enhanced electron-injection process, where the photo-generated holes get trapped at the interface of the hole transport layer (PEDOT:PSS) and the active layer component (C_{60}). The high density of trapped holes reduces the electron injection barrier via band bending at the interface, which leads to secondary electron injection from the hole transport material to the active layer. A buffer layer to strongly reduce the dark current and increase the detectivity was inserted between the PEDOT:PSS and the C_{60} layers, but it eliminated the gain.

As mentioned, the spectral response is the wavelength range in which OPDs can function properly. A given OPD can typically respond only to a specific wavelength range, and proper materials need to be selected to match the input optical signal. The dynamic range is defined as the ratio of the maximum and minimum detectable power in dB. Another key attribute is the OPD's response time, which is characterized by the rise and fall times in response to an input signal. Also, a linear output over a broad range of light intensities is beneficial, and to get an accurate response the noise should be low. Obviously, the input power should be no less than the NEP, which is defined as the input power at which the SNR is unity.

www.manaraa.com

Clearly, a high specific detectivity D*, which defines the ability of a PD to detect a small optical signal, is wanted; D* equals the reciprocal of the NEP normalized to the square root of the sensor's area and frequency bandwidth in Jones units ($\boldsymbol{cm\ Hz^{1/2}W^{-1}}$), i.e.,

$$D^* = \frac{\sqrt{A * \Delta f}}{NEP} \qquad 4.1$$

Where A is the photosensitive area of the PD and Δf is the frequency bandwidth. Beyond all these factors, obtaining high stability insures reproducibility over time, which is a major challenge in OPDs.

4.3. OPDs in Analytical Sensing

The use of OPDs in analytical sensing is a multidisciplinary endeavor that involves optics, organic electronics, microfluidics (mechanical engineering), and chemical and biological sciences. OPDs can be employed in optical sensing in several ways, with the majority of the sensors utilizing two different luminescent processes, bio/chemiluminescence (CL) and/or photoluminescence (PL).[2-4] In this review we highlight examples of OPDs' use in CL/PL sensors as well as in absorption measurements.

4.3.1. Chemiluminescent assays

CL occurs during the progression of some chemical reactions where an electronically excited state is generated. CL sensors are utilized in immunoassays and for nucleic acid detection, where an emitting compound is used as a label.[29] Such sensors often utilize oxidation of a material in an excited state.[30] The emitted light intensity depends on the concentration of the reactive material or on the rate of the chemiluminescent reaction. Having no background emission from an external excitation source, the limit of detection (LOD) for these detection systems is very low.

www.manaraa.com

Though the usage of CL in analytical applications is not new, compact, easy to use designs for e.g., healthcare systems are yet to be developed.[31-35]. An example of a point-of-care CL sensor set up includes a (poly)dimethylsiloxane (PDMS) microfluidic chip (made by soft lithography) with two inlets, one outlet and a reaction/detection chamber. The two inlets are connected to syringe pumps where the flowing rate of reagents can be controlled. Sometimes a third syringe pump is used to inject catalysts. The PD is located underneath or above the detection chamber.

Numerous studies have been reported on peroxyoxalate CL (POCL) sensors for monitoring H_2O_2 with a PMT [36-38] or a silicon photodiode [39-41]. Hoffman et al. showed [42] that these POCL sensors can be further miniaturized by successfully integrating an organic copper phthalocyanine /fullerene- ($CuPc/C_{60}$) based OPD with PDMS microchannels. The EQE of this OPD was 30% at 600-700 nm. With an optimized flow rate (~25 μL/min) of POCL reagents, a steady state CL-induced photocurrent of 8.8 nA was achieved within 11 min with excellent reproducibility. But although the photocurrent vs H_2O_2 concentration was linear up to 1 M, the H_2O_2 LOD was only 1 mM, whereas with a PMT and Si photodiodes it was as low as 5 μM [43]. An inadequate alignment of the detection chamber and the OPD, as the size of the $CuPc/C_{60}$ OPD (16 mm^2) was larger than that of the microfluidic detection chamber (2 mm^2), led to higher dark/background current (~6 nA/cm^2), which restricted the LOD significantly. Consequently Wang et al. [44] reported POCL detection with a solution processed P3HT:(6,6)-phenyl C_{61} butyric acid methyl ester (PCBM) OPD, where the OPD was comparable in size (1 mm^2) and aligned properly with the detection chamber. With this geometry and OPD, a LOD of 10 μM H_2O_2 was achieved at an optimum flow rate of 75 μL/min, which is comparable to the LOD obtained with a Si

www.manaraa.com

photodiode.[43] Later the same group successfully utilized this integrated system for antioxidant detection screening.[45] They injected various plant-based antioxidants e.g., α-tocopherol (vitamin E), β-carotene (vitamin A), and quercetin to the stream of POCL reagents in PDMS microfluidic channels to detect the antioxidant concentration in the aforementioned biological extracts. The CL signal was detected by the P3HT:PCBM OPD, which had a broadband photoresponse ranging from 350 to 650 nm with a peak responsivity of 0.25 A/W at 550 nm and a dark current density of 0.59 μA/cm^2. The results showed a linear trend of the CL intensity with the antioxidant concentration in the range of ~2 μM to 200 μM and the LOD was comparable to that achieved with a PMT.

Wojciechowski et al. [46] presented the integration of a solution processed P3HT:PCBM OPD with a disposable biosensor chip that included a microfluidic channel with an immobilized capture antibody for Staphylococcal Enterotoxin B (SEB). The OPD monitored the CL from the biotinylated α-SEB capture antibody/SEB/horseradish peroxidase (HRP)-conjugated α-SEB antibody (α-SEB-HRP) assay. A LOD of 0.5 ng/mL was obtained due to a low dark current (noise) (<10 nA/cm^2) obtained under a small reverse bias (up to -100 mV). The reported LOD was comparable to that obtained with PMT and CCD-based detection.

Pires et al. reported a CL sensor [47] that consists of an immunoassay chip with biomolecules immobilized on an Au coated glass substrate and an optimized BHJ OPD with the structure ITO/PEDOT:PSS/poly[N-9`-heptadecanyl-2,7-carbazole-alt-5,5-(4`,7`-di-2-thienyl-2`,1`,3`-benzothiadiazole)] (PCDTBT):PC$_{70}$BM/LiF/Al. The immunoassay was employed to detect recombinant human thyroid stimulating hormone (rhTSH), a marker for diagnosis of thyroid cancer. In addition to using PCDTBT (instead of P3HT),

www.manaraa.com

which is known to lead to a higher short circuit current,[48] the OPD was further optimized by changing the thickness of PEDOT:PSS and the active layer. Hence, a low LOD was obtained with the OPD monitoring the ~425 nm CL signal due to the interaction between anti-rhTSH monoclonal antibody, rhTSH antigen, and a biotinylated secondary antibody complex together with HRP. Later Pires et al. integrated the PCDTBT:$PC_{70}BM$–based OPD with a microfluidic biosensor for protein analysis [49]. For the detection of rhTSH, an excellent linearity in the range of 0.03 to 10 ng⁄mL was achieved with high sensitivity and reproducibility.

TSH detection in clinical samples was further demonstrated to verify the potential application of the biosensor in clinical testing. Following the successful detection of rhTSH; the same technique was employed for detecting the stress hormone cortisol using an appropriate antibody and fluorophore.[50] The same OPD was used due to its very low dark current (~17 pA/cm^2) and high EQE (>60%); achieving a detection sensitivity of 1.775 pA/nM and a LOD <0.28 nM with the integrated system. Pires et al. have also reported a poly(methylmethacrylate) (PMMA) multiplexed microfluidic biosensor integrated into an array of OPDs (Figure 2) for CL detection of pathogens e.g.; waterborne Escherichia coli O157:H7; Campylobacter jejuni; and adenovirus.[51] The optimized PCDTBT:$PC_{70}BM$-based OPD exhibited a responsivity >0.20 A/W at 425 nm for the multiplexed detection tests. Parallel analysis of the three inactivated bacteria mentioned earlier; in the spiked drinking and surface water samples; was achieved within 35 minutes and the LODs were 5×10^5 cells/mL for E. coli; 1×10^5 cells/mL for C. jejuni and 1×10^{-8} mg/mL for adenovirus. The reported device can potentially be employed for simultaneous detection of up to sixteen analytes within a short period of time.

www.manaraa.com

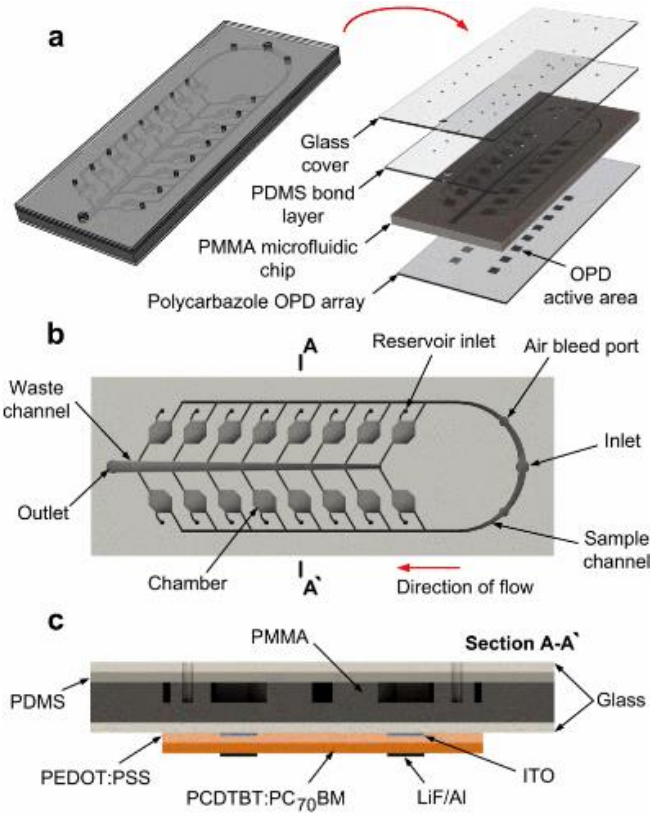

Figure 4.2: (a) Illustration of the multiplexed optical-biosensor platform integrating an array of polycarbazole OPDs to a hybrid microfluidic chip made of PMMA and PDMS. (b) Top view of the PMMA microfluidic substrate with ~30 mm^3 volume chambers. (c) Cross-section view of the integrated device illustrating all device components (not to scale) Reproduced with permission from Tao Dong from reference [51], Sensors, published by MDPI (2013).

Expanding this work, Dong and co-workers presented a concept of a capillary-driven sensing device integrated with an OPD.[52] The characterization of the proposed device model containing eight reaction chambers joined with microfluidic channels was done by finite element method simulations and the results were verified experimentally for a single chamber utilizing a CL reaction that occurred due to the HRP-luminol-peroxide interaction. However, differences in analytical sensitivity were noticed among the different chambers due to a non-uniform filling process. It was also demonstrated that the detection sensitivity of CL-based sensing can be improved by incorporating gold nanoparticles (AuNPs) with a PDMS-glass hybrid microfluidic chip.[53] Due to the enhancing effect of the AuNPs on

www.manaraa.com

HRP-luminol-H_2O_2 CL and the very high detectivity of the PCDTBT:$PC_{70}BM$ BHJ OPD (D* ~$9.2x10^{11}$ Jones under 0.22 mW/cm^2 irradiation at 428 nm), the reported CL immunosensor was ~200 fold more sensitive than previously reported similar sensors achieving a very low LOD of 2.5 pg⁄mL for 17-β estradiol. This enhancement effect of AuNPs, when integrated with ring shaped OPDs and capillary-induced flow in microfluidic channels for field CL detection of a waterborne pathogen (Legionella pneumophila), resulted in a resolution of $4x10^4$ cells/mL, with a 25 fold improvement over previously reported sensing without AuNPs. [54]

4.3.2. PL-based chemical/biological sensors

PL-based sensors typically comprise an excitation source, a sensing element that is often a thin organic film or a solution with an analyte-sensitive dye, a PD, and the electronic circuitry. The excitation source is used for excitation of the sensing material whose PL depends on the dose of the analyte. Thin film PDs in PL-based bio/chem sensors have demonstrated high detection sensitivities with the advantages of simple fabrication and ease of integration in all-organic devices that are potentially low cost. That is, OPDs can be integrated with thin sensing films or microfluidic channels with the sensing element, and with OLED excitation sources to generate compact, yet sensitive monitors. [55-59]

The structure of PL-based sensors is similar to that of CL sensors, [2,8,12] though the working principle is different. In PL-based sensors the analyte-dependent PL intensity *I* and/or decay time τ of the analyte-sensitive material are monitored. For example, optical monitoring of O_2 is based on examining the quenching of *I* and/or the decrease of τ of an excited oxygen-sensitive dye such as Pt octaethylporphyrin (PtOEP) or the Pd analog

www.manaraa.com

PdOEP. This quenching is due to collisions of the excited dye with O_2 in a dynamic Dexter process. [60] Ideally this process is described by the Stern–Volmer (SV) equation 2. [61]

$$\frac{I_0}{I} = \frac{\tau_0}{\tau} = 1 + K_{SV}[O_2] \qquad 4.2$$

Where I_0 and τ_0 are the PL intensity and decay time, respectively, at 0% oxygen, and I and τ are the values in the presence of oxygen. K_{SV} is the SV constant.

Structurally integrating a PL-based sensor would enable numerous point-of-care applications, however, for sensitive detection, a strong excitation source to excite the sensing material is needed. When using a lamp, an OLED, or an inorganic LED, an optical filter or other means are often essential for suppressing the excitation light from reaching the PD. [62,63] Banerjee et al. used a broadband halide lamp (narrowed by a band pass filter) for excitation of 1 μL rhodamine 6G dissolved in ethanol and contained in a PDMS microfluidic channel. A CuPc/C_{60}-based OPD was used for generating a cost effective detection. [64] To address the issue of interfering light from the excitation source the authors devised a cross-polarized scheme, where the excitation light passed through a linear polarizer and the dye's fluorescence (and the excitation light) passed through a second linear polarizer placed orthogonally to the former. As a result, the photocurrents measured by the CuPc/C_{60}-based OPD due to the excitation source (without the sensing component) and the dye's PL reduced by 25 dB and 3 dB, respectively improving the SNR. Hence, utilizing this approach, the signal from analytical assays monitored by an OPD can be significantly improved. With this system, a LOD of 10 nM was obtained for several fluorescent dyes such as the common rhodamine 6G and fluorescein. Next, Banerjee et al. replaced the halide excitation lamp with a green tris(8-hydroxyquinolinato) aluminum (Alq_3)-based OLED, [65-67] however, a higher 100 nM LOD was obtained with this on-chip

www.manaraa.com

design. The LOD was lowered to 10 nM by using an alternating CuPc/C_{60} bilayer OPD, which has a responsivity 10 fold better than that of a single layered heterojunction OPD.[66]

Kraker and co-workers addressed the SNR due to the interfering excitation light in a similar approach. [68] They used polarizer foils as substrates as well as filters, filtering out the excitation light of a green Alq_3-based OLED (for oxygen sensing) and of a blue OLED (for pH monitoring). A CuPc/perylene-tetracarboxylic bisbenzimidazole (PTCBI) -based OPD was used for detection of luminescent Pt(II)meso-tetra(pentafluorophenyl)porphine (Pt-TFPP) embedded in a polystyrene matrix and fluorescein isothiocyanate (FITC) in a pH buffer solution for oxygen and pH monitoring, respectively.

Optical wave-guiding can also be employed to increase the SNR and eliminate the need for optical filters. [69-73] Mayr and co-workers [69-70] developed such a sensor array with integrated OPDs, where optical filters were not required due to the platform's geometry (**Figure 4.3**), which enabled separation of the excitation light from the PL signal. As shown in the figure, ring-shaped OPDs were fabricated on the back side of a glass slide or on a polymeric substrate and the sensing film was prepared either on the opposite side of the substrate (for PL-based sensing) or immobilized inside the waveguide layer (Figure 4.3b) (for-absorption-based sensing). For the PL sensor, the sensing film was illuminated by a 450 nm LED through an aperture and the sensing signal was guided through a substrate with a higher refractive index toward the ring shaped OPD array. In this case, a stable fluorophore is excited by the LED and the emitted guided fluorescence is partially absorbed by an immobilized absorber and then deflected toward the OPD array by a scatterer. The OPDs were chosen to be a pn heterojunction diode based on CuPc: PTCBI due to their compatible spectral response with the sensing elements and high on/off ratio (64dB), i.e.,

www.manaraa.com

high photocurrent/dark current ratio. The OPDs were stable under non-inert conditions and exhibited minimal degradation at 0 V. The ring-shaped OPD geometry was successfully employed to monitor oxygen, carbon dioxide, relative humidity, and pH in aqueous and gaseous media.

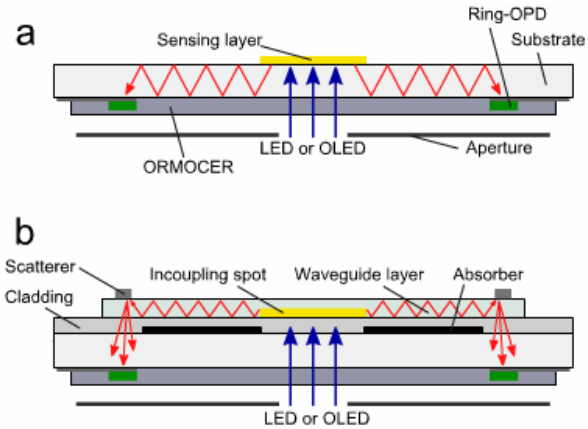

Figure 4.3: Schematic side view for the luminescence-based (a) and absorption-based (b) sensor chip (sizes are not to scale). The figure is reused from reference [70] © Springer-Verlag 2012 with kind permission from Springer Science and Business Media.

In 2010, Nalwa et al. demonstrated a structurally integrated all organic sensing platform, which included an OLED excitation source, a dye for oxygen and glucose sensing, and a P3HT:PCBM OPD. [74] The spectral response of the P3HT:PCBM-based OPD was tuned to achieve a better photoresponse for the red emission of the PtOEP sensing dye. A thicker and slower-grown P3HT:PCBM BHJ layer was generated for this reason and it resulted in a 40% EQE at ~640 nm, the peak emission of the sensing dye. Oxygen and glucose concentrations were monitored using this optimized OPD via detection of the phosphorescence I and τ of the dye (Eq. (2); first temporal measurement for an all-organic device). In particular, the fast response of the OPDs enabled oxygen detection using the τ mode. **Figure 4.4** shows the oxygen and glucose monitoring results.

www.manaraa.com

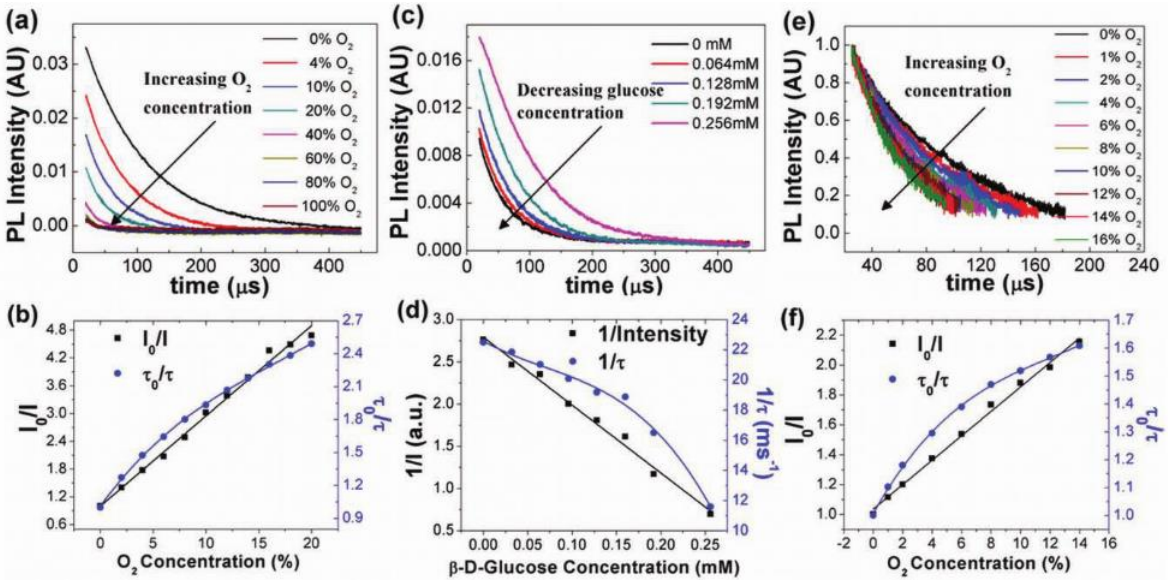

Figure 4.4: The effect of concentration of gas-phase O_2 (a) and (e), and of glucose (c) on the OPD's temporal photocurrent response. The excitation sources were LED (for a-d) and OLED (for e-f). Figure reused with permission from reference [74] Copyright © 2009 John Wiley & Sons, Inc.

Later Liu et al. [75] addressed different challenges that limit the LOD in all organic integrated sensors. These challenges include the OLEDs' broad EL band, the OLEDs' low (forward) outcoupling factor, and the transient EL profile (i.e., the EL vs. time following an OLED pulse), including the long EL temporal tail in some OLEDs, in particular in guest-host OLEDs.[76] To achieve a high sensitivity from an all organic integrated detector, Liu et al. used narrower band emission green and blue microcavity OLEDs (μcOLEDs). The narrower EL improved the SNR significantly. Furthermore adding polyethylene glycol (PEG) to the PtOEP:PS sensing matrix resulted in a porous microstructure that served a dual purpose: it led to an increase in the absorption by the dye due to scattering by voids that increased the optical path of the excitation source, and as a result increased the PL. Apparently it also increased the phosphorescence that was directed toward the OPDs, and a PEG:PS film (devoid of the dye) was used also to enhance the OLEDs' outcoupling

www.manaraa.com

factor. Though adding PEG to the sensing matrix reduced the detection sensitivity by a factor of 1.7, it enhanced the PL signal by x2.7, which is crucial when using OPDs. In the all organic sensors, it was shown that the small molecule CuPc/C_{70}-based OPD is preferred for red PL over the P3HT:PCBM OPD that has a stronger responsivity for the green excitation light. Using both CuPc/C_{70} and P3HT:PCBM OPDs (**Figure 4.5a**), a dual sensing platform for dissolved O_2 (DO) and pH monitoring was demonstrated using green and blue μcOLEDs, respectively.

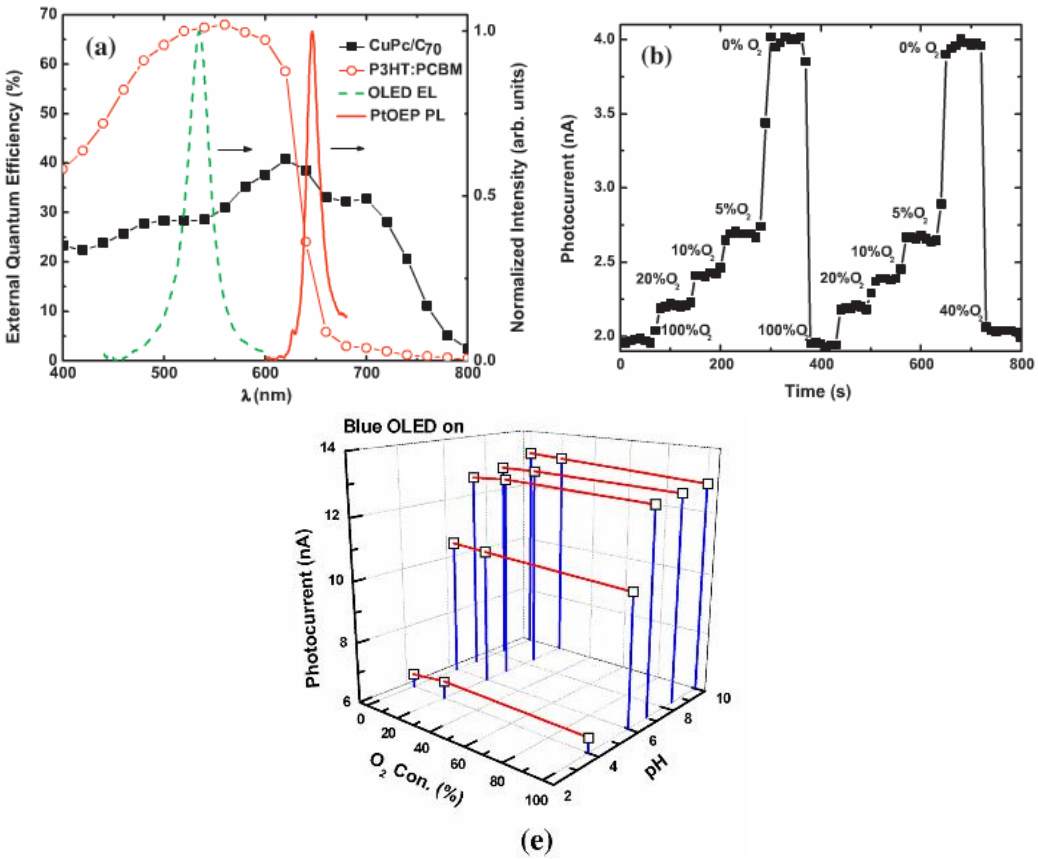

Figure 5. (a) EQE of CuPc/C70 (black) and P3HT:PCBM (red)-based OPDs, the EL of the microcavity (μC) OLED (dashed green line), and PL of the sensing film (solid red line). (b) The sensing signal excited by the μC OLED detected by CuPc/C70 OPD at various O2 concentrations. (c) The signal intensity detected by the P3HT:PCBM OPD at different O2 and pH levels with the blue μC OLED. Reprinted from reference[75] Copyright (2013), with permission from Elsevier B.V.

www.manaraa.com

Extending the previous work, Manna et al.[77] replaced the green μcOLED with a near UV μcOLED as the excitation source for an all-organic oxygen sensor. Since the oxygen sensitive dyes PtOEP and PdOEP have a stronger absorption in the near UV, the use of the near UV device significantly enhanced the SNR. Moreover, a more sensitive PTB7:PCBM-based OPD was used instead of P3HT:PCBM due its higher photoresponse at the longer wavelength range compared to the wavelength range of the excitation source. The PTB7:PCBM-based OPD, together with near UV μcOLED, enabled monitoring the entire range (0-100%) of oxygen level in contrast to the green excitation source that exhibited a lower SNR.

Lefèvre and co-workers reported the first miniaturized all organic fluorescent sensor integrated into a microfluidic chip. [78] A blue 4, 4`-bis-(2, 2-diphenyl-ethen-1-yl) biphenyl (DPVBi) OLED was used as the excitation source and a PTB3:$PC_{61}BM$ BHJ as the OPD. The OPD was highly sensitive at 600 – 700 nm with an EQE of 47% at 685 nm, and thus it was appropriate for detecting fluorescence of green algae (**Figure 4.6b**). The detection system was integrated with a PDMS microfluidic chip with two color filters to prevent undesired light from the excitation source from reaching the OPD; the filter blocking the longer wavelength part of the OLED's emission was between the microfluidic chip and the OLED, while the filter for blocking the excitation light was between the microfluidic chip and the OPD. The sensor was used for pollutant detection. A 10 μL of 1×10^6 cells/mL green algal culture (Chlamydomonas reinhardtii (CC-125)) mixed with herbicide Diuron was excited by the pulsed blue OLED and the fluorescence from the algal chlorophyll was measured by the OPD. The OPD was operated under zero bias, keeping the dark current at < 1 nA/cm^2. The fluorescence of the green algae enabled the evaluation of the number of

www.manaraa.com

algal cells present in the medium and the toxic effects of the Diuron pollutant at a concentration as low as 11 nM. Figure 5 shows the spectra of the three sensor components (OLED's EL, absorption and fluorescence of green algae, and EQE of the OPD) in the integrated setup; the algae's fluorescence as measured by the OPD, and for comparison, by a commercial fluorometer.

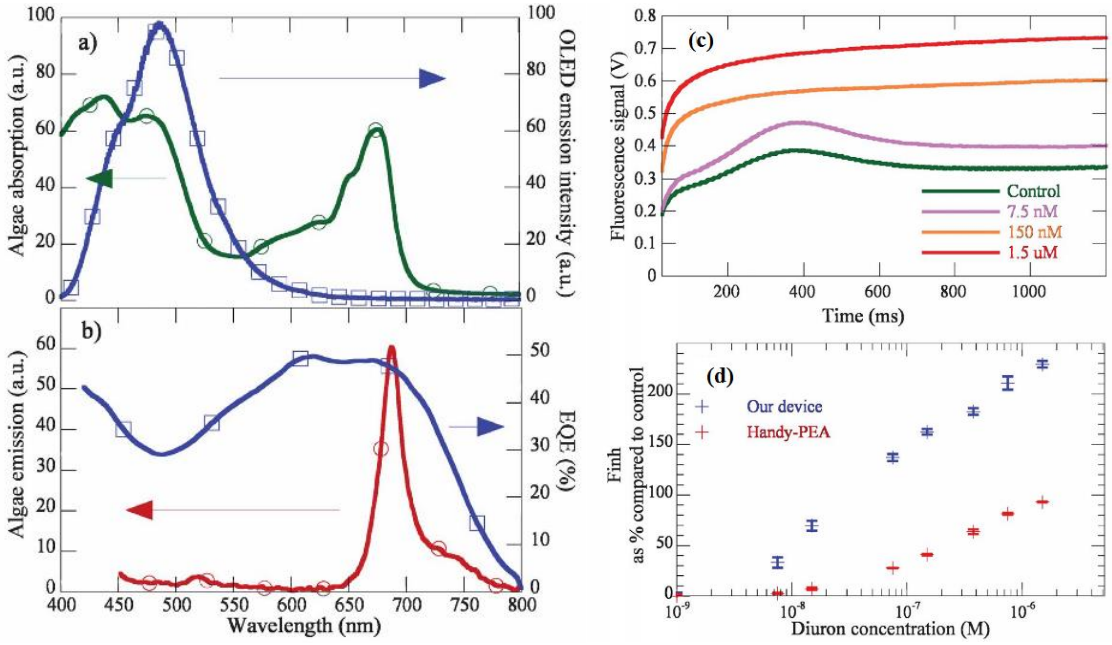

Figure 4.6: (a) Absorption spectrum of the green algae CC125 and the blue OLED emission spectrum. (b) Fluorescence emission spectrum of the green algae CC125 and the EQE of the PTB3/$PC_{61}BM$ OPD at 0 V (c) Algal fluorescence signal detected with the OPD for different concentrations of the herbicide Diuron (d) Variation of the inhibition factor of algal fluorescence (calculated) as function of Diuron concentration. Reproduced from reference [78] with permission of The Royal Society of Chemistry.

Bradley and coworkers [79] demonstrated a compact, low cost, and practical fluorescence detection system (**Figure 4.7a**) for potential lab-on-a-chip/point of care testing applications using a commercially available InGaN LED (501 nm) as the excitation source, polystyrene microfluidic chip for fluorescence immunoassays and a P3HT:PCBM OPD for detection of the two cardiac markers myoglobin and CK-MB. They used both absorptive dye coated color filters and linear and reflective polarizers to suppress the

www.manaraa.com

background due to LED's leakage EL and to enhance the SNR. The performance of the OPD was compared to that of a low cost commercial large area Si PD with a similar spectral response. Diluted fluorescent beads TransFluoSphere® were used to determine the optical LOD of this sensor setup. The EQE of the BHJ P3HT:PCBM OPD exceeded 40% across the wavelength range of 400–600 nm due to its strong absorption in this range, with a peak EQE of 58% at 520 nm, whereas the peak EQE of the Si PD was ~19% at 560 nm as shown in Figure 4.7b (we note that this commercial Si PD is likely not the state of the art). The (undesired) 4% EQE in the longer wavelength range of the Si PD also reduced the SNR. The OPD was thus proven to be a good match for the TransFluoSphere® emission band (570–700 nm) that was used to determine the optical LOD of the system.

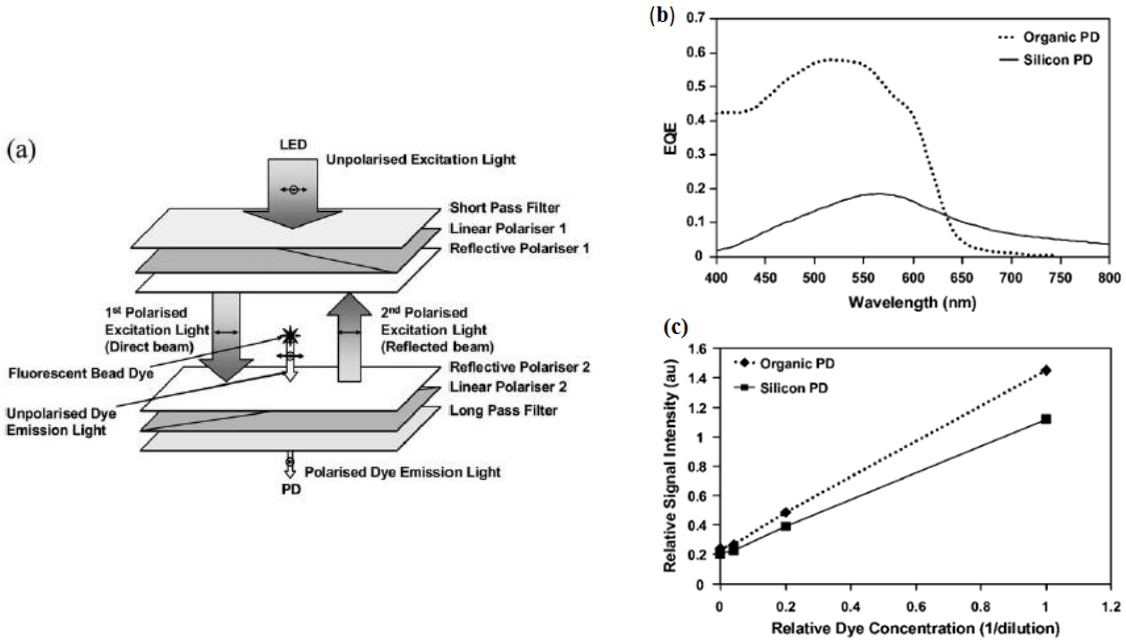

Figure 4.7: (a) Schematic of the sensing setup. (b) Comparison of EQE spectra of organic and Silicon PD (c) measured signal intensity as a function of TransfluoSphere bead suspension concentration using OPD and silicon PD (with IR blocking filter) Reproduced from reference[79] with permission of The Royal Society of Chemistry.

www.manaraa.com

The comparison of the detection by the inorganic and organic PD is shown in Figure 4.7c. The LOD was 5.6 x10^4 beads μL^{-1}(comparable to ~3 nM fluorescein) for microbeads and 1.5 ng mL^{-1} for both myoglobin and CK-MB for the human plasma immunoassays.

Imato and coworkers [80-83] utilized various OPDs toward an integrated optical detection system on a microchip for fluorometric immunoassays and other photometric studies. Two types of immunoassays, sandwich and competitive enzyme-linked immunosorbent assay (ELISA), for various analytes, were studied using an immobilized primary antibody (specific to the analyte) and HRP labeled secondary antibody. Amplex Red, which produces fluorescent resorufin by an enzymatic reaction with HRP in the presence of H_2O_2 was employed as a substrate in the assay. A LED or OLED was used to excite resorufin, the product of the immunoassay, while OPDs were used to detect the fluorescence from it. First, a heterojunction CuPc/C_{60}-based OPD with ~20% IPCE was successfully employed in a flow-immunoassay for the human stress marker immunoglobulin A (IgA) with a LOD of 16 ng/mL; the LOD for resorufin was 5 μM.

Recently, a similar OPD was used for the determination of phosphate utilizing the ion-association reaction between Malachite green (MG) and molybdenum phosphate complex. [83] The efficiency of the detection system was improved via the use of an europium (diben-zoylmethanato)$_3$ (bathophenanthroline)-based OLED with a narrow band (FWHM ~8 nm) emission peaking at 612 nm instead of a LED, achieving a linear detection in the concentration range of 0-0.2 ppm with a LOD of 0.02 ppm. Later, the layered heterojunction CuPc/C_{60} OPD was replaced with a BHJ CuPc:C_{60}-based OPD exhibiting an improved LOD (see below) in a competitive ELISA for an environmental pollutant, alkylphenol polyethoxylates (APnEOs).[81] The enzymatic reaction time was shortened

www.manaraa.com

with anti-APnEOs antibody immobilized on magnetic microbeads instead of on the microchip. The OPD was suitable for detecting the fluorescence of resorufin, attaining LODs of 2 or 4 ppb for antibodies immobilized on the PDMS microchip or on microbeads, respectively. To enhance the efficiency further, Imato and co-workers fabricated a BHJ tris[4-(5-phenylthiopen-2-yl)phenyl]-amine (10%) (TPTPA): fullerene (C_{70})-based OPD. Utilizing the higher absorptivity of these materials and higher IPCE (~44%) due to the larger interface area in the BHJ structure, the OPD exhibited a linear resorufin detection range of 0-18 μM with a LOD of 0.6 μM, whereas the LOD achieved for APnEOs was ~1-2 ppb. Interestingly, although the IPCE of the TPTPA:C_{70}-based OPD was much higher than the C_{60}:CuPC based OPD, the SNR (~3) was very similar in all cases.

With a similar approach, Köstler and coworkers [84] demonstrated a PL-based capillary oxygen sensor. The sensing layer, comprised of a fluorescent dye embedded in a polymeric matrix, was homogeneously coated on the inner wall of a capillary tube exposed to a flowing analyte. The sensing film was optically excited by a LED through a small aperture and the sensing signal travelled through the capillary tube to the OPD formed on the external side of the capillary tube. This structure, formed on the capillary tube, was possible since the organic materials can be easily deposited on non-planar substrates. The results for oxygen sensing in the intensity mode were consistent with the expected behavior, though background light reduced the sensor's efficiency.

4.3.3. Light scattering and absorption

Charwat et al. [85] showed that a simple light scattering method can be very convenient for monitoring an adherent cell population using an OPD. They utilized a PDMS microfluidic biochip (**Figure 4.8**) sandwiched between two glass slides, one contained an

www.manaraa.com

appropriate notch filter, while the other connected the microchannels to external fluidic reservoirs. The OPD was underneath the microfluidic chip. The microfluidic channel was illuminated by a 488 nm collimated laser beam and the scattered light from HeLa cells was monitored by measuring the OPD's photocurrent. The latter increased with increasing cell numbers as shown in Figure 4.8.

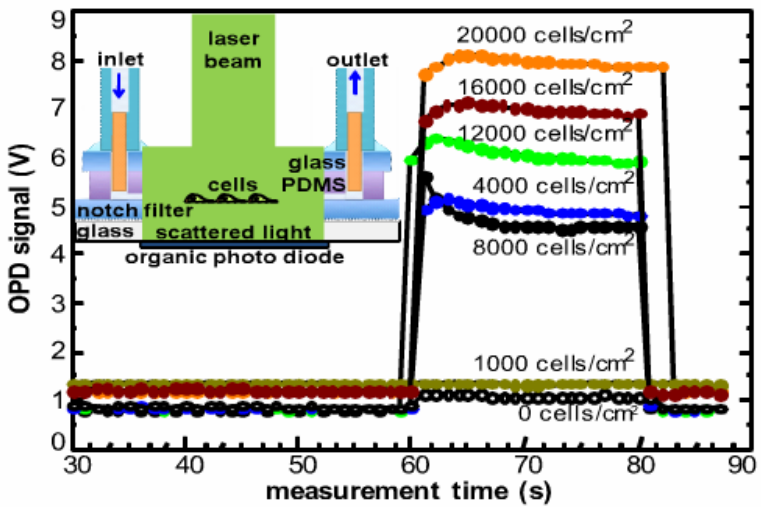

Figure 4.8: Light scattering raw data of increasing concentration of living HELA cells cultivated on chip surfaces. © 2011 IEEE; reprinted with permission, from reference[85]

Later the same group developed a miniaturized cell analysis platform by combining the OPD light scattering measurement approach with impedance spectroscopy, which enabled studying cell adhesion and cell-cell interactions in addition to monitoring the cells growth.[86] Regioregular P3HT: $PC_{61}BM$ BHJ OPD arrays were fabricated by spray coating on ITO-coated glass containing embedded interdigitated electrode structures (IDES) for impedance spectroscopy. **Figure 4.9** shows the impedance spectroscopy and light scattering results of a brain metastasis prostate carcinoma cell line (DU-145) when treated with cycloheximide (CHX), which is an inhibitor of protein biosynthesis. While the change in impedance of the CHX-treated cells was insignificant compared to a control experiment,

www.manaraa.com

the increased light scattering by the treated DU-145 cells measured by the OPD arrays showed the rising of intracellular granularity, which is an early sign of apoptosis. Thus, the platform geometry, which provides freedom regarding sensor geometry, area, and height due to its simple spray coating fabrication, can be a useful tool for monitoring cell growth and interactions under different conditions.

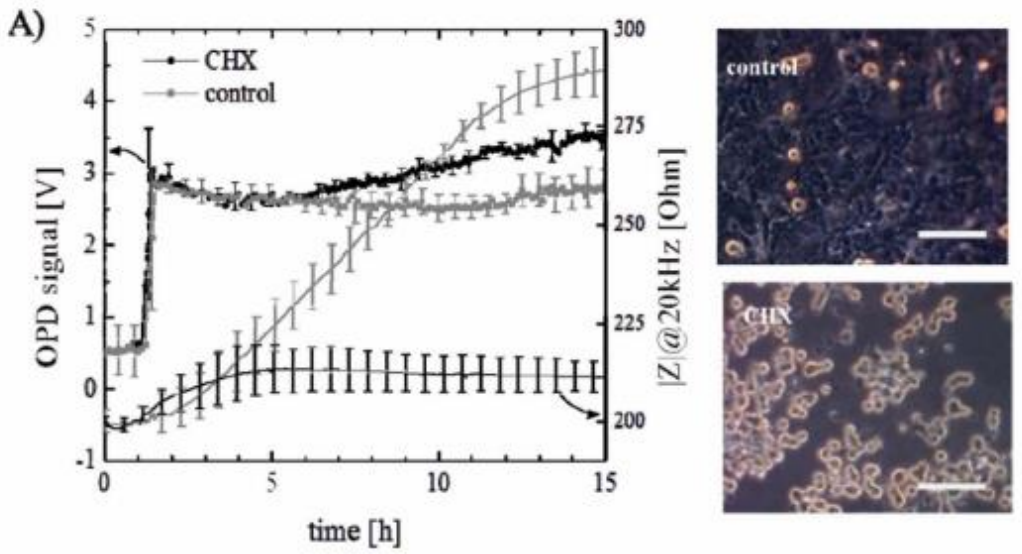

Figure 4.9: Averaged (n = 3) light scattering-time and impedance-time traces obtained for DU-145 cells (density ~ 0.9 x10^5 cells/cm^2) seeded in the absence (gray) and presence (black) of 2 µg ml^{-1} CHX. The images show phase contrast of DU-145 carcinoma cells in the absence (control) and presence of CHX. Reproduced from reference [86] with permission of The Royal Society of Chemistry.

The integration of OPDs and OLEDs with a pulse oximetry detection system demonstrated by Lochner and coworkers shows enormous potential of such integrated systems in the medical device field. [87] As shown in **Figure 4.10**, spin-coated green (poly(9,9-dioctylfluorene-co-n-(4-butylphenyl)-diphenylamine)(TFB):poly((9,9-dioctylfuorene-2,7-diyl)-alt-(2,1,3-benzothiadiazole-4,8-diyl)) (F8BT)-based and red (TFB:F8BT:poly((9,9-dioctylfluorene-2,7-diyl)-alt-(4,7-bis(3-hexylthiophene-5-yl)-2,1,3-benzothiadiazole)-20,20-diyl) (TBT)-based) OLEDs were fabricated on patterned ITO substrates whereas PTB7:$PC_{71}BM$-based OPDs were printed on a polyethylene

www.manaraa.com

naphthalate (PEN) by the blade coating technique. The OPD exhibited high EQE at the peak emission wavelengths of the OLEDs (38% and 47% for green and red OLEDs, respectively) with a low dark current of 1 nA/cm^2 (at -2 V) and excellent stability. The OLEDs' EL was absorbed by pulsating arterial blood, non-pulsating arterial blood, venous blood and other tissues as shown in Fig. 10b and the change in transmitted signal was measured by the OPD at zero bias to keep the dark current as low as possible. Light absorption in the finger is maximal during the systole phase, due to the large amount of fresh arterial blood, and minimal during the diastole, whereas the absorption due to other parameters is unchanged.

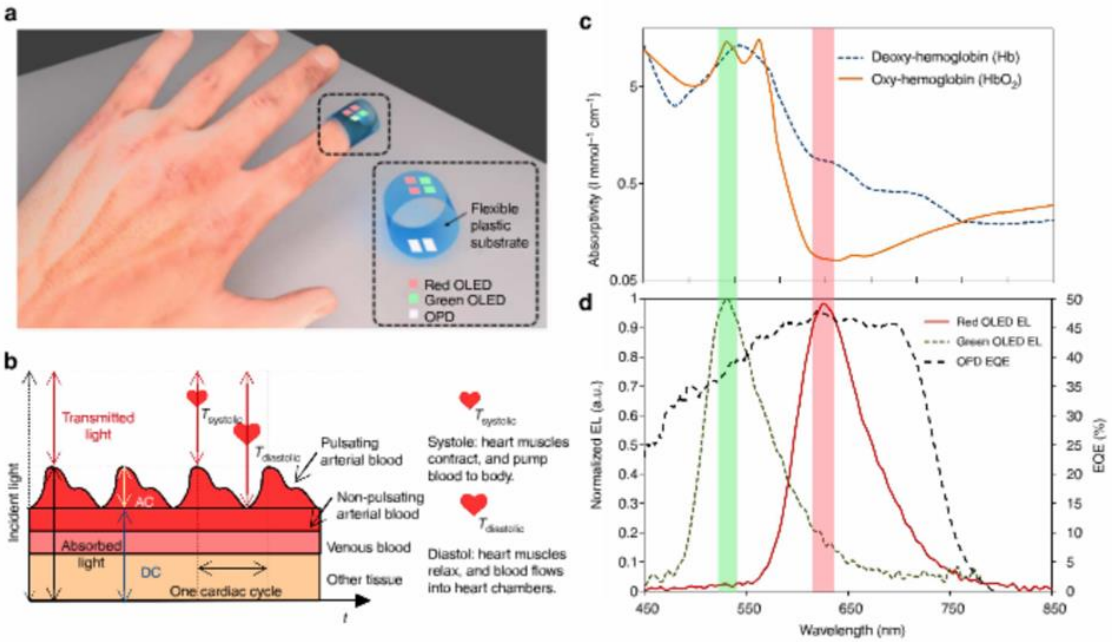

Figure 4.10: (a) Pulse oximetry sensor composed of two OLED arrays and two OPDs. (b) A schematic illustration of a model for the pulse oximeter's light transmission path through pulsating arterial blood, non-pulsating arterial blood, venous blood and other tissues over several cardiac cycles. (c) Absorptivity of oxygenated (orange solid line) and deoxygenated (blue dashed line) hemoglobin in arterial blood as a function of wavelength. The wavelengths corresponding to the peak OLED electroluminescence (EL) spectra are highlighted to show that there is a difference in deoxy- and oxy-hemoglobin absorptivity at the wavelengths of interest. (d) OPD EQE (black dashed line) at short circuit, and EL spectra of red (red solid line) and green (green dashed line) OLEDs. Reprinted with permission from Macmillan Publishers Ltd: Nature communications, from reference [87] copyright (2014).

www.manaraa.com

The continuous change in the OLEDs' EL transmitted through the finger when measured by the OPD gives a perfect measure of the pulse rate with only 1% error. Utilizing the difference in absorptivities of oxy- and deoxy-haemoglobin (Figure 4.10c), the integrated system was also successfully employed to measure arterial oxygen saturation with only 2% error. It was also shown that the background current of the OPD, under ambient light conditions, can be significantly reduced by flexing the OPD around the finger instead of keeping it flat during the measurement, thus improving the detector efficiency and accuracy.

4.3.4. On-chip spectrometer

Ramuz et al. demonstrated an integrated sensing platform that involved a three stage detection scheme built on a Ta_2O_5 planar waveguide.[88] At the first stage, a photoluminescent layer of poly [2-methoxy-5-(2'-ethyl-hexyloxy)-1,4-phenylene vinylene] (MEH-PPV) located directly on top of a waveguide was excited by an iridium (III) tris(2-(4-totyl)pyridinato-N,C2) ($Ir(mppy)_3$)-based OLED. The PL from the MEH-PPV layer was coupled into the single-mode waveguide via evanescent coupling and the guided light interacted with an analyte on its way to the detector. The interaction stage consisted of a microfluidic system, for bringing the analyte to the detection zone, and a $SiO_2/TiO_2/Cr/Au/TiO_2$ surface plasmon resonance (SPR) stack. The interaction of the guided light occurred either via direct absorption by the labeled analyte, or via exciting a SPR mode, depending on the surface condition (change in refractive index) of the SPR stack in the presence of the analyte. In either case there is a significant absorption or a peak shift in the guided light as it reaches the outcoupling grating stage at the PD array. The rectangular gratings, machined directly in the waveguide with a period of 312 nm and

www.manaraa.com

height of 12 nm, diffract the guided light into wavelength-specific solid angles and the light is then collected by a 40 pixels of a P3HT:PCBM-based OPD array with 70% EQE and a lifetime of 3000 hours. Finally, this fully organic mini-spectrometer, with overall spectral resolution of 5 nm, was employed to demonstrate an absorption-based bio-test with mouse immunoglobulin G (mIgG) and its antibody labeled with Cy5 marker, and for label-free detection via the SPR scheme by changing the surface refractive index of the SPR stack.

With a similar motivation to build an on-chip all organic spectrometer, Liu et al. [89] fabricated a multicolored μcOLED array, emitting in the range of 490 to 660 nm, on a single substrate, by tuning the thickness of the optical cavity. A 2-d combinatorial array of μcOLED pixels was employed to build this compact, integrated spectrometer. To demonstrate the potential of these tunable μcOLED arrays for on-chip applications, 12 different colored pixels on a 2"×2" glass were used as the light source and the absorption of a spin-coated P3HT film on glass was measured initially using a PMT PD. In a subsequent extension of this work, a near UV 4,4′-bis(9-carbazolyl)-1,1′-biphenyl (CBP)-based combinatorial array of μcOLED pixels was fabricated by varying the thickness of the organic layers to obtain nine sharp, discrete emission peaks from 370 to 430 nm.[77] This array was employed in an all-organic on-chip spectrometer.[77] Detailed experimental results of this work are discussed in chapter 5. Recapping, the current near UV array expands the range of the on-chip spectrophotometer described by Liu et al. from the visible to shorter wavelengths.

www.manaraa.com

4.4. Examples of Potential Challenges in Sensing with OPDs

4.4.1. Signal to noise ratio

As mentioned, several promising approaches to increase the SNR of PL-based sensors were reported, however, there is still a significant barrier to achieve a low LOD. Banerjee and coworkers analyzed some of the parameters that affect the LOD [90] with the same setup they used previously [64] but with an Alq_3-based green OLED, rather than a collimated metal halide lamp, as the excitation source. They repeated the detection of rhodamine 6G and demonstrated the effect of the depth of the microfluidic channel, the responsivity of the OPD, and the pump light power on the LOD. The SNR was theoretically shown to be maximized by suppressing the OPD's dark current that originates from the leakage EL of the excitation source and the autofluorescence from the microfluidic channel material, by using monolithic integration of the detection system for better fluorescence collection efficiency by the OPD and less leakage through the substrate. The experimental results show excellent agreement with a proposed theoretical model in terms of these three parameters. Analysis of the model shows ways to improve the SNR, thereby lowering the LOD. They report 1 nM limit of detection of rhodamine 6G with a possibility of achieving even a pM detection level. **Figure 4.11** shows the dependence of S/B (i.e., the signal minus the background normalized to the latter) on the OPD responsivity.

www.manaraa.com

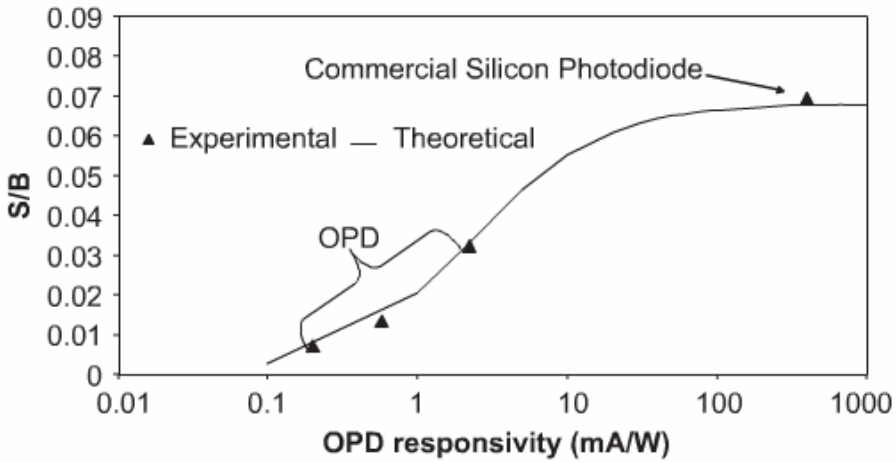

Figure 4.11: Variation of S/B with OPD responsivity. Measurements were conducted using 1mM of Rhodamine 6G, OLED/OPD with 0.1mA/W responsivity and 50 μm channel height with lock-in output, 5 V drive and 0.035 mA/W responsivity, and lock-in-input for 50 μm channel respectively. Reprinted from reference [90]; copyright 2010, with permission from Elsevier B.V.

As mentioned, another major criterion for achieving low LOD is to have very low dark current under reverse bias. Typically, low dark current densities are attained by either using a thicker active layer [20] or by using additional electron or hole blocking layers between the active layers and the electrodes. [91-92] The tuning of the electrode work function, by introducing a thin layer of a dielectric polymer, can also be employed to reduce the dark current via suppressing undesired carrier injection from the electrode to the active layer. [93] As an example, although a small negative bias on the OPD often improves its performance, we observed [74] that the dark current was the lowest at a level of 1 nA/cm^2 at 0 bias, and, indeed, a bias of -0.5 V deteriorated the LOD.

4.4.2. Stability

As discussed via examples throughout the text, stability of OPDs, including hybrid PDs, remains an issue. Stability of OPDs, however, is not as crucial as stability of organic solar cells, as the demand for disposable sensors is growing and sensor probes are also often disposable. Additionally, disposability of OPDs and hybrid PDs is not expected to be

www.manaraa.com

a major problem due to potential future low cost of such devices. Moreover, encapsulation approaches to minimize adverse effects of moisture and O_2 are available as was developed for OLEDs, [94-96] which will extend the operational lifetime of the OPDs. Short wavelength irradiation is known to adversely affect solar cells, [97] though this is less of an issue for OPDs that are typically exposed to lower intensity longer wavelengths.

4.4.3. Time resolved sensing with OPDs

For time resolved sensing, short rise and fall times of the detector's response are crucial. The decay time of phosphorescent indicators is typically in the μs range; the response time of the OPD should therefore be shorter than 1 μs. The response time strongly depends on material and geometric parameters. It was shown that it can be lowered by multilayer architectures and/or by reverse (negative) DC biasing of the OPDs. [98]

It is interesting to note that an OLED-based O_2 sensor with a thin film amorphous or nanocrystalline Si-based PD did not enable monitoring O_2 in the time domain likely due to the presence of deep traps in the bulk of the material or at grain boundaries. [99] OPDs, in contrast, allowed such measurements. [74,75]

Peumans et al. [98] showed that the response time of an OPD can be shorter than 1 ns using ultrathin (~5 Å) multilayer architectures with alternating D/A layers. The photogenerated excitons can then effectively diffuse to the closely spaced D/A interfaces between the CuPc and PTCBI layers, as the interfaces are within the exciton diffusion length (50 Å). The exciton lifetime and dark current through the OPD decreased with the decreasing thickness of alternating CuPc/PTCBI layers, while the reverse bias increased the charge collection at the electrodes via field-induced exciton dissociation and carrier tunneling through the energy barriers between the layers. Interestingly, Azellino and

www.manaraa.com

coworkers [100] reported that the response speed of an inkjet-printed inverted P3HT:$PC_{61}BM$ OPD increases with increasing power (P) of the incident light as at higher P, the slow interface traps are mostly filled compared to the shallow bulk traps in the active layers, influencing exciton lifetime.

4.4.4. Hybrid photodetectors

Recently organolead halide perovskite solar cells have attracted strong attention because of their high charge-carrier mobilities, strong light absorption, high yield quantum conversion, tunable spectral response, and high photo-conversion efficiencies. Moreover, the performance parameters of such PDs are comparable to or better than those reported for organic and vacuum deposited inorganic PDs. [101-106] **Figure 4.12** shows a general structure of a perovskite-based device and its energy diagram. Such devices are based on e.g., $CH_3NH_3PbI_3$ (MAI) with various choices of hole and electron transport layers, as described in the following examples.

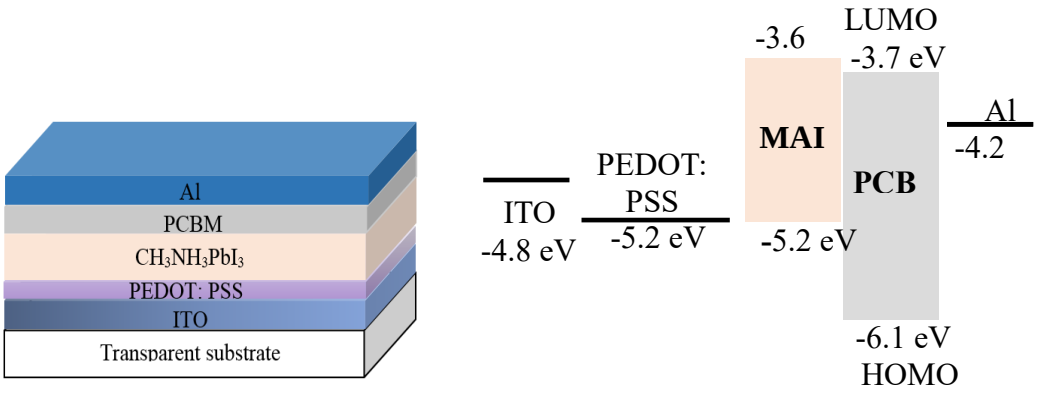

Figure 4.12: Schematic (not to scale) of an example of a perovskite-based device and its energy diagram.

Dou et al. [102] demonstrated a novel solution-processed organic–inorganic hybrid perovskite-based PD operating at room temperature and exhibiting a large detectivity

www.manaraa.com

(~10^{14} Jones). The structure of the PD was ITO/PEDOT:PSS/$CH_3NH_3PbI_{3-x}Cl_x$/PCBM/PFN (poly[(9,9-bis(30-(N,N-dimethylamino)propyl)-2,7-fluorene)-alt-2,7-(9,9-dioctylfluorene)/Al and the reason for the high detectivity was the hole blocking layer PFN between PCBM and the Al cathode. This layer significantly reduced the dark current density to $1.5x10^{-11}mAcm^{-2}$, leading to a high rectification ratio (~10^5) as compared to a PD with no or other hole blocking layers. Moreover, the PD showed a linear dynamic range (LDR), over 100 dB, and a 600 ns response time with a 3 dB bandwidth up to 3 MHz for a 0.01 cm^2 device area.

With a similar approach Fang et al. [107] fabricated a highly sensitive multilayer perovskite PD with low noise (16 fA $Hz^{-1/2}$ at −0.1 V), close to the shot and thermal noise limits. The low noise was due mainly to trap passivation at the interfacial layer by using cross-linked OTPD(N4,N4′-bis(4-(6-((3-ethyloxetan-3-yl)methoxy)hexyl)phenyl)-N4,N4′-diphenylbiphenyl- 4,4′-diamine) as HTL and double fullerene layers (PCBM/C_{60}) as ETL, which enabled the PD to resolve weak light signals of sub-picowatt/cm^2 maintaining a constant responsivity. Additionally, the PD had a high EQE (~90%) with a large LDR of 94 dB and a fast response time (~120 ns).

The performance of perovskite PDs can also be improved by modifying the ITO/perovskite/ P3HT/MoO_3/Ag OPD with a sol–gel processed TiO_2 compact film as an electron extracting layer. [105] For further enhancement the TiO_2 surface was reengineered with solution-processed $PC_{61}BM$ layer. The reduced dark current (~10^{-8} Acm^{-2}) due to the passivation of interfacial layers resulted in a high detectivity of 4×10^{12} cm $Hz^{-1/2}W^{-1}$ over a wide wavelength range (375 to 800 nm) and an EQE of 80%.

www.manaraa.com

The foregoing hybrid perovskite photodetectors also exhibit high photoconductive gain. Dong and coworkers showed that broadband hybrid perovskite PDs can achieve a very high gain (EQE ~500%) with a peak responsivity (i.e., the ratio of the photocurrent to incident power under 1 V negative bias) of 242 AW^{-1} at 740 nm.[108] Xin Hu et al. demonstrated the first broadband high gain photodetector based on a $CH_3NH_3PbI_3$ film deposited on a flexible ITO-coated substrate employing photoconduction under UV light. [103] The perovskite PD was found to be sensitive to a broad wavelength range from the UV to the visible, showing a photoresponsivity (defined here as the change in the photocurrent normalized to the irradiance and the device area) of 3.49 AW^{-1} and an EQE of 1.19×10^3% at 365 nm under a reverse bias of 3 V. Additionally, the PD exhibited faster response time (<0.1 μs) in comparison to other flexible PDs [109-110] and an excellent electrical stability under external bending.

Despite having excellent characteristics as PDs, perovskite materials suffer from degradation in air and moisture. [111-112] Guo et al. addressed the poor performance due to the well-known instability in air and showed an effective and solution-processable passivation of the perovskite that is transparent to UV light. [113] The authors reported a $CH_3NH_3PbI_{3-x}Cl_x$-based PD encapsulated by a spin-coated, water-resistant fluorous polymer (CYTOP). In addition to being highly sensitive to a broadband emission, including UV, and having a sub-μs response time, this hybrid PD maintained 75% of its initial performance after 100 days in air. The stability and durability of this device was demonstrated also by showing the insignificant change in photocurrent of the CYTOP-encapsulated perovskite PD under 8.1 mW/cm^2 irradiation at 50ºC (and 50-60% relative humidity) for over 100 h.

www.manaraa.com

The foregoing PDs may be developed for practical applications in analytical sensing due to their broadband spectral response, high sensitivity, fast response, and low cost solution processing. We note that narrow band PDs are sometimes needed to avoid interfering excitation or other background light.

Tables A2.1 and A2.2 in the appendix A2 summarize the reported OPDs attributes and their analytical applications. Attributes of some other non-organic PDs are also provided for comparison. Comparison to detection with a PMT is also included in Table A2.2. We note that not all parameters/attributes are included in the Tables as they are not provided in the cited literature.

4.5. Concluding Remarks and Outlook

Compact optical bio/chem sensors have a potential to be used widely for point-of-care analyses, environmental monitoring, food safety, clinical and biological assays, and security. This review highlighted some examples of successful use of organic thin film PDs as well as challenges faced in all-organic analytical devices, such as sensors and on-chip spectrometers. OPDs show good detection sensitivities and fast responses, and together with their potential low cost, flexibility of size and design, and possibility of fabrication on flexible as well as wearable substrates, they are promising as field deployable, disposable analytical tools.

There are ongoing challenges in developing all organic optical devices for analytical applications. The LOD should be improved and in some cases OPDs with specific, narrow band response (to eliminate background light), rather than broadband response, are needed. Stability is an ongoing issue, though it is not as important as in solar cells, as a demand for disposable sensors is growing. Due to the potential large selection of organic and organic-

www.manaraa.com

inorganic hybrid semiconductors, PDs with specific spectral response will likely be developed and the ability to fabricate micron-size devices and dense arrays will enhance their use in bioelectronics R&D in general.

4.6. Acknowledgement

Ames Laboratory is operated by Iowa State University for the US Department of Energy (USDOE) under Contract No. DE-AC 02-07CH11358. The research was partially supported by Basic Energy Sciences, Division of Materials Science and Engineering, USDOE.

4.7. References

[1] Sensors trends 2014, V. Großer, D. Heydenbluth, R. Moos, D. Rein, J. Sauerer, C. T. Simmons, W. Sinn, R. Werthschützky, J. Wilde, Eds.; AMA Association for Sensor Technology, Berlin, Germany, 2010.

[2] J. Shinar, R. Shinar, *J. Phys. D: Appl. Phys.* **41,** 133001 (2008)

[3] X. D. Wang, O. S. Wolfbeis, O. S. *Chem. Soc. Rev.* **43**, 3666 (2014)

[4] G. Williams, C. Backhouse, H. Aziz, *Electronics* **3**, 43, (2014)

[5] K. N. Ren, Q. L. Liang, B. Yao, G. O. Luo, L. D. Wang, Y. Gao, Y. M. Wang, Y. Qiu, *Lab Chip* **7**, 1574 (2007)

[6] B. Yao, H. Yang, Q. Liang, G. Luo, L. Wang, K. Ren, Y. Gao, Y. Wang, Y. Qiu, *Anal. Chem.* **78**, 5845 (2006).

[7] B. Choudhury, R. Shinar, J. Shinar, *J. Appl. Phys.* **96**, 2949 (2004).

[8] R. Liu, Y. Cai, J.-M. Park, K.-M. Ho, K.-M.; J. Shinar, R. Shinar, *Adv. Funct. Mater.* **21**, 4744 (2011)

[9] O. S. Wolfbeis, H. Offenbacher, H. Kroneis, H. Marsoner, *Microchim. Acta* **82**, 153 (1984).

[10] Y. You, S. Y. Park, *Adv. Mater.* **20**, 3820 (2008).

[11] C. McDonagh, B. D. MacCraith, A. K. McEvoy, *Anal. Chem.*, **70**, 45 (1998).

www.manaraa.com

[12] Y. Cai, R. Shinar, Z. Zhou, J. Shinar, *Sens. Act. B* **2008**, *134*, 727.

[13] G. Yu, K. Pakbaz, A. J. Heeger, *Appl. Phys. Lett.* **64,** 3422 (1994).

[14] S. Forrest, *Nature* **28**, 911 (2004).

[15] F. C. Krebs, *Sol. Energy Mater. Sol. Cells* **93**, 394 (2009).

[16] P. Peumans, S. Uchida, S. R. Forrest, *Nature* **425,** 158 (2003).

[17] D. Baierl, B. Fabel, P. Lugli, G. Scarpa, *Org. Electron.* **12,** 1669 (2011)

[18] A. Abdellah, B. Fabel, P. Lugli, G. Scarpa, *Org. Electron.* **11,** 1031 (2010).

[19] T. Aernouts, T. Aleksandrov, C. Girotto, J. Genoe, J. Poortmans, *Appl. Phys. Lett.* **92,** 033306 (2008).

[20] T. N. Ng, W. S. Wong, M. L. Chabinyc, S. Sambandan, R. A. Street, *Appl. Phys. Lett.* **92**, 213303 (2008).

[21] K. H. An, B. O'Connor, K. Pipe, M. Shtein, *Org. Electron.* **10,** 1152 (2009).

[22] K. Tvingstedt, D. S. Zilio, O. Inganäs, M. Tormen, *Opt. Express* **16**, 21609 (2008).

[23] K. Zhu, N. R. Neale, A. Miedaner, A. J. Frank, *Nano Lett.* **7**, 69 (2007).

[24] P. Peumans, V. Bulović, S. R. Forrest, *Appl. Phys. Lett.* **76**, 2650 (2000).

[25] D. Duche, P. Torchio, L. Escoubas, F. Monestier, J.-J. Simon, F. Flory, G. Mathian, *Sol. Energy Mater. Sol. Cells* **93**, 1377 (2009).

[26] S. H. Park, A. Roy, S. Beaupre´, S. Cho, S; N. Coates, J. S. Moon, D. Moses, M. Leclerc, K. Lee, A. J. Heeger, *Nat. Photonics* **3**, 297 (2009).

[27] S. Günes, H. Neugebauer, N. S. Sariciftci, *Chem. Rev.* **107**, 1324 (2007).

[28] F. Guo, Z. Xiao, J. Huang, *Adv. Optical Mater.* **1**, 289 (2013).

[29] L. J. Blum, C. A. Marquette, Chemiluminescence-based sensors. In *Optical Chemical Sensors*. F. Baldini, A. N. Chester, J. Homola, S. Martellucci, Eds.; *Springer Science & Business Media*: Dordrecht, The Netherlands, 157 (2006).

[30] A. Juris, V. Balzani, F. Barigelletti, S. Campagna, *Coord. Chem. Rev.* **84**, 85 (1988).

[31] B. G. Flecha, S. Llesuy, A. Boveris, *Free Radical Biol. Med.* **10,** 93 (1991).

[32] K. W. Sigvardson, J. M. Kennish, J. W. Birks, *Anal. Chem.* **56**, 1096 (1984).

[33] R. C. Allen, L. D. Loose, *Biochem. Biophys. Res. Commun.* **69**, 245 (1976).

www.manaraa.com

[34] A. Boveris, E. Cadenas, B. Chance, *Fed. Proc.* **40,** 195 (1981).

[35] R. S. Braman, S. A. Hendrix, *Anal. Chem.* **61**, 2715 (1989).

[36] N. Hanaoka, H. Tanaka, A. Nakamoto, M. Takada, *Anal. Chem.* **63,** 2680 (1991).

[37] K. N. Andrew, M. G. Sanders, S. Forbes, P. J. Worsfold, *Anal. Chim. Acta* **346**, 113 (1997).

[38] M. Amatatongchai, O. Hofmann, D. Nacapricha, O. Chailapakul, A. J. deMello, *Anal. Bioanal. Chem.* **387**, 277 (2007).

[39] A. Gachanja, P. Worsfold, *Anal. Chim. Acta* **290**, 226 (1994).

[40] A. W. Knight, G. M. Greenway, E. D. Chesmore, *Anal. Proc.* **32**, 125 (1995).

[41] A. T. Pereira, P. Novo, D. Prazeres, V. Chu, J. P. Conde, *Biomicrofluidics* **5**, 014102 (2011).

[42] O. Hofmann, P. Miller, P. Sullivan, T. S. Jones, J. C. deMello, D. D. C. Bradley, A. J. deMello, *Sens. Actuators, B* **106,** 878 (2005).

[43] A. M. Jorgensen, K. B. Mogensen, J. P. Kutter, O. Geschke, *Sens. Actuators, B* **90**, 15 (2003).

[44] X. Wang, O. Hofmann, R. Das, E. Barrett, A. J. deMello, J. C. deMello, D. Bradley, *Lab Chip* **7**, 58 (2006).

[45] X. Wang, M. Amatatongchai, D. Nacapricha, O. Hofmann, J. C. deMello, D. D. C. Bradley, A. J. deMello, *Sens. Actuators, B* **140**, 643 (2009).

[46] J. Wojciechowski, L. Shriver-Lake, M. Yamaguchi, E. Füreder, R. Pieler, M. Schamesberger, C. Winder, H. Prall, M. Sonnleitner, F. Ligler, *Anal. Chem.* **81,** 3455 (2009).

[47] N. Pires, T. Dong, *Conf. Proc. IEEE Eng. Med. Biol. Soc.* (2013).

[48] K.-G. Lim, M.-R. Choi, H.-B. Kim, J. H. Park, T.-W. Lee, *J. Mater. Chem.* **22**, 25148 (2012).

[49] N. M. Pires, T. Dong, U. Hanke, N. Hoivik, *J. Biomed. Opt.* **18**, 097001 (2013).

[50] N. M. Pires, T. Dong, *IEEE EMBS*, 4470 (2013).

[51] N. M. M. Pires, T. Dong, *Sensors* **13**, 15898 (2013).

[52] C. Honrado, T. Dong, T; *J. Micromech. Microeng.* **24**, 125023 (2014).

[53] N. Pires, T. Dong, *J. Biomed. Opt.* **19**, 030504 (2014).

www.manaraa.com

[54] N. Pires, T. Dong, *IEEE Eng. Med. Biol. Soc.* 4411 (2014).

[55] P. Hartmann, M. J. Leiner, M. E. Lippitsch, *Anal. Chem.* **67**, 88 (1995).

[56] O. S. Wolfbeis, I. Klimant, T. Werner, C. Huber, U. Kosch, C. Krause, G. Neurauter, A. Dürkop, *Sens. Actuators, B* **51,** 17 (1998).

[57] T. C. O'Riordan, D. Buckley, V. Ogurtsov, R. O'Connor, D. B. Papkovsky, *Anal. Biochem.* **278**, 221 (200).

[58] M. J. Sailor, E. C. Wu, *Adv. Funct. Mater.* **19**, 3195 (2009).

[59] R. Shinar, D. Ghosh, B. Choudhury, M. Noack, V.L. Dalal, J. Shinar; *J. Non-Cryst. Solids* **352**, 1995 (2006).

[60] M. Y. Berezin, S. Achilefu, *Chem. Rev.* **110**, 2641 (2010).

[61] H. Kautsky, *Trans. Faraday Soc.* **35**, 216 (1939).

[62] B. Choudhury, R. Shinar, J. Shinar, *Proc. SPIE* **5214**, 64 (2004).

[63] R. Shinar, B. Choudhury, Z. Zhou, H.-S. Wu, L. B. Tabatabai, J. Shinar, *Proc. SPIE* **5588**, 5588, 59 (2004).

[64] A. Banerjee, A, Pais, I. Papautsky, D. Klotzkin, *IEEE Sensors J.* **8**, 621 (2008).

[65] A. Pais, A, Banerjee, D. Klotzkin, I. Papautsky, *Lab Chip* **8**, 794 (2008).

[66] Y. Shuai, A. Banerjee, D. Klotzkin, I. Papautsky, *Proc. IEEE Sensors* (2008).

[67] A. Banerjee, Y. Shuai, D. Klotzkin, I. Papautsky, *IEEE* 177 (2008).

[68] E. Kraker, A. Haase, B. Lamprecht, G. Jakopic, C. Konrad, S. Köstler, *Appl. Phys. Lett.* **92**, 033302 (2008).

[69] T. Mayr, T. Abel, E. Kraker, S. Köstler, A. Haase, C. Konrad, M. Tscherner, B. Lamprecht, *Procedia Eng.* **5**, 1005 (2010).

[70] T. Abel, M. Sagmeister, B. Lamprecht, E. Kraker, S. Köstler, B. Ungerböck, T. Mayr, *Anal. Bioanal. Chem.* **404**, 2841 (2012).

[71] B. Lamprecht, M. Sagmeister, E. Kraker, P. Hartmann, G. Jakopic, S. Köstler, H. Ditlbacher, N. Galler, J. Krenn, B. Ungerböck, T. Abel, T. Mayr, *Proc. SPIE* **8234**, 82341H-1 (2012).

[72] M. Sagmeister, B. Lamprecht, E. Kraker, A. Haase, G. Jakopic, S. Köstler, H. Ditlbacher, N. Galler, T. Abel, T. Mayr, *Proc. SPIE* **8118**, 811805-1 (2011).

www.manaraa.com

[73] M. Sagmeister, A. Tschepp, E. Kraker, T. Abel, B. Lamprecht, T. Mayr, S. Köstler, *Anal. Bioanal. Chem.* **405**, 5975 (2013).

[74] K. S. Nalwa, Y. Cai, A. L. Thoeming, J. Shinar, R. Shinar, S. Chaudhary, *Adv. Mater.* **22**, 4157 (2010).

[75] R. Liu, T. Xiao, W. Cui, J. Shinar, R. Shinar, *Anal. Chim. Acta* **778**, 70 (2013).

[76] R. Liu, Z. Gan, R. Shinar, J. Shinar, *Phys. Rev. B* **83**, 245302 (2011).

[77] E. Manna, F. Fungura, R. Biswas, J. Shinar, R. Shinar, *Adv. Funct. Mater.* **25**, 1226 (2015).

[78] F. Lefèvre, A. Chalifour, L. Yu, V. Chodavarapu, P. Juneau, R. Izquierdo, *Lab Chip* **12**, 787 (2012).

[79] G. Ryu, J. Huang, O. Hofmann, C. A. Walshe, J. Y. Sze, G. D. McClean, A. Mosley, S. J. Rattle, D. D. Bradley, *Lab Chip* **11**, 1664 (2011).

[80] M. Miyake, H. Nakajima, A. Hemmi, M. Yahiro, C. Adachi, N. Soh, R. Ishimatsu, K. Nakano, K. Uchiyama, T. Imato, *Talanta* **96**, 132 (2012).

[81] R. Ishimatsu, A. Naruse, R. Liu, K. Nakano, M. Yahiro, C. Adachi, T. Imato, *Talanta* **117**, 139 (2013).

[82] R. Liu, R. Ishimatsu, M. Yahiro, C. Adachi, K. Nakano, T. Imato, *Talanta* **134**, 37 (2015).

[83] R. Liu, R. Ishimatsu, M. Yahiro, C. Adachi, K. Nakano, T. Imato, *Talanta* **132**, 96 (2015).

[84] B. Lamprecht, A. Tschepp, M. Čajlaković, M. Sagmeister, V. Ribitsch, S. A. Köstler, *Analyst* **138**, 5875 (2013).

[85] V. Charwat, P. Muellner, R. Hainberger, M. Purtscher, P. Ertl, S. Tedde, O. Hayden, *Information Photonics (IP), ICO International Conference on*, 1 (2011).

[86] V. Charwat, M. Purtscher, S. Tedde, O. Hayden, P. Ertl, *Lab Chip* **13**, 785 (2013).

[87] C. M. Lochner, Y. Khan, A. Pierre, A. C. Arias, *Nat. commun.* **5**, 5745 (2014).

[88] M. Ramuz, D. Leuenberger, L. Bürgi, *J. Polym. Sci., Part B: Polym. Phys.* **49**, 80 (2011).

[89] R. Liu, C. Xu, R. Biswas, J. Shinar, R. Shinar, *Appl. Phys. Lett.* **99**, 093305 (2011).

[90] A. Banerjee, Y. Shuai, R. Dixit, I. Papautsky, D. Klotzkin, *J. Lumin.* **130**, 1095 (2010).

www.manaraa.com

[91] P. Keivanidis, S.-H. Khong, P. Ho, N. Greenham, R. Friend, *Appl. Phys. Lett.* **94**, 173303 (2009).

[92] X. Gong, M.-H. Tong, S. Park, M. Liu, A. Jen, A. Heeger, *Sensors* **10**, 6488 (2010).

[93] E. Saracco, B. Bouthinon, J.-M. Verilhac, C. Celle, N. Chevalier, D. Mariolle, O. Dhez, J.-P. Simonato, *Adv. Mater.* **25**, 6534 (2013).

[94] A. P. Ghosh, L. J. Gerenser, C. M. Jarman, J. E. Fornalik, *Appl. Phys. Lett*. **2005**, *86*, 223503

[95] J.-S. Park, H. Chae, H. K. Chung, S. I. Lee, *Semicond. Sci. Technol*. **26**, 034001 (2011).

[96] J. Ahmad, K. Bazaka, L. J. Anderson, R. D. White, M. V. Jacob, *Renewable Sustainable Energy Rev*. **27**, 104 (2013).

[97] M. Jørgensen, K. Norrman, F. C. Krebs, *Sol. Energ. Mat. Sol. C.*, **92**, 686 (2008).

[98] P. Peumans, V. Bulović, S. R. Forrest, *Appl. Phys. Lett.*, **76**, 3855 (2000).

[99] D. Ghosh, R. Shinar, V. Dalal, Z. Zhou, J. Shinar, *J. Non-Cryst. Solids* **354**, 2606 (2008).

[100] G. Azzellino, A. Grimoldi, M. Binda, M. Caironi, D. Natali, M. Sampietro, *Adv. Mater.* **25**, 6829 (2013).

[101] T. Miyasaka, *Chem. Lett.* **44**, 720 (2015).

[102] L. Dou, Y. M. Yang, J. You, Z. Hong, W. H. Chang, G. Li, Y. Yang, *Nat. Commun.* **5,** 5404 (2014).

[103] X. Hu, X. Zhang, L. Liang, J. Bao, S. Li, W. Yang, Y. Xie, *Adv. Funct. Mater.* **24**, 7373 (2014).

[104] Y. Lee, J. Kwon, E. Hwang, C. H. Ra, W. J. Yoo, J. H. Ahn, J. H. Park, J. H. Cho, *Adv. Mater.* **27**, 41 (2015).

[105] C. Liu, K. Wang, C. Yi, X. Shi, P. Du, A. W. Smith, A. Karim, X. Gong, *J. Mater. Chem. C*, **3,** 6600 (2015)**.**

[106] Z. Xiao, Y. Yuan, Y. Shao, Q. Wang, Q. Dong, C. Bi, P. Sharma, A. Gruverman, J. Huang, *Nat. Mat.* **14**, 193 (2015).

[107] Y. Fang, J. Huang, *Adv. Mater.* **27**, 2804 (2015).

[108] R. Dong, Y. Fang, J. Chae, J. Dai, Z. Xiao, Q. Dong, Y. Yuan, A. Centrone, X. C. Zeng, J. Huang, *Adv. Mater.* **27**, 1912 (2015).

www.manaraa.com

[109] F. X. Wang, J. Lin, W. B. Gu, Y. Q. Liu, H. D. Wu, G. B. Pan, *Chem. Commun.* **49**, 2433 (2013).

[110] G. Chen, Z. Liu, B. Liang, G. Yu, Z. Xie, H. T. Huang, B. Liu, X. F. Wang, D. Chen, M. Q. Zhu, G. Z. Shen, *Adv. Funct. Mater.* **23**, 2681 (2013).

[111] R. K. Misra, S. Aharon, B. Li, D. Mogilyansky, I. Visoly-Fisher, L. Etgar, E. A. Katz, *J. Phys. Chem. Lett.* **6**, 326 (2015).

[112] G. Niu, W. Li, F. Meng, L. Wang, H. Dong, Y. Qiu, *J. Mater. Chem. A*, **2**, 705 (2014).

[113] Y. Guo, C. Liu, H. Tanaka, E. Nakamura, *J. Phys. Chem. Lett.* **6**, 535 (2015).

[114] Dhar, S; Miller, D. M; Jokerst, N. M; *Opt. Express*. **22,** 5052 (2012)

[115] T. Kamei, B. M. Paegel, J. R. Scherer, A. M. Skelley, R. A. Street, R. A. Mathies, *Anal. Chem.* **75,** 5300 (2003).

[116] A. Joskowiak, M. S. Santos, D. M. F. Prazeres, V. Chua, J. P. Condea, *Sens. Act. B* **156**, 662 (2011).

[117] A. Samusenko, V. J. Hamedan, G. Pucker, M. Ghulinyan, F. Ficorella, R. Guider, D. Gandolfi, L. Pavesi, *Proc. of SPIE* **9520**, 95200D-1 (2015).

[118] J. P. Clifford, G. Konstantatos, K. W. Johnston, S. Hoogland, L. Levina, E. H. Sargen, *Nat. Nanotechnol.* **4**, 40 (2009).

[119] D. Caputo, G. de Cesare, L. S. Dolci, M. Mirasoli, A. Nascetti, A. Roda, R. Scipinotti, *IEEE Sens. J.* **13**, 2595 (2013).

[120] C. C. Lin, F. H. Ko, C. C. Chen, Y. S. Yang, F. C. Chang, C. S. Wu, *Electrophoresis* **30**, 3189 (2009).

www.manaraa.com

CHAPTER 5

TUNABLE NEAR UV MICROCAVITY OLEDS AND MULTICOLOR OLED ARRAYS: CHARACTERIZATION AND ANALYTICAL APPLICATIONS

Modified from E. Manna, F. Fungura, R. Biswas, J. Shinar, R. Shinar,
Adv. Funct. Mater. **25**, 1226 (2015)

Abstract

We demonstrate a new, as yet unexplored, approach to fabricate narrow-band emission near-UV microcavity OLEDs (μcOLEDs) with peak emission at ~385 nm, in near-perfect alignment with the narrow primary 385 nm absorption band of the ubiquitous Pt octaethyl porphyrin (PtOEP) dye, using 4,4'-N,N'-dicarbazole-biphenyl (CBP) as the emissive layer. Although OLEDs have been extensively operated at optical wavelengths, only few have achieved near-UV emission, as described in this paper. Yet there is a growing need for portable compact narrow-band near UV sources for many biomedical and forensic applications. A microcavity effect, due to metallic electrodes enclosing an optical cavity, was employed to achieve the desired narrow peak emission. An Al/Pd bi-layer anode enabled attaining a turn on voltage of 3.8 V – only 0.58 V more than the 385 nm photon energy – and a 4,4′-cyclohexylidenebis [N, N-bis (4-methylphenyl) benzenamine] (TAPC) layer improved electron-hole recombination in the emissive layer. The fabricated μcOLED was efficiently used as the excitation source in a structurally integrated all-organic oxygen sensor. Moreover, a CBP-based combinatorial array of μcOLED pixels was fabricated by varying the thickness of the organic layers to obtain nine sharp, discrete emission peaks from 370 to 430 nm, which were employed in an all-organic on-chip spectrophotometer. The photodetectors were based on P3HT:PCBM (poly(3-hexylthiophene):[6,6]-phenyl-

www.manaraa.com

C_{60}-butyric acid methyl ester) or the more sensitive PTB7:PCBM (PTB7 is polythieno [3,4-b]-thiophene-co-benzodithiophene). Simulations of the OLEDs' emission, performed with a scattering matrix approach and in good agreement with the experimental results, were used for analysis of the experimental data, assisting in device fabrication.

Key Words: UV OLED, microcavity OLED, oxygen sensing, photoluminescence enhancement, on-chip spectrophotometer

5.1. Introduction

Organic light emitting diodes' (OLEDs') attributes include many promising features such as compatibility with simple and flexible substrates[1-5] and easily adaptable size and design.[6-7] As such, they are uniquely simple to integrate with other components to generate compact devices for optical analytical applications.[3-4,8-12] Indeed, the unique characteristics of OLEDs resulted in their incorporation in various sensing schemes.[13-18] As an example, OLEDs were used as excitation sources in optical gas and liquid phase (bio)chemical sensors, including O_2 sensors.[3,8-12,19] The latter play a crucial role in e.g., food packaging, medical testing, and biological applications, including cell cultivation, marine biology, and enzymatic biosensing.[20-22] OLEDs, together with organic photodetectors (OPDs), address a growing need for more compact, field-deployable integrated devices, though challenges associated with such all-organic platforms still exist.[3,13]

In attempts to improve OLEDs for solid-state lighting and display applications, devices with many different configurations were explored.[23,24] The focus of OLED R&D, however, has been mainly on devices emitting in the visible range.[24] Significantly less research has been aimed at developing efficient OLEDs emitting in the near UV or near IR regions.[25-27] Yet efficient deep-blue/near UV OLEDs and arrays with pixels emitting at

www.manaraa.com

different wavelengths in this range are of strong interest for analytical applications.[3,10] For these applications, microcavity OLEDs (μcOLEDs) are advantageous as the otherwise broad electroluminescence (EL) band of the OLED[3] narrows and can be tailored to a desired peak emission wavelength λ_{max} by tuning the cavity modes.[28-30] Moreover, the sharper OLED emission bands minimize interference with the photoluminescence (PL) of sensing probes. In addition, the microcavity structure allows fabrication of a combinatorial array of OLED pixels with tunable narrower emission bands on a common, small-size substrate,[30] which can be adapted as an on-chip spectrometer and for simultaneous detection of multiple analytes.

The optical O_2 sensor comprises three major components: the excitation source, the sensor film, and the photodetector (PD). Sensing is based on monitoring the PL whose intensity and decay time depends on the dose of the quenching element.[3,8-12] PL quenching occurs via O_2-dye collisions in a dynamic process;[31] ideally it is described by the Stern-Volmer (SV) equation[3,8-11]

$$\frac{I_0}{I} = \frac{\tau_0}{\tau} = 1 + Ksv[O_2] \qquad 5.1$$

Where I_0 and τ_0 are the PL intensity and decay time, respectively, at 0% oxygen, and I and τ are the values in the presence of oxygen. K_{SV} is the SV constant. The sensitivity S is defined as τ_0/τ(100% O_2) or I_0/I(100% O_2).

Several approaches have been developed to increase the sensitivity of the sensor as well as the PL intensity. Pt octaethylporphyrin (PtOEP) embedded in a polystyrene (PS) matrix is often used, but PS is only moderately permeable to oxygen.[3] Studies show that polyethylene glycol (PEG) blended with PS (PEG:PS) at ratios of 1:9 to 1:4 and

www.manaraa.com

PtOEP:PEG:PS sensing films enhance OLED outcoupling and the PL intensity, respectively.[8,32]

In this work novel near UV 4,4'-bis(9-carbazolyl)biphenyl (CBP)-based μcOLEDs were fabricated by using, inter alia, Al/Pd cathodes, and they were successfully used for improved O_2 sensing. Additionally, a combinatorial array of tunable CBP-based μcOLEDs emitting in the 370-430 nm range was used in an on-chip spectrometer. The O_2 sensor was a structurally integrated all-organic OLED/sensing film/OPD device. The OLED's peak emission was tuned to 385 nm, where the PtOEP has a strong absorption peak.[33] The sensing film was a PtOEP:PEG:PS blend; it was drop cast on the back side of the OLED's glass substrate. The OPD, in the front detection configuration,[3,8] was based on the standard P3HT:PCBM (where P3HT is poly(3-hexyl thiophene) and PCBM is phenyl-C_{61}-butyric acid methyl ester) or a more sensitive one, which was based on polythieno [3,4-b]-thiophene-co-benzodithiophene (PTB7). The choice of the μcOLED eliminates the issue related to the OLED's EL tail that is otherwise detected by the OPD, generating an interfering background. The blend sensing film results in enhanced PL signals.[8] The utility of the combinatorial array of the OLED pixels is demonstrated by using it to measure the absorbance spectrum of an Alexa Fluor 405 film. The 370 – 430 nm range presented here is a step toward expansion of the range covered by μcOLED pixels emitting in the 493 – 639 nm visible range,[30] and the integration with an OPD, first undertaken here for the on-chip OLED-based spectrometer, presents a step toward achieving a compact, economical spectrometer.

Simulations of emission from OLEDs, which assisted in device design, were performed with our scattering matrix approach, described previously.[34]

www.manaraa.com

5.2.Results and Discussions

5.2.1. µC OLED design

Due to strong optical absorption by ITO[35] and most common metals in the UV, the standard near-UV OLED and the µcOLEDs, where a very thin metal layer is used as the semitransparent anode, have a high loss at the electrode/organic interface, which results in reduced device efficiency. Thin Ag metal has been extensively used as a semi-transparent anode in µcOLEDs emitting in the visible because its high reflectance and low absorption in that region provide a very good lossless microcavity.[28,30,36] However below 400 nm, the absorption of silver increases rapidly and its reflectance decreases.[37-38] Despite being lossy, Al is well suited for fabricating a strong optical near UV microcavity due to its uniform reflectance in this wavelength range. **Figure 5.1** shows the irradiance *R* vs. voltage for CBP-based standard and µcOLEDs of the structure anode/MoO_x (5 nm)/CBP (25 nm)/BPhen (35 nm)/LiF/Al with three different anodes: ~140 nm ITO,[11] 25 nm Ag, and 15 nm Al.

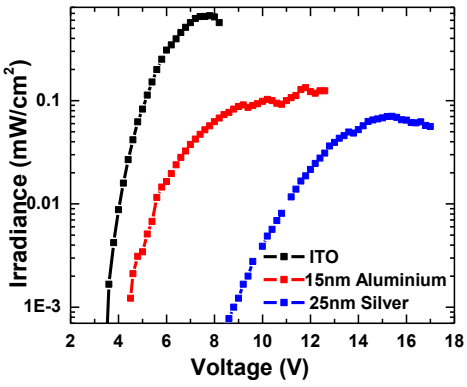

Figure 5.1: Irradiance (R) vs V for UV CBP OLEDs with ITO, Ag, or Al anodes

One of this work's goals was to obtain an easy-to-fabricate anode that provides a good microcavity and a low turn on voltage for the near-UV OLED. The work function of Al is

www.manaraa.com

~-4 – -4.2 eV, so to improve hole injection, a very thin layer of palladium was added. Adding just 5 nm of Pd on top of the Al anode improves the hole injection due to Pd's deeper Fermi level (~-5.2 - -5.6 eV) without significantly affecting the EL full width at half maximum (FWHM), which is 25 nm, with the EL peak red-shifting by ~5 nm (from 382 to 387 nm). The addition of the Pd layer also prevents the formation of a thin insulating Al oxide layer. **Figure 5.2** compares *R* and current density (*J*) vs voltage for devices with Al vs Al/Pd anodes.

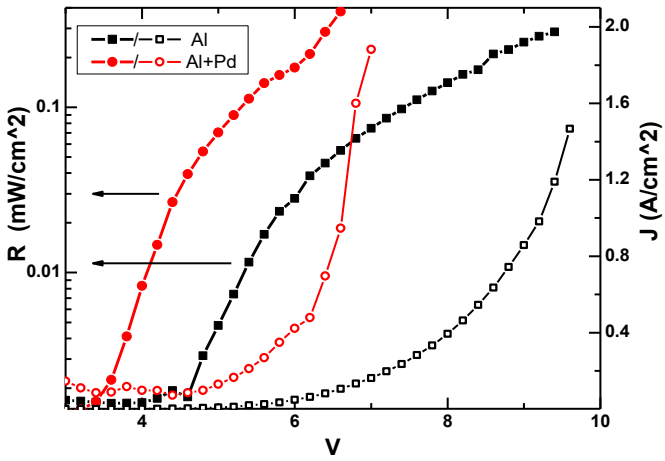

Figure 5.2: *R and J vs V for µcOLEDs with Al or bi-layer Al/Pd anodes with the structure anode/MoO_x (5 nm)/CBP (25 nm)/BPhen (35 nm)/LiF/Al.*

In the µcOLEDs, the thickness of the MoO_x layer is not sufficient to prevent exciton quenching by the metal anode. Additionally, though CBP has a relatively high electron mobility μ_e ~ $3x10^{-4}$ $cm^2/V{\cdot}s$, it is still much lower than the hole mobility μ_h ~ $2x10^{-3}$ $cm^2/V{\cdot}s$, so charge balance in the device needs improvement. Device performance indeed improved when we added a 20 nm 4, 4′-cyclohexylidenebis [N, N-bis (4-methylphenyl) benzenamine] (TAPC) layer on the MoO_x, where the anode was Al, and 30 nm (optimized thickness) of TAPC for the device with the ITO anode. The improvement is likely due to

www.manaraa.com

reduced exciton quenching at the anode in the microcavity device and excellent electron and exciton blocking due to TAPC's shallow LUMO level (~-2.0 eV). **Figure 5.3** shows the *J-R-V* characteristics of µcOLEDs with and without TAPC as a hole transporting layer (HTL), as well as the energy level diagram of the devices. The external quantum efficiency (EQE) without the TAPC layer is very low. In contrast, the EQE of the devices with TAPC is about 0.2%, which is comparable to previous reports on conventional UV OLEDs.[25,27] The charge imbalance in the device may be associated with the higher hole mobility of CBP (x10 larger than the electron mobility), which can result in accumulation of holes near the CBP/BPhen interface in the absence of TAPC. This charge accumulation likely quenches excitons formed near that interface.[39] Adding a TAPC layer may reduce the exciton quenching by improving charge balance in the device.

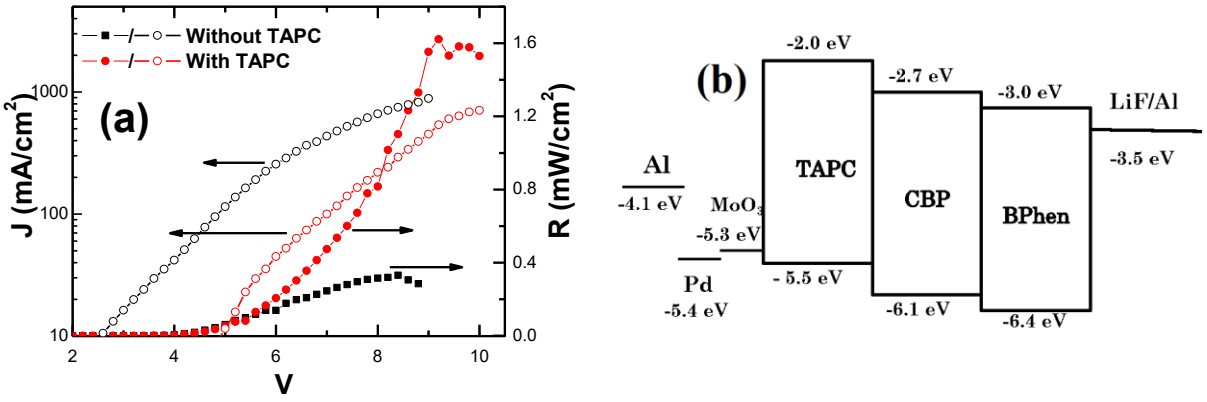

Figure 5.3: (a) J-R-V curves of OLEDs with and without a TAPC hole-transport layer. (b) The energy level diagram of the device.

We note that the reduced current with added TAPC stems from an increase in the resistance, which increased with increasing TAPC thickness.

www.manaraa.com

5.2.2. Gas phase oxygen sensing

Four different PtOEP-doped sensing films were evaluated for achieving the largest PL intensity and sensitivity first with a photomultiplier tube (PMT) in a back detection configuration. The four sensing films are low *Mw* PS (45,000), high *Mw* PS (288,000), 1:9 PEG:high *Mw* PS, and 1:4 PEG:high *Mw* PS. **Figure 5.4** shows the PL decay signal for each sensing film following application of a 1 ms voltage pulse to the OLED excitation source. As seen, the PtOEP-doped 1:9 PEG:PS film shows the highest PL intensity. Figure 4 shows also the largely linear SV plots of τ_0/τ vs $[O_2]$ with R^2 values of 0.991, 0.987, 0.983, and 0.998, respectively. The 1:9 PEG:PS film shows the best performance with the highest PL intensity and detection sensitivity S = 20.4. The results are in good agreement with the OLED outcoupling and PL intensity enhancement reported by Liu et al.[8,32] The scattering centers on the surface and in the bulk of the 1:9 PEG:PS film increase light absorption and hence the PL.[8] Moreover, the dye-O_2 interaction is likely increased due to the increased surface area of the sensing film, which increases S.

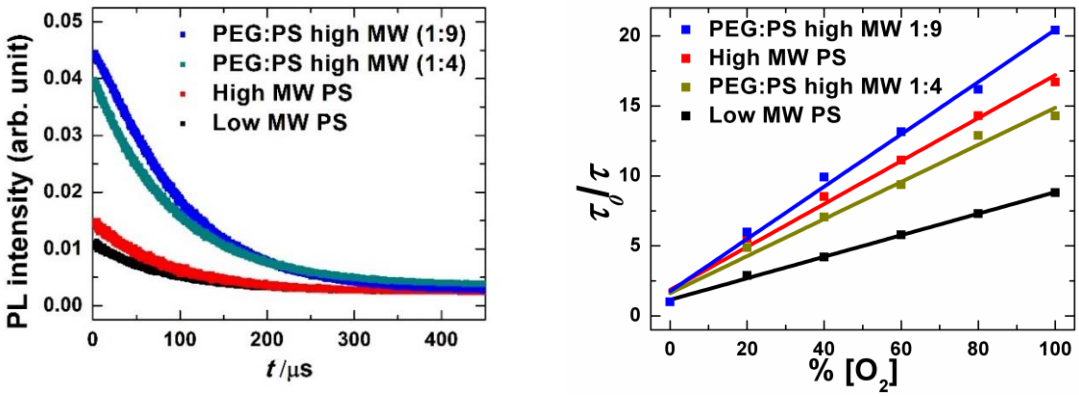

Figure 5.4: PL decay curves at 0% O_2 (left) and SV plots (right) with pulsed OLED excitation using different sensing films.

www.manaraa.com

5.2.3. Integration with a photodetector

Standard and microcavity green tris(8-hydroxy quinoline) Al (Alq_3)-based OLEDs (~530 nm peak emission) were used successfully for O_2 and related sensing applications.[8-11] However, when replacing the PMT with an integrated OPD, the [O_2] range that can be detected is limited.[8,40] As the absorption of PtOEP (or the Pd analog PdOEP) is stronger in the near UV region (~385-395 nm), a standard near UV[11] or µcOLED can serve as a very efficient excitation source. **Figure 5.5** shows the schematics of the integrated all-organic sensor.

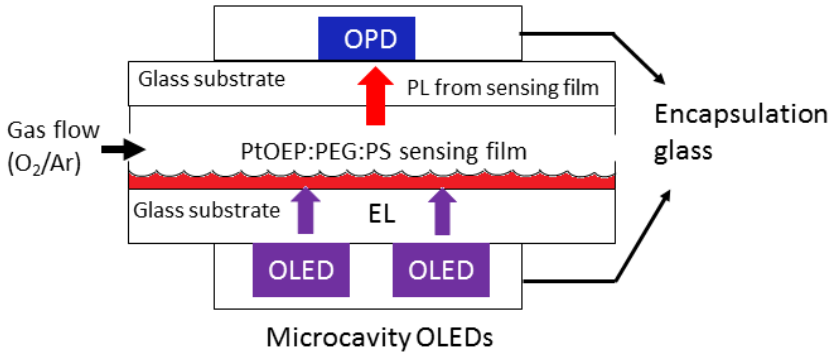

Figure 5.5: Schematics of integrated all-organic sensor (not to scale)

Figure 5.6a shows the SV plots for all-organic O_2 sensors using a PTB7-based OPD with a power conversion efficiency (PCE) of 6.2%. These plots show linear SV relations and the use of the UV µcOLED enabled increased dynamic range with the OPD. We note that with the green µcOLEDs in conjunction with an OPD the signal-to-noise was relatively poor even in the low [O_2] range, unlike the situation with the UV µcOLED. The PTB7-based OPD is preferably chosen for this experiment over the standard P3HT:PCBM-based OPD due to its higher sensitivity in the long wavelength range. **Figure 5.6b** compares the EQE of both OPDs along with the EL of the UV µcOLED and the PL of the sensing film.

www.manaraa.com

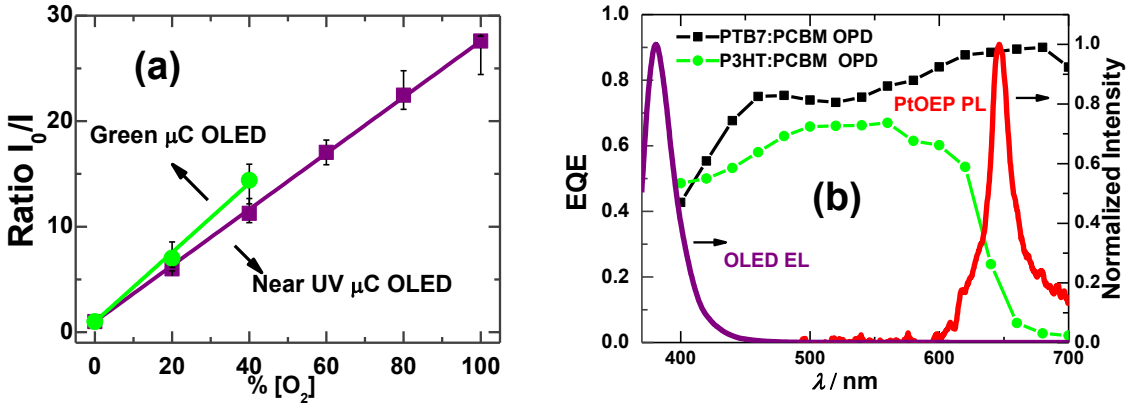

Figure 5.6: (a) SV relation in oxygen sensing with a green (circles) or UV- μcOLED (squares) as the excitation source and PTB7-based OPD with a 6.2% PCE. (b) - EQE of P3HT:PCBM (green circles) and PTB7:PCBM (black squares) OPDs; the EL of the UV μCOLED (violet; ~385 nm), and the normalized PL of the 1:9 PtOEP:PEG:PS sensing film (red; ~645 nm) are also shown.

5.2.4. Near-UV spectrophotometer

5.2.4.1. Measurements:

The resonant wavelength of an optical cavity is described by $m\lambda_r = 2\Sigma n_i(\lambda)L_i\cos\theta$, where λ is the resonant wavelength of the m-th mode, and n_i and L_i are the refractive index and thickness of the i-th layer, respectively. The thickness of the optical medium determines the cavity mode or the normal emission of a μcOLED. Using CBP-based microcavity structures, it was possible to tune the emission wavelength producing nine different discrete and relatively sharp peaks ranging from 370 to 430 nm on a common substrate. The combinatorial array was fabricated by varying the thickness of the CBP and BPhen layers. The structure of the devices was 15 nm Al/5 nm MoO_3/20 nm TAPC/x nm CBP/y nm BPhen/1 nm LiF/Al, where $15 \leq x \leq 30$ nm and $25 \leq y \leq 40$ nm. **Figure 5.7a** shows the EL spectra of these devices. The FWHM of these bands ranged from 24 to 48 nm, with the broadening of the EL spectrum at longer wavelengths due to the shape of the reference (cavity-free) CBP EL spectrum across this wavelength range (Figure 7(a)). All

www.manaraa.com

these devices exhibit comparable *J-R-V* characteristics with $R \sim 0.8$ mW/cm^2 at $J \sim 1$ A/cm^2, except for the thinnest device that showed a slightly reduced *R*.

Figure 5.7b shows the schematics of the all-organic on-chip spectrometer. **Figure 5.7c** shows the absorption spectrum of an Alexa fluor 405 film using this all-organic on-chip spectrometer with the P3HT:PCBM-based OPD. As seen, the measured absorption is in good agreement with that of a reference measurement using the Ocean Optics spectrometer. The current near UV array expands the range of the on-chip spectrophotometer described by Liu et al. from the visible [30] to shorter wavelengths. The Alexa fluor 405 dye was chosen to show the potential of the all-organic on-chip spectrometer in biological applications, as this dye is extensively used in biological fluorescence imaging. The film (~500-750 nm thick) was made from 0.1 mg/mL dye in water. Since the standard concentration of Alexa fluor 405 used in imaging is 0.5 mg/mL,[41] the integrated spectrometer is promising for various future sensing/imaging applications.

5.2.4.2. Simulations

Simulations of the OLEDs' emission were performed with our scattering matrix approach described previously.[34] In this approach Maxwell's equations are solved in Fourier space, i.e., within a plane wave basis for the OLED architecture that contains emissive sources within the OLED. The OLED is composed of layers stacked in the *z* direction. In each layer of the OLED stack, the materials are represented by realistic frequency dependent absorptive dielectric functions obtained from experimental measurements of Al,[42] MoO_x,[43] and ITO.[37] The simulations are performed with all layers being planar in the (*x*, *y*) plane as in the experiment. However this approach is more general allowing the layers to have a periodic structure in the (*x*, *y*) direction with a repeat

www.manaraa.com

vector $\mathbf{R} = n_1\mathbf{a}_1 + n_2\mathbf{a}_2$, where the primitive lattice vectors are $\mathbf{a}_1$ and $\mathbf{a}_2$. This general formalism allows for the investigation of out-coupling of trapped modes using periodic microlens structures or grating structures, which is an important aspect for later work.

ITO-control OLED

We first determined the thickness of the ITO layer on the glass substrates, by measuring the transmission and reflectance of ITO-coated glass and comparing these to simulated reflectance and transmission. The measured transmission exhibited 85-90% transmission over most of the optical spectrum, with a broad peak near 450 nm and a sharp dip at shorter wavelengths, in conjunction with a minimum reflectance near 450 nm, and increasing reflectance at shorter wavelengths. These features were best modeled by an ITO thickness of 110 nm. Larger ITO thicknesses shifted the broad peak position to longer wavelength, whereas thinner ITO moved this peak feature to shorter wavelength. Using this ITO thickness we simulated the emission from the control ITO-based structure composed of glass ITO/MoO_3 (7 nm)/TAPC (20 nm)/CBP (15 nm)/BPhen (25 nm)/LiF (1 nm)/Al. A single wavelength-dependent refractive index $n + ik$ was used for all the organic layers taken from ellipsometry measurements of organic materials,[41] since the optical properties of each individual organic constituent were not available. This approximation may be justified given the small variations expected for n of the individual organic materials. It successfully simulated the measured emission that peaked at 375 nm.

Microcavity OLEDs:

Next we simulated the OLED stack composed of Al (15 nm)/MoO_3 (5 nm)/TAPC (20 nm)/CBP (x nm)/BPhen (y nm)/LiF/Al (100 nm), utilizing available n and k values.[44] We utilized an emissive source at the CBP/BPhen interface. First, the emitted intensity $E_0(\lambda)$ below the glass was simulated assuming the source inside the OLED has a featureless

www.manaraa.com

emission profile. This approach yields the dependence of the emission on the optical cavity length without added assumptions on how the emissive source emits at different wavelengths. Since x and y were varied to tune the microcavity wavelength, we found it convenient to plot the emission peak as a function of the optical length $L = x + y$ (as distinct from the full optical microcavity length, which extends into the bottom and top Al electrodes[30]). The emission intensity exhibits a peak value that increases as the optical cavity length is increased (**Figure 5.7d**). The position of the shortest wavelength emission at 370 nm (x = 15 nm; y = 25 nm, L = 40 nm, the shortest optical length) is in excellent agreement with simulation. The longer optical cavities (L = 60 nm with x = 25 nm, y = 35 nm and L = 65 nm with x = 30 nm, y = 35 nm) also exhibit good agreement of the peak emission wavelengths between experiment and simulation (Figure 7d). Simulations at intermediate L underestimated the positions of the peak wavelengths relative to the experiment. The measurements displayed an almost linear increase of peak wavelengths with L, whereas the simulation showed a more quadratic dependence. As found in our earlier work [30] the complete optical microcavity length must include contributions from the penetration of fields in the Al cathode and anode, and is larger than the simple optical lengths within the electrodes.

The foregoing results suggest that the source CBP emission profile $I_s(\lambda)$ is strongly wavelength dependent. Accordingly, we used the experimentally measured emission $E_{exp}(\lambda)$ and the simulated emission intensity $E_0(\lambda)$ to obtain the emission profile of the emissive CBP species $I_s(\lambda)$ from $E_{exp}(\lambda) = E_0(\lambda)*I_s(\lambda)$. We obtain the source profile $I_s(\lambda)$ to be sharply peaked near 370 nm for short optical lengths (L = 40 nm) and a broad profile with a peak at 425 nm at the longest optical length (L = 70 nm) in accordance with the

www.manaraa.com

experimental results of Figure 5.7a. As the microcavity length increases, the CBP emission broadens and red shifts significantly, as would be expected for strong microcavity effects.

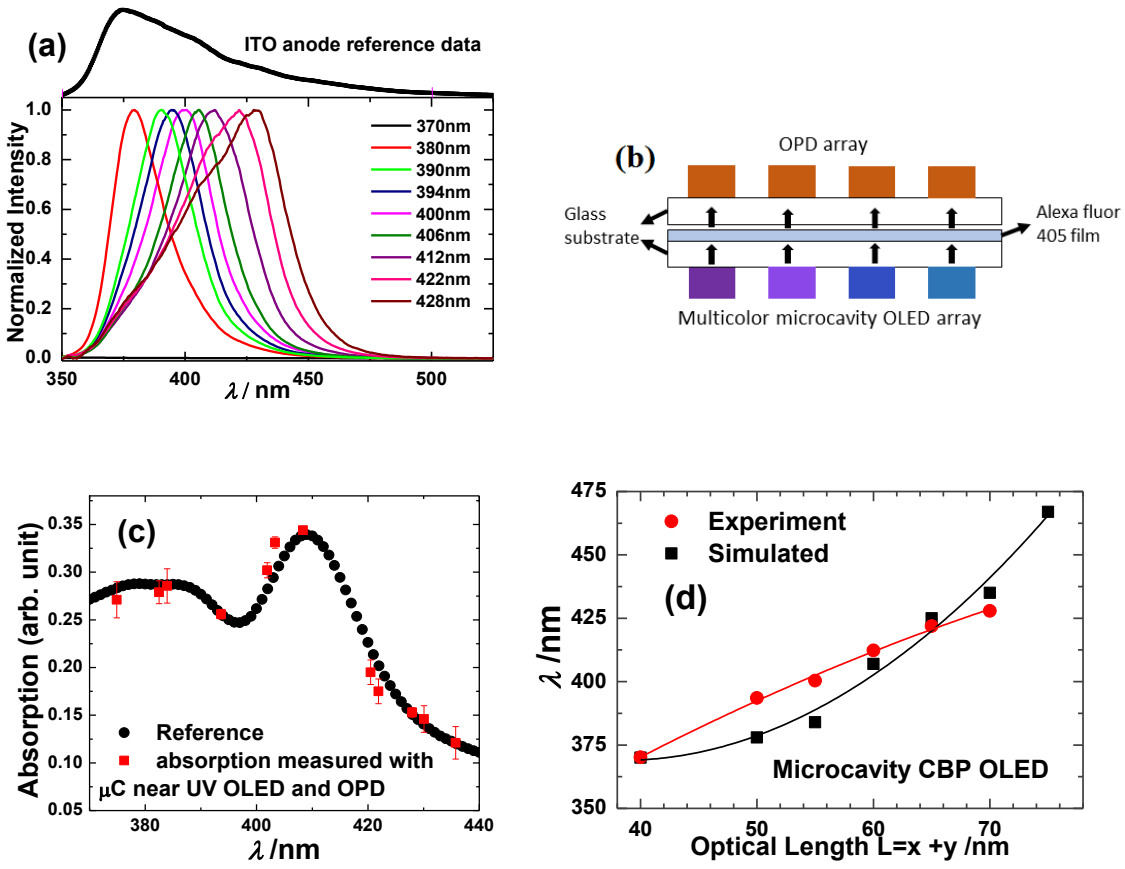

Figure 5.6: a) (a) EL spectra of OLEDs of the structure 15 nm Al/5 nm MoO_3/20 nm TAPC/CBP/BPhen/1 nm LiF/Al with different CBP and BPhen layer thickness of 15-30 nm and 25-40 nm, respectively. (b) Schematics of the all-organic on-chip spectrometer (not to scale) (c) Absorption of an Alexa fluor 405 film on glass, measured with the near UV microcavity OLEDs and the ITO/PEDOT:PSS /P3HT:PCBM /Ca/Al photodetector (squares) and with the ocean optics system (circles). (d) Comparison of the experimental and simulated peak emission wavelengths vs the optical length L. The lines are smooth fits to the simulated and experimental points.

5.3. Summary and Conclusions:

We demonstrated simple fabrication and characterization of improved near UV microcavity OLEDs, with peak emission at ~385 nm, using CBP as the emitting layer.

www.manaraa.com

BPhen and TAPC layers at the cathode and anode, respectively, strongly enhanced device performance improving electron-hole recombination in the emitting layer. A relatively low turn-on voltage of ~3.8 V – only 0.58 V above the 385 nm photon energy – was achieved via the use of an Al/Pd bi-layer anode, rather than Al only. We also demonstrated the structural integration of this device with an OPD to generate an all-organic compact O_2 sensor. The use of the near UV μcOLED improved the sensor performance in comparison to the previously used green μcOLED for probe excitation, where the [O_2] dynamic range was limited. In addition, we tuned this near UV microcavity device to produce a multicolor μcOLED array by gradually changing the thickness of the CBP and BPhen layers. This array was utilized in an all-organic spectrometer on a chip for measuring the absorption spectrum of an Alexa fluor 405 dye film. Two different OPDs, i.e., P3HT:PCBM- and PTB7:PCBM-based, were utilized; the latter improved the sensing performance. Simulations based on the scattering matrix approach were in good agreement with the experimental results and contributed to device fabrication.

5.4. Experimental Procedures

5.4.1. Materials

PtOEP, PS (molecular weight M_w ~ 45,000 and 288,000) and PEG (M_w ~ 1000) were used to prepare the sensing films. The dye was purchased from H. W. Sands and PS and PEG were purchased from Sigma-Aldrich. Molybdenum oxide (MoO_3), the hole injection material, was purchased from Sterm Chemicals, 4, 4′-cyclohexylidenebis [N, N-bis (4-methylphenyl) benzenamine] (TAPC), the hole transport and electron-blocking material, and CBP, the emitting material, were purchased from Luminescence Technology Corporation. The hole- and exciton-blocking material bathophenanthroline (BPhen) was

www.manaraa.com

purchased from Sigma-Aldrich and used as the electron transport material. Alexa fluor 405 dye was purchased from Life Technologies.

5.4.2. Fabrication procedures

OLED Fabrication

OLEDs were fabricated on cleaned and UV-ozone treated glass substrates inside a thermal evaporation chamber with a base pressure of $\sim 10^{-6}$ mbar within a glovebox. Al electrodes and all organic materials were deposited by thermal evaporation. The Al cathode was deposited through a shadow mask containing either 1.5 mm diameter circular holes or 3 mm wide stripes. The combinatorial array for the spectrometer was fabricated by varying the thickness of organic layers using a sliding shutter.

Sensing film fabrication

PtOEP, PS and PEG were dissolved in 1 mL toluene at different weight ratios to generate solutions of 1:40 PtOEP:PS ($M_w \sim 45{,}000$), 1:40 PtOEP:PS ($M_w \sim 288{,}000$), 1:4:36 PtOEP:PEG:PS ($M_w \sim 288{,}000$), and 1:8:32 PtOEP:PEG:PS ($M_w \sim 288{,}000$). The sensing films were prepared by drop-casting 200 µL of the solution on the back side of OLED glass substrates. The OLEDs (excitation source) were driven by a pulse generator (Avtech AV-1011B) generating 1ms pulses at a rate of 50 Hz. Various concentrations of oxygen were generated by mixing high purity Ar and O_2, using mass flow controllers, at a constant flow rate. The Alexa fluor 405 films, 500 – 750 nm thick, were made from 0.1 mg/mL dye in water and baked at 120°C for two hours.

www.manaraa.com

5.4.3. Measurements

OLED characterization

Characterization of the OLEDs was done using a Keithley 2400 source meter to apply a voltage and measure the current. A Thorlab PM100 power meter was used for measuring the irradiance. The EL spectra were obtained using an Ocean Optics CHEM2000 spectrometer. The raw spectra were obtained in the "SCOPE" mode, but were corrected to the radiometrically calibrated mode; the spectra shown are the corrected spectra.

PL and absorption measurements

The PL decay curves of the sensing film at different oxygen concentrations were monitored by a Hamamatsu R6060 photomultiplier tube (PMT). The PL intensity of the 1:4:36 PtOEP: PEG: PS sensing film was monitored with standard P3HT:PCBM and PTB7:PCBM OPDs and the current from the detector was measured by a Keithley 2400 source meter. In the latter case the OLED was driven by a constant voltage generated by a KEPCO (Abc-125 1 dm) power supply.

5.5. Acknowledgements

Ames Laboratory is operated by Iowa State University for the US Department of Energy (USDOE) under Contract No. DE-AC 02-07CH11358. The research was partially supported by Basic Energy Sciences, Division of Materials Science and Engineering, USDOE. This research used resources of the National Energy Research Scientific Computing Center, which is supported by the Office of Science of the USDOE under Contract No. DE-AC02-05CH11231. We also thank Chun Xu for computational programs.

www.manaraa.com

5.6. References:

[1] S. Purandare, E. F Gomez, A. J Steckl, *Nanotechnol.* **25**, 094012 (2014).

[2] H. H. Kim, H. J. Kim, B. J. Choi, Y. S. Lee, S. Y. Park, L. S. Park, *Mol. Cryst. Liq. Cryst.* **584**, 153 (2013).

[3] J. Shinar, R. Shinar, *J. Phys. D: Appl. Phys.* **41**, 133001 (2008).

[4]T. Mayr, T. Abel, E. Kraker, S. Köstler, A. Haase, C. Konrad, M. Tscherner, B. Lamprecht, *Procedia Eng.* **5**, 1005 (2010).

[5]T. H. Han, Y. Lee, M.R. Choi, S.H. Woo, S.H. Bae, B.H. Hong, J.H. Ahn, T.W. Lee, *Nat. Photonics* **6**, 105 (2012).

[6] K. Hoshino, T. Hasegawa, K. Matsumoto, I. Shimoyama, *Sens. Actuators, A* **128**, 339 (2006).

[7] J. W. Park, D. C. Shin. S. H. Park, *Semicond. Sci. Technol.* **26,** 034002 (2011).

[8] R. Liu, T. Xiao, W. Cui, J. Shinar, R. Shinar, *Anal. Chim. Acta* **778,** 70 (2013).

[9] Y. Cai, R. Shinar, Z. Zhou, J. Shinar, *Sens. Actuators, B* **134,** 727 (2008).

[10]Z. Zhou, R. Shinar, B. Choudhury, L. B. Tabatabai, C. Liao, J. Shinar, in *Chemical and Biological Sensors for Industrial and Environmental Security*, edited by Arthur J. Sedlacek III, S. D. Christensen, R. J. Combs, T. Vo-Dinh, *SPIE Conf. Proc.* **5994**, 59940E (2005).

[11] R. Liu, Y. Cai, J. M. Park, K. M. Ho, J. Shinar, R. Shinar, *Adv. Funct. Mater.* **21**, 4744 (2011).

[12] X. D. Wang, O. S. Wolfbeis, *Chem. Soc. Rev.* **43**, 3666 (2014).

[13] G. Williams, C. Backhouse, H. Aziz, *Electronics* **3**, 43 (2014).

[14]S. Camou, M. Kitamura, J.P. Gouy, H. Fujita, Y. Arakawa, T. Fujii, in *Proc. SPIE 4833, Applications of Photonic Technology* **5**, 1 (2003).

[15] B. Yao, G. Luo, L. Wang, Y. Gao, G. Lei, K. Ren, L. Chen, Y. Wang, Y. Hu, Y. Qiu, *Lab Chip* **5**, 1041 (2005).

[16] K. N. Ren, Q. L. Liang, B. Yao, G. O. Luo, L. D. Wang, Y. Gao, Y. M. Wang, Y. Qiu, *Lab Chip* **7**, 1574 (2007).

www.manaraa.com

[17] B. Yao, H. Yang, Q. Liang, G. Luo, L. Wang, K. Ren, Y. Gao, Y. Wang, Y. Qiu, *Anal. Chem.* **78**, 5845 (2006).

[18] L. Scholer, K. Seibel, K. Panczyk, M. Bohm, *Microelectron. Eng.* **86**, 1502 (2009).

[19] E. Kraker, A. Haase, B. Lamprecht, G. Jakopic, C. Konrad, S. Köstler, *Appl. Phys. Lett.* **92,** 033302 (2008).

[20] P. Puligundla, J. Jung, S. Ko, *Food Control* **25,** 328 (2012).

[21] M. Scholles, L. Kroker, U. Vogel, J. Krüger, R. Walczak, J. Ruano-Lopez, in *Proc. of SPIE* **7593**, 75930C (2010).

[22] A. Marcello, D. Sblattero, C. Cioarec, P. Maiuri, P. Melpignano, *Biosens. Bioelectron*. **46,** 44 (2013).

[23] F. So, J. Kido, P. Burrows, *MRS Bull*. **33**, 663 (2008).

[24] G. Gu, S.R. Forrest, *IEEE J. Sel. Top. Quant. Electron*. **4,** 83 (1998).

[25] T. Yu, W. Su, W. Li, R. Hua, B. Chu, B. Li, *Solid State Electron*. **51,** 894 (2007).

[26] C.F. Qiu, L. D. Wang, H. Y. Chen, M. Wong, H. S. Kwok, *Appl. Phys. Lett*. **79**, 2276 (2001).

[27] L. Zou, V. Savvate'ev, J. Booher, C. H. Kim, J. Shinar, Appl. Phys. Lett. **79**, 2282 (2001).

[28] Y. Q. Li, J. X. Tang, Z. Y. Xie, L. S. Hung, S. S. Lau, *Chem. Phys. Lett*. **386**, 128 (2004).

[29] P. E. Burrows, V. Khalfin, G. Gu, S. R. Forrest, *Appl. Phys. Lett*. **73**, 435 (1998).

[30] R. Liu, C. Xu, R. Biswas, J. Shinar, R. Shinar, *App. Phys. Lett*. **99,** 093305 (2011).

[31] H. Kautsky, *Biochem. Z.* **291**, 271 (1937).

[32] R. Liu, Z. Ye, J.M. Park, M. Cai, Y. Chen, K.-M. Ho, R. Shinar, J. Shinar, *Optics Express* **19**, A1272 (2011).

[33] A. K. Bansal, W. Holzer, A. Penzkofer, T. Tsuboi, *Chem. Phys*. **330**, 118 (2006).

[34] R. Biswas, C. Xu, W. Zhao, R. Liu, R. Shinar, J. Shinar, *J. Photon. Energy* **1**, 011016 (2011).

[35] M. Kang, I. Kim, M. Chu, S. W. Kim, *J. Korean Phys. Soc*. **59**, 3280 (2011).

[36] H. Peng, J. Sun, X. Zhu, X. Yu, M. Wong, H. S. Kwok, Appl. Phys. Lett. **88,** 073517 (2006).

www.manaraa.com

[37] N. Ahmad, J. Stokes, N. A. Fox, M. Teng, *J. Cryan, Nano Energy* **1,** 777 (2012).

[38] Refractive Index data base of elements and compounds, http://refractiveindex.info/legacy

[39] R. Liu, Z. Gan, R. Shinar, J. Shinar, *Phys. Rev. B* **83**, 245302 (2011).

[40] K. S. Nalwa, Y. Cai, A. L. Thoeming, J. Shinar, R. Shinar, S. Chaudhary, *Adv. Mater.* **22**, 4157 (2010).

[41] B. Huang, S.A. Jones, B. Brandenburg, X. Zhuang, *Nat Methods* **5**, 1047 (2008).

[42] E. Palik, *Handbook of the Optical Constants of Solids II,* Academic Press, Boston (1991).

[43] F. Hamelmann, A. Brechling, A. Aschentrup, U. Heinzmann, P. Jutzi, J. Sandrock, U. Siemeling, T. Ivanova, A. Szekeres, K. Gesheva, *Thin Solid Films* **446,** 167 (2004**)**.

[44] S. Hermann, O. D. Gordon, M. Friedrich, D. R. T. Zahn, *Phys. Status Solidi C* **2**, 4037 (2005).

www.manaraa.com

CHAPTER 6

SUMMARY AND CONCLUSIONS

As there is an ever increasing demand for highly efficient, flexible and compact OLEDs for lighting and analytical applications, emphasis is given toward increasing OLEDs' light outcoupling factor and enhancing the sensitivity of analytical sensing (oxygen sensor is discussed here) in all-organic platform.

Highly efficient small molecule phosphorescent OLEDs were fabricated on nano-patterned PC and PET substrates with various patterns. The corrugation height for these substrates were optimized by analyzing the performance of OLEDs on these patterns. 1.5-3 fold enhancement in luminous efficiency is achieved for blue and green OLEDs using 270-320 nm patterns on PC, mostly by reducing light trapping inside the device. 1.28-2.6 fold luminous efficiency enhancement were reported with efficient and color stable fluorescent WOLEDs fabricated on optimized patterns. The enhancement factor is found to be greatly dependent on the final corrugation height after PEDOT:PSS deposition. The challenges of conformally developing a polymer anode on nano-patterns were evaluated and use of a hybrid anode with highly transparent metal mesh with PEDO:PSS is proposed as a potential solution.

We demonstrated simple fabrication and characterization of improved near-UV microcavity OLEDs, with peak emission at ~385 nm, which was successfully employed as an excitation source for PL-based oxygen sensing. Improved detection limits and dynamic ranges were achieved by structural integration of the μC CBP-based OLED with PTB7:PCBM OPD. In addition, we tuned this near UV microcavity device to produce a multicolor μcOLED array by gradually changing the thickness of the organic layers. This

www.manaraa.com

array was subsequently integrated with a P3HT:PCBM OPD and utilized in an all-organic spectrometer on a chip for measuring the absorption spectrum of an Alexa fluor 405 dye film.

www.manaraa.com

APPENDIX A

WOLEDS IN SSL AND COLOR POINT MANAGEMENT

For general illumination, the white light source is generally characterized by its black body color temperature and the color temperature ranging from 2800K to 6500K is considered to be preferred for lighting purposes.

The perceived brightness of the OLED depends strongly on its emission spectrum. The photopic curve, the sensitivity of human eye to different wavelength of light, is shown in the **Figure 1.6** in Chapter 1. The photosensitivity of the human eye peaks at 555 nm and vanishes above ~700 nm and below ~390 nm, as seen in figure. The tristimulus parameter set (X, Y, Z) to calculate color coordinates in standardized 1931XYZ color space from the color matching function ($\tilde{x}(\lambda)$, $\tilde{y}(\lambda)$, $\tilde{z}(\lambda)$) dependent on the human eye's perception to different colors. The relations are shown in the following equations.

$$X = K\int_{380}^{700} g(\lambda)\,\tilde{x}(\lambda)d\lambda \quad \text{A.1}$$

$$Y = K\int_{380}^{700} g(\lambda)\,\tilde{y}(\lambda)d\lambda \quad \text{A.2}$$

$$Z = K\int_{380}^{700} g(\lambda)\,y\tilde{z}(\lambda)d\lambda \quad \text{A.3}$$

Where g(λ) is the spectrum power distribution of the light source and K is an empirical constant calculated to give the actual brightness as Y. The CIE color coordinates are calculated in the following way.

$$x = \frac{X}{X+Y+Z} \quad \text{A.4}$$

$$y = \frac{Y}{X+Y+Z} \quad \text{A.5}$$

The color coordinates for red, green and blue colors are shown the figure X. Although, the distance between these (x, y) coordinates in color space is not directly to the difference in

www.manaraa.com

human perception the change in color for those particular points. For example, the eye sensitivity is more in the color change in blue region than in green region. Thus a new set of coordinates (u', v') for standardized 1976 is popularly used by the display industry, which can be calculated in the following way.

$$u' = \frac{4x}{-2x+12y+3} \quad \text{A.6}$$

$$v' = \frac{9y}{-2x+12y+3} \quad \text{A.7}$$

CIE color coordinates (x, y) used by display industry can be calculated by calculating the blackbody spectrum at a particular temperature and then calculate x, y from that using the following equation.

Plotting the set of x,y coordinates for each color temperature, the black-body locus can be drawn as shown in the figure. Warmer light corresponds to the lower color temperature while cooler light corresponds to higher color temperature. A deviation of 0.01 in the x, y coordinates from the black-body emitter locus is accepted for general illumination.

Color rendering index (CRI (R)) is a quantitative measurement of the capability of a light source to produce the true color of an object upon illumination as compared to the ideal light. Two light sources with same color temperature but with different spectral power distribution will have different CRI. For lighting application, CRI is typically used. However, CIE color coordinates were used in this thesis instead of CRI to avoid complex measurement and calculation.

www.manaraa.com

APPENDIX B

OPDS IN ANALYTICAL SENSING: SUMMARY TABLES

From E. Manna, T. Xiao, J. Shinar, R. Shinar, *Electronics* **4**, 688 (2015)

Table B.1. Summary of electrical and optical attributes of the OPDs

PD details	Dark current (nA/cm^2) (Bias, V)	EQE (%)	Respon-sivity (A/W)	Wavelength range (nm)	Response time	Lifetime	Noise	Refs.
ITO/CuPc:C_{60}/BCP/Al; BHJ	~ 6.25 (~0)	30		600-700				42
ITO/CuPc/C_{60}/BCP/Ag;	0 (+ 0-0.2)	15-17	0.07 @ 493 nm, 0.11 @ 592 nm		--	--	--	80
ITO/CuPc/C_{60}/BCP/Ag;		23		400-500				83
ITO/PEDOT:PSS/ CuPc/C_{60}/LiF/Al	0.83 (~0)	--	0.008 A/W @ 570 nm	500-700	--	2 weeks	--	64, 65
ITO/CuPc/C_{60}/CuPc/C_{60}/LiF/Al	--	--	0.023 @ 560 nm	500-700	--	--	--	66

www.manaraa.com

ITO/CuPc/ CuPc:C_{60}/C_{60}/BCP /Al Mixed heterojunction		IPCE 19 @ 585 nm		400-750				81
ITO/LiF/ CuPc/C_{70}/ BPhen/Al	--	35 @ 640 nm	--	400-700 nm	--	--	--	75
ITO/ TPTPA:C70 /BCP/Ag		IPCE44 @ 586		400-600				82
Au(or Au/MoO_3)/CuPc/PTCBI/ Alq_3 (BPhen) /Ag	~1 nA	10 @ 600 nm	--	500-700	1.3-1.6 μs (with BPhen)	--	--	68-73, 84
ITO/PEDOT:PSS/ P3HT:PCBM/Al [or LiF/Al, Ca/Al or Ba/Al as cathode]	0.1-1 (~0-0.1)	50-70	0.25	350-600	0.51 μs rise-time; 0.66 μs fall-time	over 3 years shelf life	~1 pA @ 1 Hz band-width	44-46, 74, 77, 79, 88
ITO/PEDOT:PSS/ rr-P3HT: $PC_{61}BM$/Ca/ Ag	~65 (-5)	76 (-5 V)	0.36	400-650	--	over 1 year	$8.2*10^{-14}$ A/ $Hz^{1/2}$	85-86

www.manaraa.com

ITO/PEDOT:PSS/PCDTBT:$PC_{70}BM$ /LiF/Al	$2.8*10^{-3}$ (~0)	60-70	0.22 @ 405 nm	400-600	--	25% photo-current decrease in 15 days	D*~ 9.2 x10^11 jones	47,49-54
ITO/PTB3: $PC_{61}BM$/LiF/Al	<1	45 @ 685 nm	0.26 @ 685 nm	400-750	1 μs	--	--	78
ITO/PEDOT:PSS/ PTB7:PCBM/Ca/Al	~1-2 (~0)	88 @ 640 nm	--	400-700	--	--	--	77
Conductive PEDOT:PSS/ PEDOT:PSS/ PTB7:$PC_{71}BM$/ Al	1 (-2)	38 @ 532 nm; 47 @ 626 nm	--	400-750		24% photo-current decrease over 7 days (OLED/OPD lifetime)		87
thin film c-Si PD	0.63 (~0)	--	0.19-0.34	470-600	--	--	--	114
a-Si:H	0.01-0.1 (-3)	50	--	500-550	--	--	--	115,116
(poly-Si) with interdigitated p-i-n structure	<5 nA	50	0.33	850	--	--	--	117
PbS CQD	0.1	50 @ 550 nm		500-1400	~300ns	> 2months	D* ~1x10^{12} jones	118

www.manaraa.com

- We note that the dark current at nominally 0 bias may be due to some remnant light.
- The structure of the OPDs is heterojunction, if not specified otherwise.

Generally, OPDs are often comparable to their inorganic counterparts in terms of dark current and responsivity, though their response time is typically longer. Optimization of OPDs is an ongoing field of research.

Table B.2. Summary of the OPDs' analytical applications.

Detection approach	PD type/active layer	Analyte	LOD	Ref.	Comments
CL	CuPc-C_{60} BHJ	H_20_2	1 mM	42	High LOD due to larger size of the OPD compared to the detection chamber
	P3HT:PCBM BHJ	$H_2O_{2;}$	10 μM;	44	Results are comparable to inorganic PD (Newport 818 UV silicon PD) and PMT (Hamamatsu R3896 and RAPTOR fiber optic biosensor)
		Antioxidants;	1-50 μM;	45	
		Staphylococcal enterotoxin B	0.5 ng/ml	46	
	PCDTBT: $PC_{70}BM$ BHJ; ring shaped OPDs	rhTSH	30-80 pg/ml	47, 49	Higher detection sensitivity than with a P3HT based PD, excellent linearity, multiplexed detection
		Stress hormone cortisol	<0.28 nM	50	
		E. Coli	$5x10^5$ cell/ml	51	
		C. jejuni	$1x10^5$ cell/ml		
		Adenovirus	$1x10^{-8}$ mg/ml		
		17-β estradiol	2.5 pg/ml	53	
		Legionella pneumophila	$4x10^4$ cell/ml	54	

www.manaraa.com

	a-Si:H	*HRP*	0.2 amol	119	
	Metal semiconductor (c-Si N^+) metal PD	*Streptavidin*	4.76 nM	120	
PL	CuPc-C_{60} heterojunction	Rhodamine 6G	10 nM (halide excitation), 100 nM (OLED excitation)	64, 65	
		Fluorescein	10 nM (halide), 10 μM (OLED)		
		resorufin	5.0 μM	80	
		IgA	16 ng/ml		
		malachite green, phosphate	0.02 ppm	83	
	Bilayer CuPc/C60	Rhodamine 6G	10 nM	66	
	CuPc/C_{70} heterojunction	O_2, pH	--	75	Time-resolved sensing
	CuPc/ CuPc:C_{60} /C_{60} mixed heterojunction	APnEOs	2-4 ppb	81	
	CuPc/PTCBI	Various indicators for O_2, CO_2, pH	--	68-73, 84	ring shaped OPD
	TPTPA:C_{70}	resorufin	0.6 μM	82	--
		APnEOs	1-2 ppb		
	P3HT:PCBM BHJ	O_2, β-D-glucose	--	74	Time resolved sensing
		Diuron	11nM	78	higher sensitivity than commercial

www.manaraa.com

					biosensors (Handy-PEA fluorometer)
		myoglobin, CK-MB	1.5 ng/ml	79	Higher photoresponse than silicon (Osram Opto Semiconductors, SFH2430)
	PTB7:$PC_{61}BM$	O_2	--	77	--
	a-Si:H	Fluorescein	680 pM; 17 nM (with integrated PD on microchip)	115	--
		Green fluorescent protein	18.5 nM	116	
Light scattering	Regioregular P3HT: $PC_{61}BM$	Living HELA cells	<1000 cells/cm^2	85-86	Label free monitoring
		calcein-AM	--		
	PTB3:$PC_{61}BM$ BHJ	Mouse immuno-globulin G	5 nm spectral resolution	88	Grating-based spectrometer
Absorption	P3HT: $PC_{61}BM$	Alexa Fluor 405	5-10 nm spectral resolution	77	Absorption based spectrometer
	PTB7:$PC_{71}BM$	Oxy hemoglobin	--	87	Flexible integrated sensor, pulsed oximetry

*Please refer to Chapter 4 for the reference

www.manaraa.com